الجمهورية الجزائرية الديمقراطية الشعبية

People's Democratic Republic of Algeria

وزارة التعليم العالي والبحث العلمي

Ministry of Higher Education and Scientific Research

University of 20th August 1955 - Skikda جامعة 20 أوت 1955 سكيكدة

Faculty of sciences كلية العلوم

Department of Chemistry قسم الكيمياء

PhD thesis

Submitted in partial fulfilment of the requirements for the degree of
Doctor of Philosophy in Chemistry (LMD)

Specialization:
Environmental Chemistry

Evaluation of the performance of catalytic advanced oxidation processes (AOPs) in homogeneous and/or heterogeneous phases: application to the removal of refractory organic pollutants

By: Kahoul Khadidja

Defended on: 20 /01/ 2025

Approved by the Examining Board:

Zaghdoudi Rachida	Professor	President	University of Skikda
Ahmedchekkat Fatiha	Doctor (MCA)	Supervisor	University of Skikda
Guechi El-Khamssa	Professor	Examiner	University of Annaba
Bechiri Ouahiba	Professor	Examiner	University of Annaba
Krid Ferial	Professor	Examiner	University of Skikda
Boussouf Ibtissam	Doctor (MCA)	Examiner	University of Skikda
Chiha Mahdi	Professor	Invited	University of Skikda

Academic year : 2025/2026

الجمهورية الجزائرية الديمقراطية الشعبية
République algérienne démocratique et populaire
وزارة التعليم العالي والبحث العلمي
Ministère de l’Enseignement Supérieur et de la Recherche Scientifique

Université de 20 Aout 1955 - Skikda جامعة 20 أوت 1955 سكيكدة

Faculté de sciences كلية العلوم

Département de chimie قسم الكيمياء

Thèse

Présentée en vue de l’obtention du diplôme de

Doctorat LMD en chimie

Spécialité :

Chimie de l’environnement

Évaluation des performances des procédés d’oxydation avancée (POAs) catalytiques en phase homogène et/ou hétérogène : application à l’élimination des polluants organiques réfractaires

Présentée Par : Kahoul Khadidja

Soutenue le : 20 /01/ 2026

Devant le Jury composé de :

Zaghdoudi Rachida	Professeur	Présidente	Université de Skikda
Ahmedchekkat Fatiha	Docteur (MCA)	Encadrante	Université de Skikda
Guechi El-Khamssa	Professeur	Examiner	Université de Annaba
Bechiri Ouahiba	Professeur	Examiner	Université de Annaba
Krid Ferial	Professeur	Examiner	Université de Skikda
Boussouf Ibtissam	Docteur (MCA)	Examiner	Université de Skikda
Chiha Mahdi	Professeur	Invité	Université de Skikda

Année universitaire : 2025/2026

To my father, for his endless support and encouragement.

To my mother, sister, and brothers, with love and gratitude.

To my beloved aunt, whose kindness has always inspired me.

To my dear grandmother, a source of endless love and wisdom.

Khadidja KAHOUL

Acknowledgments

First and foremost, I thank Allah Almighty for His infinite mercy, guidance, and blessings, without which this work would not have been possible. It is only by His will and support that I had the strength and perseverance to complete this thesis.

I want to express my appreciation to my supervisor, Dr Fatiha Ahmedchekkat, for her guidance throughout this project.

My sincere gratitude goes to Professor Chiha Mahdi, Head of the Laboratory, for his valuable technical assistance and insightful guidance, which contributed significantly to the advancement of this research. I also warmly thank the engineers Houda Brahimi, Boujnah Souhila, and Bouchokh Sihem, as well as Engineer Hasssiba Boutrik (University of Bouira), for their valuable technical assistance and constant support, which greatly contributed to the success of this research. I am deeply grateful to my dear friends Barkahoum Chelabi and Dalila Bousbaa, whose encouragement and companionship were a source of strength during this journey. I also wish to acknowledge my colleagues in the laboratory, Amina Bousireb, Nesrine Bouguizi, Nour Souames, and Nour Brahmi, for their collaboration, stimulating discussions, and the friendly atmosphere they created.

Finally, I extend my heartfelt thanks to all those who, directly or indirectly, contributed to the realization of this thesis.

Abstract:

The persistence of refractory organic pollutants (ROPs) in aquatic environments poses a significant challenge due to their chemical stability, resistance to conventional treatment methods, and adverse ecological and health impacts. Among these pollutants, Rhodamine B (RhB) is widely used as a model compound to assess advanced oxidation processes (AOPs). This work focuses on the performance evaluation of catalytic AOPs in both homogeneous and heterogeneous phases, with particular emphasis on semiconductor-based photocatalysis. Titanium dioxide (TiO_2) nanoparticles were synthesized via a non-conventional sol-gel route and calcined at different temperatures (400, 600, and 800 °C). The materials were extensively characterised using TG/DSC, FTIR/ATR, XRD, BET, SEM/EDX, UV/Vis, and pHpzc analysis. Their photocatalytic performance was investigated through the degradation of RhB under various operational conditions, including pollutant concentration, catalyst loading, pH solution, irradiation wavelength, and calcination temperature. The TiO_2-400 sample exhibited the highest degradation efficiency (96.11%) and stability, demonstrating its suitability as an efficient photocatalyst. To further enhance its photocatalytic activity, TiO_2 was incorporated into bentonite clay supports with varying contents (10% TiO_2-BN, 30% TiO_2-BN, and 50% TiO_2-BN) using the same non-conventional sol-gel method. The TiO_2-bentonite composites (TiO_2-BN) were characterised using FTIR/ATR, XRD, BET, SEM/EDX, and pH_{pzc}, and tested for RhB removal under various conditions: pollutant concentration, catalyst loading, solution pH, and irradiation wavelength. The incorporation of bentonite enhanced surface area, adsorption capacity, and charge separation, leading to improved degradation performance. The 50% TiO_2-BN sample displayed the best balance between adsorption and photocatalytic activity, with a degradation rate of 99.64%. Kinetic studies confirmed that RhB degradation followed a pseudo-first-order model based on the Langmuir-Hinshelwood (L-H) mechanism. A direct comparison between TiO_2-400 and 50% TiO_2-BN composites highlighted the synergistic role of bentonite in enhancing photocatalytic efficiency. Overall, this research demonstrates that tailoring the synthesis route, calcination temperature, and support material significantly influences photocatalytic performance. The findings contribute to the development of sustainable catalytic AOPs for the removal of refractory organic pollutants from water, offering promising perspectives for environmental remediation.

Keywords: Advanced oxidation process, Catalysis, Water, Refractory organic pollutants (ROPs).

الملخّص:

إن استمرار وجود الملوّثات العضوية المقاومة (ROPs) في البيئة المائية يشكل تحدياً كبيراً نظراً لاستقرارها الكيميائي، ومقاومتها لطرق المعالجة التقليدية، فضلاً عن آثارها السلبية على النظم البيئية وصحة الإنسان. ومن بين هذه الملوّثات، يُستخدم مركب الرودامين ب (RhB) على نطاق واسع كمركب نموذجي لتقييم تقنيات الأكسدة المتقدمة (AOPs). يركّز هذا العمل على تقييم أداء عمليات الأكسدة المتقدمة التحفيزية في الطورين المتجانس وغير المتجانس، مع إيلاء اهتمام خاص لعملية التحفيز الضوئي المعتمدة على أنصاف النواقل. تم تحضير جسيمات ثاني أكسيد التيتانيوم النانوية (TiO_2) بواسطة طريقة سول-جيل (Sol-gel) غير تقليدية، ثم تمّ تكليسها تحت درجات حرارة مختلفة (400، 600، و800 °م). وقد جرى توصيف المواد المحضرة بشكل موسع باستخدام تقنيات TG/DSC، وFTIR/ATR، وXRD، وBET، SEM/EDX، UV/Vis، وpHpzcوتم تقييم أدائها من خلال دراسة تحلل صبغة RhB تحت ظروف تجريبية مختلفة شملت: تركيز الملوّث، كتلة TiO_2 المضافة، قيمة pH المحلول، طول الموجة الإشعاع، ودرجة حرارة التكليس. وقد أظهرت العيّنة TiO_2-400 أعلى نسبة في تحلل الرودامين ب (96.11%) مع ثباتية جيدة، مما يبرهن على فعاليته. ولتعزيز نشاطه للتحفيزي الضوئي أكثر، تم دمج TiO_2 مع طين البنتونيت بنسب مختلفة: (10% TiO_2-BN، 30%TiO_2-BN و 50% TiO_2-BN) باستخدام نفس طريقة السول-جيل غير التقليدية. جرى توصيف مركبات-TiO_2 بنتونيت (TiO_2-BN) بواسطةFTIR/ATR ، وXRD، وBET، SEM/EDX، وpH_{pzc}، واختُبرت لإزالة RhB تحت ظروف مختلفة: تركيز الملوث، كمية المحفّز، قيمة pH للمحلول، وطول الموجة للإشعاع. وقد أدى إدماج البنتونيت إلى تحسين المساحة السطحية والقدرة على الامتزاز وفصل الشحنات، مما أسفر عن تعزيز الأداء في التحلل. وحقق نموذج TiO_2-BN % 50 أفضل توازن بين الامتزاز ونشاط التحلل الضوئي، بمعدل بلغ 99.64%. أكدت الدراسات الحركية أن تحلل RhB اتبع نموذجاً شبه من الدرجة الأولى وفق آلية Langmuir-Hinshelwood (L-H) كما أبرزت المقارنة المباشرة بين TiO_2-400 و 50%TiO_2-BN الدور التآزري للبنتونيت في تعزيز الكفاءة التحفيزية الضوئية. بصورة عامة، يبين هذا البحث أن التحكم في شروط تحضير المحفزات، ودرجة حرارة التكلس، ونوع المادة الداعمة يؤثر بشكل ملحوظ على أداء التحلل الضوئي. وتساهم هذه النتائج في تطوير عمليات أكسدة متقدمة تحفيزية مستدامة لإزالة الملوثات العضوية المقاومة من المياه، مما يوفر آفاقاً واعدة لمعالجة التلوث البيئي.

الكلمات المفتاحية: التقنيات المتقدمة للأكسدة، التحفيز، المياه، الملوثات العضوية المقاومة

Résumé :

La persistance des polluants organiques réfractaires (ROPs) dans les milieux aquatiques constitue un enjeu environnemental majeur en raison de leur stabilité chimique, de leur résistance aux procédés de traitement conventionnels ainsi que de leurs effets écotoxicologiques et sanitaires préoccupants. Parmi ces composés, la Rhodamine B (RhB) est fréquemment employée comme molécule modèle pour l'évaluation des procédés d'oxydation avancée (AOPs). La présente thèse est consacrée à l'étude des performances des AOPs catalytiques en phase homogène et hétérogène, avec une attention particulière portée à la photocatalyse à base de semi-conducteurs. À cet effet, des nanoparticules de TiO_2 ont été synthétisées par une voie sol-gel non conventionnelle, puis soumises à une calcination à 400, 600 et 800 °C. Les matériaux obtenus ont été caractérisés de manière approfondie par TG/DSC, FTIR/ATR, XRD, BET, SEM/EDX, UV/Vis et pH_{pzc}. L'échantillon TiO_2-400 a présenté la meilleure efficacité de photodégradation de la RhB (96,11 %) ainsi qu'une stabilité remarquable, confirmant son potentiel en tant que photocatalyseur performant. Dans une seconde étape, afin d'accroître l'activité photocatalytique, des composites TiO_2-bentonite (10 % TiO_2-BN, 30 % TiO_2-BN, 50 % TiO_2-BN) ont été élaborés par la même méthode sol-gel non conventionnelle. Leur caractérisation et leur évaluation ont montré que l'incorporation de la bentonite favorise l'augmentation de la surface spécifique, de la capacité d'adsorption et de la séparation des charges, ce qui se traduit par une amélioration notable de la performance photocatalytique. Le composite contenant 50 % TiO_2 a offert le meilleur compromis entre adsorption et activité photocatalytique, atteignant un taux de photodégradation de 99,64 %. Les études cinétiques ont confirmé que la dégradation de la RhB obéit à un modèle pseudo-premier ordre, en accord avec le mécanisme de Langmuir-Hinshelwood. Ces résultats mettent en évidence l'effet synergique de la bentonite et démontrent que la voie de synthèse, la température de calcination et la nature du support exercent une influence déterminante sur les performances photocatalytiques. Dans l'ensemble, ce travail contribue à l'avancement des connaissances sur les procédés d'oxydation avancée catalytiques et ouvre des perspectives prometteuses pour le développement de solutions durables visant l'élimination des polluants organiques réfractaires des milieux aqueux.

Mots clés : Les procédés d'oxydation avancées, Catalyse, Eau, Polluants organique réfractaire (PORs)

Table of contents

Chapter I: Literature review

Chapter II: Experimental procedures and characterization techniques

Chapter III: Results and discussion

Part 1: Photodegradation of Rhodamine B using TiO_2 nanocatalyst synthesized via non-conventional sol-gel method

Part 2: Preparation of TiO_2-Bentonite composites via a non-conventional sol-gel route for the photodegradation of Rhodamine B

Chapter VI: Kinetic analysis of synthesized photocatalysts

List of abbreviations and acronyms

ROPs	Refractory organic pollutants
RhB	Rhodamine B
AOPs	Advanced oxidation processes
CB	Conduction band
BV	Valence band
Eg	Band gap energy
TTIP	Titanium tetraisopropoxide
ROS	Reactive oxygen species
TG/DSC	Thermo-gravimetric and differential scanning calorimetry
XRD	X-ray diffraction
BET	Brunauer-Emmett-Teller
FTIR/ATR	Fourier-transform infrared spectroscopy with attenuated total reflectance
(SEM/EDX)	Scanning electron microscopy /Energy-dispersive X-ray spectroscopy
PZC	Point of zero charge
UV-Vis	UV-Vis Spectroscopy
TiO_2-BN	TiO2-bentonite composites
TiO_2-P25	(TiO2) Degussa P-25
TiO_2-400	TiO2 calcined at 400°C
TiO_2-600	TiO2 calcined at 600°C
TiO_2-800	TiO2 calcined at 800°C
C_0	Initial concentration (mg/L) of Rhodamine B
C_t	Concentration of Rhodamine B at time t (mg/L)
k_1	First-order rate constants
k_2	Second-order rate constants
L-H	Langmuir-Hinshelwood
K	Adsorption coefficient of the reactant in (L.mg-1)
ka	Reaction rate constant in (mg. L^{-1}.min^{-1})

List of tables

Chapter I

Chapter II

Chapter III

Chapter IV

List of figures

Chapter I

Chapter II

Chapter III

Chapter IV

General introduction:

Water pollution has emerged as one of the most pressing global challenges of the twenty-first century, driven by rapid industrialization, urban expansion, and intensified agricultural practices [1]. Among the diverse classes of contaminants, refractory organic pollutants (ROPs) are of particular concern due to their exceptional chemical stability, resistance to biodegradation, and persistence in aquatic environments [2,3]. These compounds, often released from textile, pharmaceutical, dyeing, and agrochemical industries, not only deteriorate water quality but also bioaccumulate, thereby posing long-term risks to aquatic ecosystems and human health [4,5]. Conventional water treatment technologies, including biological processes, coagulation-flocculation, and adsorption, have demonstrated limited efficiency against such pollutants, as they often fail to mineralise them into harmless byproducts fully. Consequently, the scientific community has increasingly turned toward advanced oxidation processes (AOPs) as sustainable, high-performance alternatives capable of addressing this critical environmental challenge [2,6]. Within this framework, semiconductor-based photocatalysis has garnered significant attention due to its ability to generate highly reactive oxygen species under light irradiation, thereby facilitating the mineralization of a wide range of persistent pollutants [7]. Titanium dioxide (TiO_2), in particular, remains the most extensively studied photocatalyst due to its abundance, low cost, non-toxicity, strong oxidizing power, and photostability[8]. However, its photocatalytic performance is strongly influenced by factors such as synthesis route, calcination temperature, crystallinity, surface area, and electron–hole recombination dynamics [9]. To address these challenges, researchers have explored novel synthesis approaches as well as the incorporation of suitable supports or dopants to enhance photocatalytic efficiency and extend light absorption into the visible range [10,11]. The present thesis is dedicated to the evaluation of catalytic advanced oxidation processes (AOPs) in both homogeneous and heterogeneous phases, with a particular focus on semiconductor photocatalysis. To this end, TiO_2 nanoparticles were synthesized using a non-conventional sol-gel method and subsequently calcinated at different temperatures (400, 600, and 800 °C). These materials were extensively characterized through TG/DSC, FTIR-ATR, XRD, BET, SEM/EDX, UV-Vis DRS, and pHpzc analyses. The photocatalytic performance was systematically assessed using Rhodamine B (RhB) as a model pollutant, allowing for the investigation of the effects of initial dye concentration, photocatalyst loading, irradiation wavelength, and solution pH. Among the synthesized materials, the TiO_2-400 sample demonstrated the highest photocatalytic efficiency (96.11%) combined with good stability, thereby confirming its potential as a high-performance nanocatalyst.

In a second stage, the study was extended to the development of TiO_2–bentonite composites (with 10, 30, and 50% TiO_2) using the same sol-gel route. The incorporation of bentonite was expected to improve textural and surface properties by increasing the specific surface area, enhancing adsorption capacity, and facilitating charge separation. Experimental findings confirmed that the bentonite support exerts a synergistic role, significantly improving photocatalytic performance. In particular, the 50% TiO_2–BN composite exhibited the best compromise between adsorption and photocatalytic activity, achieving a degradation efficiency of 99.64%. Furthermore, kinetic studies revealed that the photocatalytic degradation of RhB followed a pseudo-first-order model consistent with the Langmuir-Hinshelwood (L–H) mechanism, thereby providing insights into the reaction pathway and rate-determining steps. These results highlight the crucial influence of synthesis method, calcination temperature, and support material on the overall photocatalytic efficiency, offering a comprehensive understanding of how structural, morphological, and surface properties govern the reactivity of TiO_2-based catalysts.

The thesis is organized into three main chapters:

- **Chapter I** provides an in-depth literature review covering water pollution by refractory organic pollutants, limitations of conventional treatments, principles of AOPs, and a particular focus on TiO_2-based photocatalysis and its modification strategies.
- **Chapter II** describes the experimental methodology, including the synthesis procedure, characterization techniques, and photocatalytic testing protocols.
- **Chapter III** presents and discusses the experimental results, starting with pure TiO_2 nanoparticles, followed by TiO_2–bentonite composites, and culminating in a detailed kinetic analysis of the photocatalytic degradation process.
- **Chapter IV** devoted to kinetics and comparative evaluation) quantifies the degradation rates for RhB over TiO_2 and TiO_2-BN, validates the L-H kinetic formalism, and establishes a head-to-head performance comparison between TiO_2-400 and 50% TiO_2-BN**.**

Overall, this research contributes to the development of sustainable, efficient, and environmentally friendly oxidation processes for the elimination of refractory organic pollutants. The findings not only advance fundamental understanding of the structure–activity relationship in TiO_2-based photocatalysts but also provide practical insights for the design of next-generation water treatment technologies.

References:

[1] A. K. Worku *et al.*, “Recent advances in wastewater treatment technologies: Innovations and new insights,” *Energy Reviews*, vol. 4, no. 4, p. 100164, Dec. 2025, doi: 10.1016/j.enrev.2025.100164.

[2] X. Jiang, K. L. Kirsten, and A. Qadeer, “Contaminants in the Water Environment: Significance from the Perspective of the Global Environment and Health,” *Water*, vol. 17, no. 9, p. 1257, Apr. 2025, doi: 10.3390/w17091257.

[3] J. Yi, J. Wan, J. Alemán, Y. Wang, S. Zuo, and J. Li, “Ligand-functionalized MOFs for efficient degradation of refractory organic pollutants in water: Unraveling the synergistic mechanism of adsorption and catalysis,” *Surfaces and Interfaces*, vol. 77, p. 108059, Nov. 2025, doi: 10.1016/j.surfin.2025.108059.

[4] R. Al-Tohamy *et al.*, “A critical review on the treatment of dye-containing wastewater: Ecotoxicological and health concerns of textile dyes and possible remediation approaches for environmental safety,” *Ecotoxicology and Environmental Safety*, vol. 231, p. 113160, Feb. 2022, doi: 10.1016/j.ecoenv.2021.113160.

[5] Kusumlata, B. Ambade, A. Kumar, and S. Gautam, “Sustainable Solutions: Reviewing the Future of Textile Dye Contaminant Removal with Emerging Biological Treatments,” *Limnological Review*, vol. 24, no. 2, pp. 126–149, Apr. 2024, doi: 10.3390/limnolrev24020007.

[6] A. Wołowicz and H. M. S. Munir, “Emerging organic micropollutants as serious environmental problem: A comprehensive review,” *Science of The Total Environment*, vol. 958, p. 177948, Jan. 2025, doi: 10.1016/j.scitotenv.2024.177948.

[7] A. Majeed, M. A. Iqbal, and T.-O. Do, “Advances in Composite Photocatalysts for Efficient Degradation of Organic Pollutants: Strategies, Challenges, and Future Perspectives,” *Catalysts*, vol. 15, no. 9, p. 893, Sep. 2025, doi: 10.3390/catal15090893.

[8] E. D. Huang Kong *et al.*, “Recent advances in titanium dioxide bio-derived carbon photocatalysts for organic pollutant degradation in wastewater,” *iScience*, vol. 28, no. 5, p. 112368, May 2025, doi: 10.1016/j.isci.2025.112368.

[9] Y. Kumar, S. Kumar, and J. Sangwai, “Effect of Clay on the kinetics of CO2 hydrate relevant for Carbon Capture and Sequestration”.

[10] H. Zhou *et al.*, “Photocatalytic degradation by TiO_2-conjugated/coordination polymer heterojunction: Preparation, mechanisms, and prospects,” *Applied Catalysis B: Environmental*, vol. 344, p. 123605, May 2024, doi: 10.1016/j.apcatb.2023.123605.

[11] W. Fang *et al.*, “Account of doping photocatalyst for water splitting,” *Chinese Journal of Catalysis*, vol. 60, pp. 1–24, May 2024, doi: 10.1016/S1872-2067(23)64637-6.

Chapter I: Literature review

1. Introduction:

Refractory organic pollutants (ROPs), including synthetic dyes, pharmaceuticals, pesticides, and industrial chemicals, constitute a significant category of persistent contaminants that withstand conventional water treatment methods. This chapter provides a comprehensive overview of the latest advancements in catalytic advanced oxidation processes (AOPs), with a particular focus on heterogeneous photocatalysis involving titanium dioxide (TiO_2) and its composites. It addresses the physicochemical characteristics of ROPs, their persistence in aquatic environments, and the detrimental ecological and human health impacts they have. Due to their chemical stability and resistance to biodegradation, ROPs present a significant challenge in wastewater remediation. The chapter also reviews the mechanisms and operational parameters of key AOPs such as TiO_2-based photocatalysis and related catalytic systems. It emphasises the influence of factors such as pH, light source, oxidants, and catalyst structure. Special attention is given to the modification of TiO_2 with clay-based supports, particularly bentonite, to enhance photocatalytic activity, improve pollutant adsorption, and mitigate limitations such as rapid electron-hole recombination. Overall, this review identifies existing research gaps and situates the scientific contribution of the present study within the broader field of environmental nanotechnology and sustainable water treatment.

2. Refractory organic pollutants (ROPs):

2.1. Definition and sources of (ROPs):

Refractory organic pollutants (ROPs), also known as persistent organic pollutants (POPs), are a notable group of hazardous substances that resist natural degradation processes. These pollutants include various synthetic organic compounds such as dyes, pharmaceuticals, pesticides, polycyclic aromatic hydrocarbons (PAHs), and endocrine-disrupting chemicals (EDCs), which are defined by their chemical stability, hydrophobic nature, and low biodegradability. Due to their persistent properties, ROPs are frequently detected in industrial and municipal wastewater, posing significant risks to aquatic ecosystems and human health through bioaccumulation and long-distance environmental transport [1]. Traditional treatment methods, such as biological oxidation, coagulation-flocculation, and adsorption, often fail to fully degrade these contaminants, creating a need for more effective and sustainable technologies like advanced oxidation processes (AOPs) [2,3]. The difficulty in degrading ROPs stems not only from their structural diversity but also from their interactions with coexisting matrix components and resistance to microbial breakdown, which makes their removal a major engineering and environmental challenge.

2.2. Physicochemical properties and persistence:

Refractory organic pollutants (ROPs) are a diverse group of synthetic and naturally occurring compounds characterized by high chemical stability, low biodegradability, and long environmental half-lives as shown in table I.1. Their physicochemical properties, such as low water solubility, high molecular weight, hydrophobicity (often indicated by high octanol-water partition coefficients, log K_ow), and strong aromaticity, contribute to their resistance to conventional biological treatment and environmental degradation processes [9,10]. These features enable ROPs to persist in surface waters, sediments, and even groundwater for extended periods. Many ROPs also exhibit volatility and semi-volatility, leading to atmospheric dispersion and long-range environmental transport. Their pronounced chemical resilience is primarily attributed to structural motifs such as halogen substituents, extended π-conjugated systems, and heterocyclic frameworks that confer stability and impede both oxidative transformation and microbial degradation[11]. Consequently, ROPs tend to accumulate within biological tissues and persist in environmental compartments, thereby reinforcing their designation as persistent, bioaccumulative, and toxic (PBT) substances [12]. This persistence presents major challenges for water treatment facilities, necessitating the development of more robust, advanced treatment technologies such as catalytic advanced oxidation processes (AOPs).

Table I.1. Common refractory organic pollutants in wastewater and their characteristic.

Pollutant class	Examples	Sources	Properties	Ref
Synthetic dyes	Rhodamine B, Methylene Blue	Textile, cosmetics, and dyeing industries	Highly stable, low biodegradability	[4]
Pharmaceuticals & PPCPs	Carbamazepine, Diclofenac, Ibuprofen	Hospitals, households	Persistent, endocrine-disrupting	[5]
Pesticides & agricultural chemicals	Atrazine, Chlorpyrifos	Agricultural runoff	Toxic, persistent	[6]
PAHs & heterocyclic organics	Benzo[a]pyrene, Quinoline, Indole	Petrochemical processes, coking plants	Carcinogenic, low biodegradation	[7]
Surfactants & phenolic compounds	Nonylphenol, Bisphenol A	Detergents, plastics	Endocrine-disrupting, refractory	[8]

2.3. Environmental and health impacts:

Refractory organic pollutants (ROPs) pose significant environmental and public health risks due to their persistence, toxicity, and potential for bioaccumulation. Once released into the environment through industrial discharges, agricultural runoff, or domestic wastewater, ROPs can persist in surface and groundwater, sediments, and even atmospheric compartments, where they undergo long-range transport and transformation into equally or more toxic byproducts [13]. Ecologically, these compounds can disrupt aquatic life by interfering with endocrine systems, altering reproductive cycles, and causing genetic mutations in fish, invertebrates, and microorganisms. For humans, chronic exposure via contaminated water, food chains, or inhalation has been linked to carcinogenicity, neurotoxicity, and developmental disorders [14]. Particularly concerning are dyes, pharmaceuticals, pesticides, and phenolic compounds, which exhibit high toxicity even at trace concentrations. The resilience of ROPs to biodegradation further exacerbates their health effects, as conventional wastewater treatment systems often fail to fully remove them, leading to continuous environmental cycling and human exposure[15]. These threats underscore the urgent need for advanced remediation strategies that can mineralize or degrade such pollutants into harmless byproducts.

2.4. Rhodamine B as a model compound in photocatalytic degradation studies:

Rhodamine B (RhB) is a xanthene-based synthetic dye widely employed in the textile, paper, leather, and food industries due to its brilliant pink colour and high photostability. Despite its industrial utility, RhB is considered a model pollutant for evaluating the efficiency of wastewater treatment technologies owing to its persistent, toxic, and non-biodegradable nature. Its molecular structure includes aromatic rings and amino groups, which confer stability against microbial degradation and contribute to its resistance to conventional biological treatment methods [16]. Rhodamine B (RhB) constitutes a significant environmental contaminant with pronounced ecotoxicological and human health implications. Within aquatic ecosystems, it can attenuate photosynthetic efficiency by diminishing light penetration, thereby perturbing primary productivity and destabilising trophic dynamics. In humans, its carcinogenic and mutagenic potential has been attributed to its propensity to intercalate into the DNA double helix, consequently compromising genomic integrity and promoting aberrant cellular processes[17]. Furthermore, its intense colouration makes even low concentrations environmentally problematic, as it causes aesthetic and ecological damage [18]. Owing to these characteristics, Rhodamine B is widely employed as a model compound in advanced oxidation process (AOP) research for benchmarking the performance of photocatalytic and catalytic systems designed for the degradation of refractory organic pollutants.

3. Overview of advanced oxidation processes (AOPs):

3.1. General principles and reactive oxygen species (ROS):

Advanced oxidation processes (AOPs) are chemical treatment technologies that utilize the generation of highly reactive oxygen species (ROS), particularly hydroxyl radicals ($^{\bullet}OH$), to initiate and drive the oxidative breakdown of recalcitrant organic pollutants in aqueous environments. These radicals possess a high oxidation potential ($E^0 = +2.80$ V) and are capable of non-selectively attacking a broad range of organic molecules, ultimately leading to their degradation [19], [20]. AOPs typically involve the in situ generation of ROS through various activation mechanisms such as ultraviolet (UV) irradiation, ozonation, Fenton and photo-Fenton reactions, and heterogeneous photocatalysis using semiconductors like titanium dioxide (TiO_2) [21], [22]. In addition to hydroxyl radicals, other reactive species such as superoxide anions ($O_2^{\bullet-}$), singlet oxygen ($^1O_2$), and hydrogen peroxide (H_2O_2) may also participate in the oxidation process, with their generation and relative contributions being contingent upon the nature of the catalyst and the prevailing operational conditions [23].

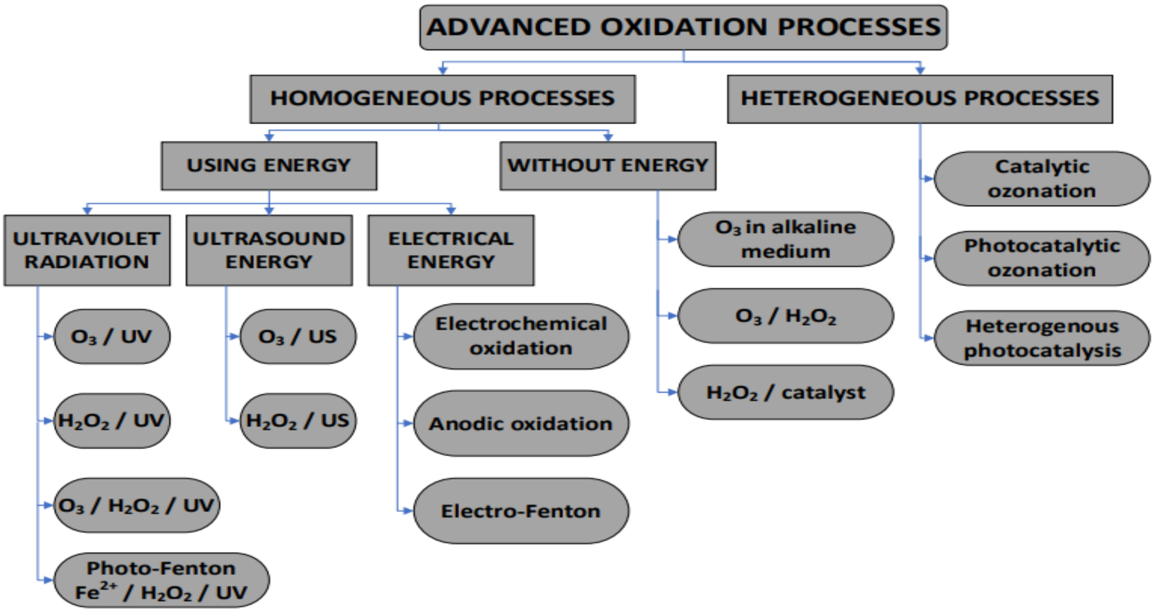

Figure I.1 Classification of advanced oxidation processes techniques [24].

Several parameters, including pH, oxidant concentration, light intensity, and the chemical nature of the target contaminants, govern the efficiency of AOPs. Owing to their high oxidative capacity and minimal generation of harmful by-products, advanced oxidation process are widely recognised as among the most effective and environmentally sustainable technologies for the remediation of persistent organic pollutants in wastewater [25]. An overview of the main types of AOPs, including homogeneous and heterogeneous processes with and without energy input, is presented in Figure I.1.

3.2. Homogeneous processes:

Homogeneous advanced oxidation processes (AOPs) involve the generation of reactive oxygen species (ROS) within a single-phase system, typically an aqueous solution, where both the oxidants and catalysts are present in the same phase. These processes are characterized by fast reaction kinetics and high degradation efficiency due to the uniform distribution of reactants[26]. Common homogeneous AOPs include the classical Fenton and photo-Fenton reactions, in which ferrous ions (Fe^{2+}) catalyze the decomposition of hydrogen peroxide (H_2O_2) to generate hydroxyl radicals ($^{\bullet}OH$). This process can be enhanced under UV or visible light irradiation to improve radical production [27]. Other homogeneous systems include UV/H_2O_2, O_3/H_2O_2, and electro-Fenton processes, which may be further intensified by external energy inputs such as ultraviolet light, ultrasound, or electrical current [28]. While these techniques are highly effective for degrading a wide range of refractory organic pollutants, their efficiency strongly depends on operational parameters such as pH, oxidant dosage, and the presence of radical scavengers. Moreover, challenges related to iron sludge generation and catalyst recovery limit the long-term environmental sustainability of homogeneous systems, motivating a growing interest in heterogeneous alternatives [29].

3.3. Heterogeneous processes: semiconductor-based photocatalysis:

Heterogeneous advanced oxidation processes (AOPs), particularly those based on semiconductor photocatalysis, have gained increasing attention for the degradation of refractory organic pollutants due to their high efficiency and environmental compatibility. In these systems, the photocatalyst, typically a semiconductor such as titanium dioxide (TiO_2), is activated by light irradiation, usually in the UV or visible range, generating electron-hole pairs (e^-/h^+) on its surface (equation I.1). The photogenerated electron can be trapped by oxygen to form superoxide ($O_2^{\bullet-}$) and hydroperoxyl radicals ($HO_2^{\bullet}$), and subsequently hydrogen peroxide (H_2O_2) (equations 2-7). The charge carriers interact with water and dissolved oxygen to form reactive oxygen species, primarily hydroxyl radicals ($^{\bullet}OH$) and superoxide anions ($O_2^{\bullet-}$), which oxidize the pollutants adsorbed on the catalyst surface as shown in the equations below [30],[31]:

$TiO_2 + h\nu \rightarrow e^{-}_{(CB)} + h^{+}_{(VB)}$ (Equation I.1)

$h^{+} + H_2O \rightarrow HO^{\bullet}$ (Equation I.2)

$h^{+} + OH^{-} \rightarrow HO^{\bullet}$ (Equation I.3)

$e^{-} + O_2 \rightarrow O_2^{\bullet -}$ (Equation I.4)

$O_2^{\bullet -} + H+ \rightarrow HOO^{\bullet}$ (Equation I.5)

$HOO^{\bullet} + e^{-} \rightarrow HO_2^{-}$ (Equation I.6)

$HO_2^{-} + H^{+} \rightarrow H_2O_2$ (Equation I.7)

In contrast to homogeneous systems, heterogeneous photocatalysis offers significant operational advantages, notably the ease of catalyst separation and recovery, the potential for repeated reuse with minimal loss of catalytic performance, and applicability across a broader pH spectrum. TiO_2 remains the most studied photocatalyst due to its strong oxidative potential, non-toxicity, low cost, and photochemical stability. However, its performance is limited by rapid electron-hole recombination and weak absorption in the visible light region [22]. To address these limitations, recent research has focused on modifying TiO_2-based photocatalysts through strategies such as metal/non-metal doping, heterojunction formation, and the development of composite materials. These modifications aim to enhance charge carrier separation and extend the optical absorption range into the visible spectrum, thereby improving photocatalytic efficiency [25,32].

Table I.2. Recent studies on Rhodamine B degradation using TiO_2-based advanced oxidation processes (AOPs).

AOP Type	Catalytic process	Key Experimental Conditions	R (%)	Ref
Synthesized TiO_2 Via the sol-gel method (Photocatalysis)	TiO_2/UV	$[TiO_2]_0$= 0.3 g.L^{-1} $[RhB]_0$=6 mg L^{-1} pH 5, UV lamp λ_{max}(nm) 280–100	99.8	[33]
Visible-Light Photocatalysis	N-doped TiO_2 / Bentonite Composite	RhB 20 mg/L; pH 5.5; 1 g/L catalyst; λ > 420 nm; 120 min	90.4	[34]
Photo-Fenton-Like Process	TiO_2–Fe_3O_4 Composite	RhB 15 mg/L; pH 3.0 UV-A light; 0.5 g/L catalyst; 60 min	96.7	[35]
Ozone-Assisted Photocatalysis	TiO_2-graphene oxide composite + O_3	RhB 25 mg/L; O_3 flow 1 L/min; TiO_2-GO 1 g/L; UV-C light; 90 min	>95	[36]
Visible-Light / Ultrasound	TiO_2-WO_3 Nanocomposite	RhB 10 mg/L; ultrasound (20 kHz); visible light; pH 6; 0.5 g/L catalyst; 90 min	93.5	[37]

A variety of studies have reported the successful application of advanced TiO_2-based materials for the degradation of Rhodamine B. A summary of selected recent studies demonstrating the effectiveness of TiO_2-based AOPs for Rhodamine B degradation is presented in Table I.2, highlighting the influence of catalyst composition, irradiation source, and operational parameters on photocatalytic performance. Figure I.2 illustrates the bibliometric trends in publications on nano-TiO_2 and TiO_2-based AOPs from 2000 to 2022. Both research areas display a steady growth trajectory until around 2019, followed by a plateau and a slight decline in subsequent years. Publications on nano-TiO_2 consistently outnumber those on AOP-TiO_2, although both follow similar growth patterns, reflecting sustained global interest in TiO_2 for environmental applications. The pronounced increase between 2015 and 2019, particularly for AOP-TiO_2, suggests intensified research efforts in photocatalytic technologies, likely driven by advances in synthesis techniques, visible-light activation strategies, and the escalating demand for sustainable water and wastewater treatment solutions.

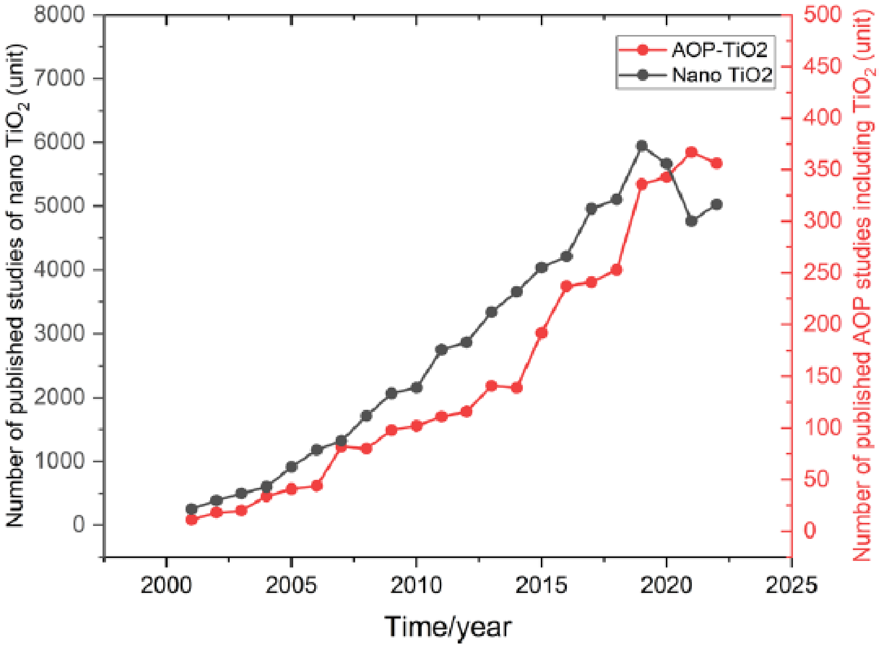

Figure I.2. Number of publications per year on the topic of TiO_2 and AOP based on the ISI Web of Science [38].

3.4. Heterogeneous processes *vs* Homogeneous processes:

The distinction between heterogeneous and homogeneous processes lies in the phase distribution of the catalyst relative to the reactants, which significantly affects the reaction mechanisms, efficiency, and practical applicability of the treatment method. In homogeneous processes, all the reactive species and catalysts are present in the same phase, typically the aqueous phase. This configuration allows for rapid diffusion and high reaction rates due to the intimate contact between the reactants. A classic example is the Fenton reaction, where ferrous ions (Fe^{2+}) catalyze the decomposition of hydrogen peroxide (H_2O_2) to generate hydroxyl radicals ($^{\bullet}OH$), which are highly effective in degrading a wide range of organic pollutants [39]. Despite their high efficiency, homogeneous processes are constrained by several operational limitations, including a restricted optimal pH range typically in the acidic range, challenges associated with catalyst recovery, the generation of secondary pollutants such as iron-rich sludge, and the necessity for continuous chemical dosing, all of which collectively compromise their long-term sustainability and economic viability in large-scale applications [40]. In contrast, heterogeneous processes involve catalysts that exist in a different phase from the reactants, most commonly as solid catalysts interacting with liquid-phase pollutants. This separation offers several operational benefits, including easier catalyst recovery and reuse, reduced risk of secondary pollution, and improved stability in varying environmental conditions [41]. Titanium dioxide (TiO_2)-based photocatalysis is a well-established heterogeneous advanced oxidation process that has been extensively investigated for environmental remediation. Upon irradiation with ultraviolet or solar light, TiO_2 generates reactive oxygen species (ROS), including hydroxyl radicals ($^{\bullet}OH$) and superoxide anions ($O_2^{\bullet-}$), which are capable of initiating oxidative pathways leading to the degradation and complete degradation of organic pollutants [42]. Furthermore, Heterogeneous photocatalytic systems demonstrate robust performance across a broad pH range. Recent research has increasingly focused on enhancing their visible-light responsiveness through advanced strategies such as elemental doping, surface functionalization, and heterojunction engineering. Despite these advances, several intrinsic limitations remain. Photocatalytic activity can be hindered by low quantum efficiency, rapid electron-hole recombination, and mass transfer resistances at the solid-liquid interface. Moreover, the immobilisation of catalysts, although beneficial for post-treatment recovery and reusability, often reduces the accessible active surface area, thereby diminishing degradation kinetics. Nevertheless, heterogeneous photocatalysis is gaining prominence in sustainable water and wastewater treatment due to its recyclability, long-term stability, and compatibility with environmentally benign technologies. The choice between homogeneous and heterogeneous systems is determined by multiple factors, including contaminant characteristics, treatment objectives, cost–benefit considerations, and environmental impact. Current research increasingly favours hybrid configurations that integrate the advantages of both approaches, for example, employing immobilised iron-based catalysts in photo-Fenton reactions to address system-specific limitations and achieve superior degradation performance [41,43,44].

3.5. Influence of key operational parameters on advanced oxidation processes:

The efficiency of advanced oxidation processes (AOPs) is strongly influenced by several operational parameters, with pH, light source, oxidant type, and catalyst properties being particularly critical. The pH of the reaction medium affects not only the speciation of oxidants (e.g., H_2O_2, O_3) but also the surface charge of catalysts and the stability of reactive oxygen species, such as hydroxyl radicals. For instance, Fenton and photo-Fenton reactions exhibit optimal performance under acidic conditions (typically around pH 3), whereas heterogeneous photocatalysis with TiO_2 can function across a broader pH spectrum. Nonetheless, its activity is generally enhanced under slightly acidic to neutral conditions [25,45]. The light source represents a critical operational parameter, as it dictates the photoactivation efficiency of semiconductor catalysts. Ultraviolet (UV) irradiation has traditionally been employed to excite wide-bandgap materials such as TiO_2; however, recent advancements increasingly prioritise visible-light activation to enhance the utilisation of solar energy. This objective is pursued through tailored modification strategies including elemental doping, dye sensitisation, and heterojunction engineering, which extend the optical absorption range, promote efficient charge separation, and thereby improve photocatalytic performance. [46,47]. The type and concentration of oxidants exert a decisive influence on the generation of reactive species; however, excessive dosages can induce scavenging effects, thereby diminishing overall degradation efficiency. The catalyst's properties, including surface area, crystallinity, bandgap energy, and morphology, affect pollutant adsorption and the rate of ROS production. Advances in catalyst engineering, such as doping and the development of composite materials, aim to enhance charge separation and broaden light absorption, thereby improving photocatalytic performance [48]. Therefore, optimizing these key parameters is essential for achieving high degradation rates, process stability, and environmental sustainability.

3.5. Recent advances in AOPs for the degradation of refractory organic pollutants:

Advanced oxidation processes (AOPs) have seen significant strides in treating refractory organic pollutants, those that defy conventional degradation due to their chemical stability and low biodegradability. One noteworthy innovation involves spherical metal oxides (SMOs) with engineered morphologies, such as hollow, yolk-shell, porous shell, and nanoflower structures, that promote enhanced light absorption, improved diffusion of reactive oxygen species (ROS), and heightened antibiotic degradation efficiency [49,50,51]. Additionally, composites of BiOI and HKUST-1 have been proven effective for the visible-light activation of persulfate, achieving up to 94.9% degradation of the azo dye Orange II within 60 minutes under optimized conditions [52]. Electrochemical oxidation, producing reactive species directly at electrode surfaces without added chemicals, continues to attract attention as an effective approach for breaking down complex pollutants, including pharmaceuticals and dyes [53]. Beyond advancements in individual processes, a recent systematic literature review underscores the sustainability potential of AOPs for the treatment of refractory wastewater, noting that pollutant removal efficiencies frequently exceed 96%, sludge generation is minimal, and effluent biodegradability is enhanced, thereby facilitating scalable and environmentally sustainable treatment solutions [26]. Furthermore, integrating AOPs with complementary techniques, such as membrane filtration [29], electro-Fenton methods [53], and biological catalysts [54], has demonstrated synergistic effects, including higher selectivity, lower toxic by-products, and improved energy efficiency, particularly in complex wastewater cases. These developments demonstrate how innovative material structures, electrochemical enhancements, and hybrid system designs support the next generation of strong, scalable, and environmentally friendly AOPs for degrading persistent and hazardous organic pollutants.

4. Sol-gel method:

4.1. Definition:

The sol-gel method is a versatile wet-chemical synthesis technique widely employed for the preparation of inorganic materials, particularly metal oxides, with controlled composition, morphology, and microstructure. It involves the transition of a colloidal suspension (sol) into a three-dimensional continuous network (gel) through hydrolysis and polycondensation reactions of molecular precursors, typically metal alkoxides or inorganic salts [54]. This process operates under relatively low temperatures, enabling the production of materials with high purity, tunable porosity, and nanoscale particle sizes, making it particularly attractive for applications in photocatalysis, optics, sensors, and coatings [55].

4.2. Sol-gel reactions:

The sol-gel process proceeds through a sequence of hydrolysis and condensation reactions of metal alkoxide precursors, culminating in the formation of a three-dimensional oxide network. In the initial stage, metal alkoxides $M(OR)_n$, such as titanium tetraisopropoxide (TTIP), undergo hydrolysis (equation I.8), where hydroxyl groups replace alkoxy groups through nucleophilic attack by water molecules. This step is followed by condensation reactions (Equation I.9-10), which may proceed through either oxolation or alkoxolation pathways, generating metal-oxygen-metal (M-O-M) linkages and releasing small molecules such as alcohol or water. Ultimately, the transformation from a colloidal sol to a continuous gel network occurs, and subsequent drying and thermal treatment yield the targeted oxide material [38], [56]. The general reactions can be represented as [57]:

a) Hydrolysis

$M(OR)_n + H_2O \rightarrow M(OR)_{n-1}(OH) + ROH$ (Equation I.8)

b) Condensation

(1) *Oxolation* (water release):

$M\text{-}OH + M\text{-}OH \rightarrow M\text{-}O\text{-}M + H_2O$ (Equation I.9)

(2) *Alcoxolation* (alcohol release):

$M\text{-}OR + M\text{-}OH \rightarrow M\text{-}O\text{-}M + ROH$ (Equation I.10)

These reactions are influenced by parameters such as precursor type, water/alkoxide molar ratio, pH, temperature, and the presence of catalysts, all of which determine the microstructure, porosity, and crystallinity of the final oxide material [56].

4.3. Types of Sol-gel Processes:

Sol-gel processes can be broadly categorized based on the nature of the precursor and the reaction pathway employed during synthesis[58]. Two principal approaches are commonly distinguished: (i) the aqueous sol-gel route, which using metal alkoxides or inorganic salts undergoing hydrolysis and condensation in water, and (ii) the non-aqueous sol-gel route, where organic solvents serve as the reaction medium, often enabling greater control over hydrolysis kinetics and particle morphology. The aqueous method is typically favoured for its cost-effectiveness and environmental compatibility. In contrast, the non-aqueous approach offers enhanced tunability of nanoparticle characteristics, such as crystallinity, surface area, and porosity, due to the reduced rate of uncontrolled hydrolysis [59]. Hybrid sol-gel processes, which integrate organic and inorganic components, have also emerged to produce organic-inorganic nanocomposites with tailored functionalities for specific applications [60]. The selection of a particular sol-gel type depends on factors such as the targeted material properties, precursor availability, and intended application in fields ranging from catalysis to biomedical engineering. As conventional sol-gel methods are often limited by long reaction times and poor crystallinity, non-conventional sol-gel approaches have been developed to enhance the structural and photocatalytic properties of TiO_2 [61].

4.4. Factors influencing the Sol-gel method:

The sol-gel method is susceptible to a range of physicochemical parameters that collectively govern the structure, morphology, and performance of the final material. Key factors include the precursor type and concentration, which determine the hydrolysis and condensation kinetics, as alkoxide precursors such as titanium isopropoxide (TTIP) hydrolyze at different rates depending on their alkyl chain length and steric effects [56,62]. The pH of the reaction medium critically influences the mechanism: acidic conditions generally promote linear polymeric networks via slower condensation, whereas basic conditions favour rapid nucleation and branched structures [63]. Water /alkoxide molar ratio (R) plays a pivotal role, with higher ratios accelerating hydrolysis but risking uncontrolled precipitation [64]. The type and concentration (acidic or basic) of catalyst alter both the rate and direction of sol-gel reactions, impacting particle size and porosity[62]. Furthermore, temperature and ageing time govern the extent of polycondensation and network crosslinking, thereby affecting crystallinity and surface area [59]. Finally, drying and calcination conditions dictate the removal of residual organics and the phase composition of the oxide, which in turn influences photocatalytic activity [65]. Optimization of these parameters is therefore essential to tailor the physicochemical properties of sol-gel-derived TiO_2 for specific applications such as photocatalysis.

5. Titanium dioxide (TiO_2) as a photocatalyst:

Titanium dioxide (TiO_2) is one of the most widely studied and applied photocatalysts due to its high oxidative potential, photostability, non-toxicity, and low cost[66]. Upon UV or near-UV irradiation, TiO_2 generates electron-hole pairs that participate in redox reactions, leading to the formation of reactive oxygen species (ROS) capable of degrading a wide range of organic pollutants. Among its polymorphs, anatase typically exhibits superior photocatalytic activity compared to rutile and brookite due to its higher surface area and charge carrier mobility. However, its wide band gap (~3.2 eV) limits its activation to UV light, which comprises only a small fraction of the solar spectrum. Recent research has focused on enhancing its visible-light activity through doping with metals or non-metals, surface modification, and heterojunction formation [67,68]. These advancements aim to expand their applicability in environmental remediation, particularly in wastewater treatment.

5.1. Principal crystallographic forms of Titanium dioxide:

5.1.1. TiO_2 rutile:

Rutile (Figure I.1.A) constitutes the most abundant polymorph of titanium dioxide. Its name derives from its red hue, although it may also occur in yellow or black varieties. Rutile crystallises in a tetragonal Bravais lattice [69].

Structurally, rutile and anatase represent the most widespread crystalline forms of TiO_2. Its atomic arrangement is as follows: each TiO_6 octahedron shares two opposite edges with adjacent octahedra, forming one-dimensional chains aligned along the *c*-axis. These chains are interconnected with four neighbouring chains via corner-sharing.

The oxygen planes and titanium-vacancy planes, oriented parallel to (100) and (010), are separated by a short interplanar spacing of $d(100) = 1.148$ Å, conferring a relatively high density ($d = 4.24\ g\cdot cm^{-3}$) to rutile [66]. Vacancies within the titanium sublattice generate square-section tunnels along the [001] crystallographic direction. Morphologically, the rutile typically occurs as elongated prismatic crystals, in contrast to the octahedral habit of anatase. Above approximately 700 °C, anatase undergoes an irreversible phase transformation into rutile [70].

5.1.2. TiO_2 anatase:

Anatase Figure I.3 (B) represents another polymorphic form of titanium dioxide, crystallizing in the tetragonal system. Structurally, each TiO_6 octahedron shares edges with adjacent octahedra to form chains aligned along the *a*-axis, adopting a zigzag configuration along the *c*-axis. This chain motif is also encountered in other TiO_2 polymorphs and certain sodium titanates. The chains are interconnected via corner-sharing along the *b*-axis, producing structural blocks, which subsequently link along the *c*-axis through edge-sharing to generate a three-dimensional framework [112]. In the crystallographic orientation, both oxygen atom planes and titanium vacancy planes are discernible. These planes are separated by an interplanar spacing of $d_{(11-2)} = 1.166$ Å, slightly greater than that of rutile, resulting in a lower crystallographic density ($d = 3.92\ g\cdot cm^{-3}$). Cationic vacancies within the planes give rise to tunnel-like channels extending in two symmetrically equivalent crystallographic directions, (100) and (010) [71,72]. Upon thermal treatment between 630 and 1050°C, anatase undergoes an irreversible phase transformation into rutile, the thermodynamically most stable TiO_2 polymorph. The transformation temperature increases with crystallite size, reflecting the competition between surface and bulk free energies [70].

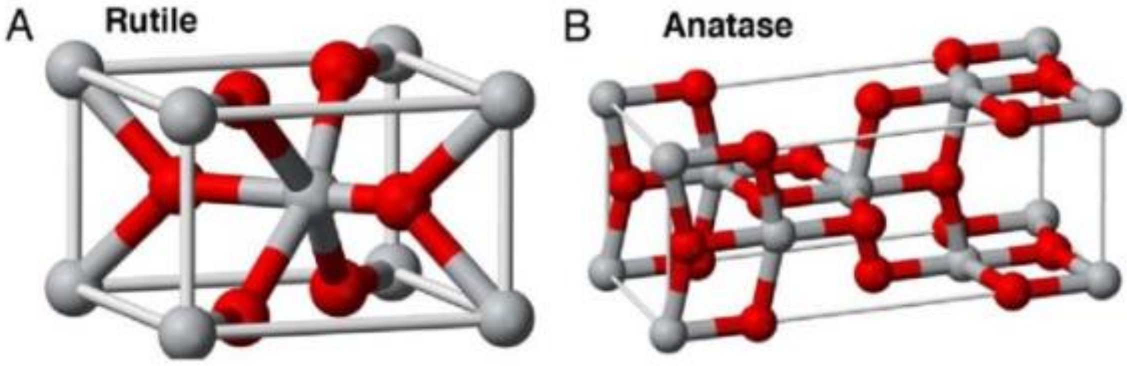

Figure I.3. Unit cell of (a) rutile and (b) anatase phases of TiO_2. The grey circles represent titanium atoms, and the red circles represent oxygen atoms. Both phases crystallize in the tetragonal system, with lattice constants *a* = 0.3785 nm and *c* = 0.9514 nm for anatase, and *a* = 0.4594 nm and *c* = 0.2958 nm for rutile, respectively [73].

5.2. Synthesis of TiO_2 nanoparticles via non-conventional sol-gel method:

Titanium dioxide (TiO_2) can be synthesized using various methods, each one provides a distinct control over morphology, crystallinity, and functional properties. Common approaches include hydrothermal and solvothermal synthesis[74], which promote crystal growth under elevated temperature and pressure; chemical vapor deposition [75], and physical vapor deposition [76] for precise thin-film fabrication; precipitation [77], and co-precipitation methods [78], which are cost-effective and straightforward but often yield a broader particle size distribution; and microwave-assisted [79] or green synthesis routes [80], which provide rapid and environmentally friendly processing.

The sol-gel process is a versatile and cost-effective technique for synthesizing metal oxide nanoparticles, enabling precise control over size, morphology, and crystallinity through mild reaction conditions[81]. For the non-conventional sol-gel approach, modifications to classical protocols such as using precursor/solvent ratios, unconventional solvents, pH adjustments, or modified hydrolysis/condensation sequences are introduced to optimize particle uniformity, phase composition, and photocatalytic activity [82]. Titanium alkoxides, particularly titanium isopropoxide (TTIP), remain the most common precursors due to their high reactivity toward hydrolysis. The reaction proceeds through hydrolysis [38]:

$Ti(OR)_4+4H_2O \rightarrow Ti(OH)_4+4ROH$ (Equation I.9) followed by condensation:

$Ti(OH)_4 \rightarrow TiO_2 + 2H_2O$ (Equation I.10)

In non-conventional sol-gel approaches, parameters such as acidic catalysis (e.g., HNO_3, HCl) under controlled pH conditions are employed to inhibit precipitation and facilitate the formation of well-dispersed nanoparticles with tunable anatase/rutile phase ratios. Recent investigations have introduced methodological variations, including the utilisation of ethanol-water mixtures under reflux, low-temperature drying before calcination, and the incorporation of additives such as surfactants or biotemplates to enhance porosity and specific surface area [83]. For instance, Lukong et al. [1] demonstrated that controlled acid hydrolysis at pH 3 followed by low-temperature drying yielded TiO_2 with high anatase purity and improved photocatalytic degradation of methylene blue [84]. Similarly, Nirmal Rajeev et al. synthesized mesoporous TiO_2 via a modified sol-gel route incorporating CTAB as a structure-directing agent, resulting in higher Congo red degradation rates under UV light [85]. Other studies investigate the synthesis of TiO_2 via non-conventional sol-gel method [86,87]. These non-conventional adaptations facilitate the precise engineering of particle physicochemical properties, thereby optimising their performance for targeted photocatalytic and environmental applications.

5.3. Parameters affecting the photocatalytic activity of TiO_2:

The photocatalytic performance of TiO_2 is strongly influenced by different physicochemical parameters that determine its crystal structure, surface area, charge carrier dynamics, and light absorption properties. Among the most critical factors are the calcination temperature, which governs phase composition and crystallinity, and the amount of incorporated secondary materials, such as clays, metal oxides, carbonaceous phases, or dopants, which can modify surface reactivity, charge separation efficiency, and pollutant adsorption capacity. The optimization of these parameters is essential for maximizing the degradation efficiency of target contaminants in advanced oxidation processes (AOPs) [42].

5.3.1. Effect of calcination temperature:

The calcination temperature is a key factor controlling the crystalline phase, crystallite size, and surface characteristics of TiO_2 nanoparticles. Anatase, the metastable phase with superior photocatalytic activity, generally forms at low to moderate calcination temperatures (300-500 °C) and gradually transforms into the thermodynamically stable rutile phase at higher temperatures (≥600 °C) [88]. While increasing calcination temperature enhances crystallinity and reduces bulk defects, thereby improving charge transport, it also promotes particle growth and reduces surface area, which can limit the number of active sites available for photocatalysis [89]. Optimal calcination temperatures, therefore, balance high crystallinity with sufficient surface area; for many sol-gel synthesized TiO_2 samples, this range is between 400 and 500 °C [90]. Beyond 700 °C, the anatase-to-rutile transition is typically complete, and the reduced band gap of rutile may shift light absorption toward the visible region. However, its higher electron-hole recombination rate often lowers photocatalytic efficiency. Adjusting calcination temperature according to the synthesis route and intended application is thus critical for achieving optimal activity in environmental remediation [91].

5.3.2. Effect of incorporated material content:

Incorporating secondary materials into TiO_2, such as natural clays, silica, alumina, graphene, carbon nanotubes, or metal oxides, can significantly influence its photocatalytic behaviour by modifying surface chemistry, morphology, and charge carrier dynamics [92]. The amount of the added phase is a crucial factor: low to moderate loadings often enhance photocatalytic activity by increasing surface area, improving pollutant adsorption, and promoting charge separation through heterojunction formation [93]. For example, coupling TiO_2 with layered clays such as bentonite can improve dispersibility and stability while reducing particle agglomeration, thereby preserving active surface sites [94]. In contrast, excessive incorporation may block light penetration to TiO_2 surfaces, introduce recombination centres, or dilute the active photocatalyst fraction, resulting in decreased performance as reported by Adhi Setiawan et al [34,95]. The optimal additive content depends on factors such as the additive type, synthesis method, and target pollutant. In many TiO_2-clay composites, the reported optimal range is typically between 10 % and 50 % by weight, as noted by Laysandera *et al.* [96]. Systematic optimization of the additive loading is therefore crucial to fully exploit synergistic effects while minimizing potential adverse impacts.

5.4. Photocatalytic mechanisms of TiO_2 and activation under UV/Visible light:

Figure I.4 illustrates the photocatalytic mechanism of TiO_2 under UV light irradiation. The photocatalytic activity of TiO_2 is primarily governed by its capacity to absorb photons and generate electron-hole (e^-/h^+) pairs, which subsequently trigger a cascade of redox reactions. Under UV irradiation ($\lambda \leq 387$ nm), photons possessing energy equal to or greater than the bandgap of anatase (~3.2 eV) or rutile (~3.0 eV) promote the excitation of electrons from the valence band to the conduction band, thereby leaving behind oxidizing holes (h^+). These photogenerated charge carriers participate in surface reactions: (h^+) oxidizes water or hydroxide ions to form highly reactive hydroxyl radicals ($^{\bullet}OH$), while e^- reduces molecular oxygen to superoxide radicals ($O_2^{\bullet-}$), both of which are potent oxidants responsible for degrading organic contaminants [97,98]. To extend activation into the visible spectrum, various strategies have been employed, such as doping with non-metals (e.g., N, F) or metals, and forming composites with carbonaceous materials or secondary oxides. Such modifications can introduce mid-gap states or reduce the effective bandgap, thereby enabling the excitation of electrons by lower-energy photons within the visible-light range. For example, N-F co-doped TiO_2 facilitates electron promotion from nitrogen-derived mid-gap states to the conduction band under visible-light irradiation. These states can subsequently be replenished via electron transfer from Ti^{3+} centres or oxygen vacancies, sustaining continuous charge excitation and the generation of reactive oxygen species (ROS) [99,100].

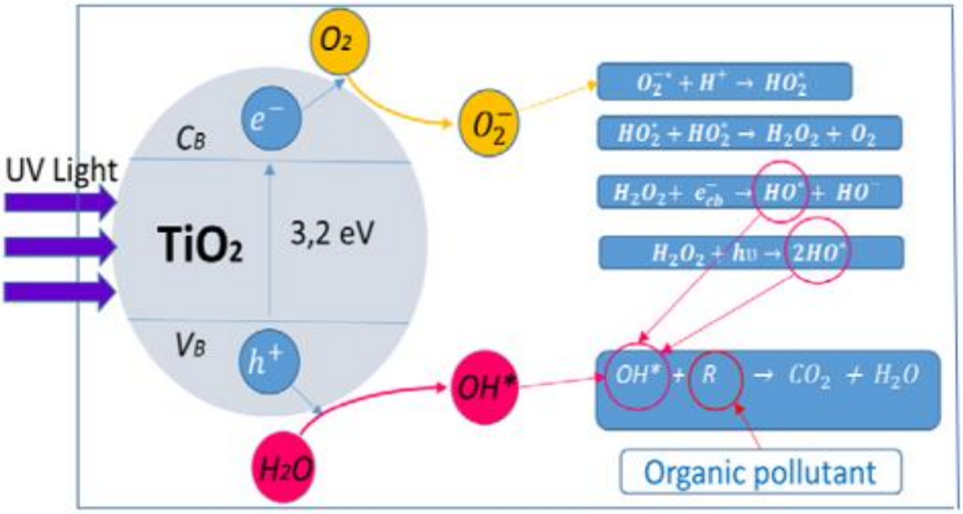

Figure I.4. Photocatalytic mechanism of TiO_2 [101].

Carbonaceous materials, such as graphene, act as electron sinks, facilitating charge separation and suppressing recombination by accepting photo-generated electrons from TiO_2 due to their favourable Fermi levels, which enhances photocatalytic efficiency [102]. Collectively, these UV- and visible-light-induced pathways demonstrate the dual mechanisms by which TiO_2 and its modified variants can harness solar spectra for environmental remediation, employing both high-energy excitation and engineered bandgap tailoring to utilise a broader range of light.

4.5. Limitations of TiO_2 photocatalysis:

Despite its excellent photocatalytic efficiency and chemical inertness, TiO_2 suffers from several intrinsic limitations that restrict its large-scale application. One of the primary drawbacks is the rapid recombination of photogenerated electron-hole (e^-/h^+) pairs, which significantly reduces the quantum efficiency of the photocatalytic process. This recombination competes with the redox reactions on the catalyst surface, thereby diminishing the generation of reactive oxygen species (ROS) [57,93]. Furthermore, the inherently wide bandgap of TiO_2 (~3.2 eV for anatase and ~3.0 eV for rutile) restricts its optical absorption predominantly to the ultraviolet region, which accounts for less than 5% of the solar spectrum. This spectral limitation substantially constrains its capacity to harness visible light for photocatalytic applications [3,4]. Additionally, TiO_2 undergoes progressive deactivation during repeated photocatalytic cycles due to surface passivation by adsorbed reaction intermediates, structural degradation under prolonged irradiation, or thermally induced phase transformations (e.g., anatase-to-rutile transition) at higher temperatures [100]. Addressing these limitations requires targeted strategies such as surface modification, heterojunction formation, doping with metals or non-metals, and coupling with narrow-band-gap semiconductors to extend the light absorption range and inhibit charge recombination [103].

5.6. Surface modification strategies of TiO_2:

Surface modification strategies are widely employed to overcome the intrinsic limitations of TiO_2, such as its wide band gap and rapid electron-hole recombination, thereby improving photocatalytic activity under both UV and visible light. Common approaches include doping with nonmetals (e.g., N, C, S) or metals (e.g., Fe, Ag, Pt), coupling with other semiconductors (ZnO, WO_3, CdS), and integrating TiO_2 with high-surface-area supports such as clays [104]. Clays, particularly bentonite, montmorillonite, and kaolinite, offer layered structures, abundant hydroxyl groups, and high cation exchange capacity, which enhance TiO_2 dispersion, prevent nanoparticle agglomeration, and provide additional adsorption sites for pollutants, facilitating improved mass transfer during photocatalysis [105,106]. Moreover, the intercalation of TiO_2 into clay layers can create hybrid materials with synergistic adsorption and degradation functions, increasing photocatalytic efficiency in complex water matrices [106]. Other modifications, such as sensitization with dyes or carbon-based materials (graphene, carbon nanotubes), further extend light absorption into the visible range and inhibit recombination [107]. As a whole, these strategies engineer the surface chemistry, morphology, and electronic structure of TiO_2 to align with the functional requirements of targeted environmental applications.

6. Clay:

Clay minerals have emerged as effective supports in photocatalysis due to their high surface area, layered structure, ion-exchange capacity, and tunable surface chemistry. Their incorporation with semiconductor photocatalysts, such as TiO_2, enhances the dispersion of active sites, improves light utilization, and facilitates pollutant adsorption, thereby promoting photocatalytic efficiency[108]. Moreover, clays such as bentonite, kaolinite, and montmorillonite provide structural stability, prevent nanoparticle aggregation, and enable controlled release of reactive species during photocatalytic reactions. The synergistic interaction between clay minerals and photocatalysts optimizes charge separation and enhances catalyst reusability, making clay-based composites promising candidates for sustainable water and wastewater treatment applications [109].

6.1. General characteristics of clays:

Clays are naturally occurring, fine-grained aluminosilicate minerals characterised by a layered phyllosilicate structure and particle sizes typically below 2 µm [110]. It exhibits high specific surface areas, significant cation exchange capacities (CEC), and variable surface charges, which give them notable adsorption and ion-exchange properties. Structurally, clay minerals consist of tetrahedral silica sheets and octahedral alumina or magnesia sheets arranged in various stacking sequences, leading to diverse clay types such as kaolinite, montmorillonite, and illite [111]. Their physicochemical properties, such as swelling capacity, thermal stability, and surface reactivity, are greatly influenced by their mineralogical composition, degree of crystallinity, and exchangeable cations. These features make clays versatile materials in environmental remediation, catalysis, and nanocomposite synthesis [108].

6.1.1. Mineralogy and crystallochemistry of clays:

Clay rocks are silico-aluminous sedimentary rocks, composed mainly of phyllosilicates along with various other compounds such as quartz, carbonates, and iron or aluminium oxides. Figure I.5 illustrates the terminology used to define the structure of clays. Four levels of organization can be distinguished for clay minerals or phyllosilicates [72]:

- *Planes* : formed by atoms.
- *Sheets*: tetrahedral or octahedral, formed by a combination of planes.

- *Layers*: correspond to combinations of sheets.
- *Crystal*: results from the stacking of several layers.

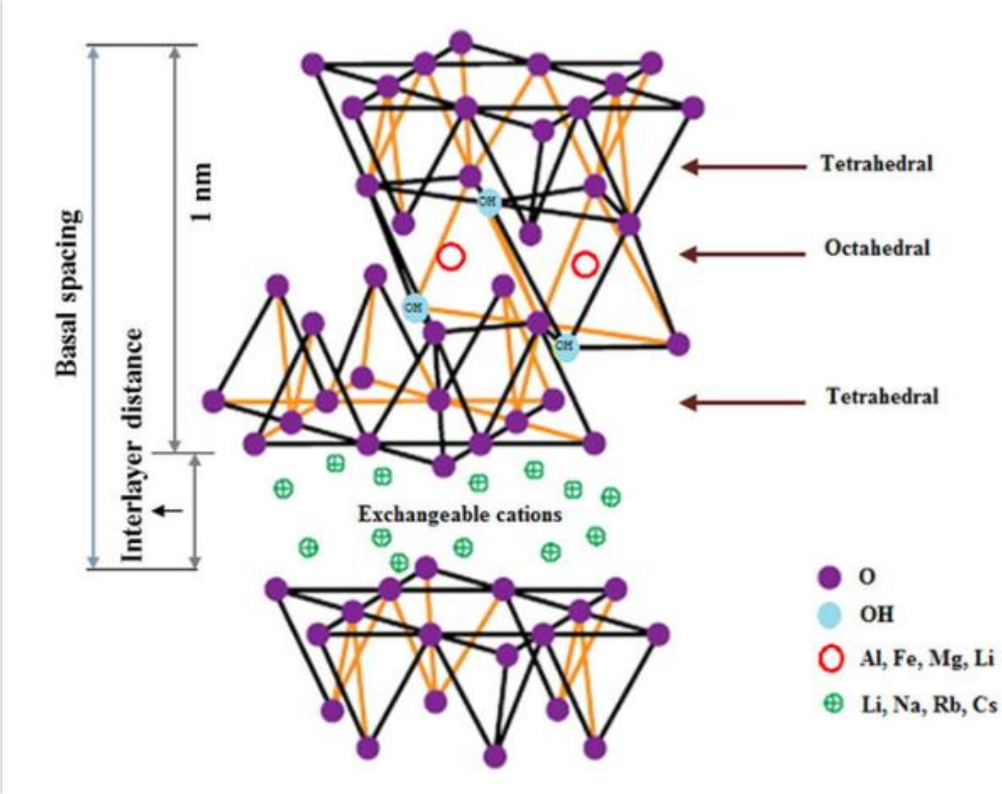

Figure I.5. Structure of phyllosilicates [112].

6.1.2. Structural elements of clay minerals:

Layered clays are phyllosilicates whose fundamental structural unit is the layer (Figure I.6). Each layer comprises a stacking of tetrahedral (T) and octahedral (O) sheets. These sheets are formed by the superposition of oxygen planes that define cavities with either tetrahedral or octahedral geometry. Incorporating cations within these cavities ensures the structural stability of the layer. Si^{4+} ions typically occupy tetrahedral sites, whereas octahedral sites host Al^{3+} or Mg^{2+} ions [113]. Others of different chemical nature may substitute these cations, but with comparable ionic radius, such as Al^{3+} and Fe^{3+} in tetrahedral sites, or Mg^{2+}, Fe^{3+}, Fe^{2+}, or Li^{+} in octahedral sites. Heterovalent substitutions (e.g., $Si^{4+} \rightarrow Al^{3+}$ or $Al^{3+} \rightarrow Fe^{2+}$) generate a charge imbalance, which is generally compensated by hydrated or non-hydrated cations in the interlayer space[114]. Different clay types are distinguished based on the nature of their layers.

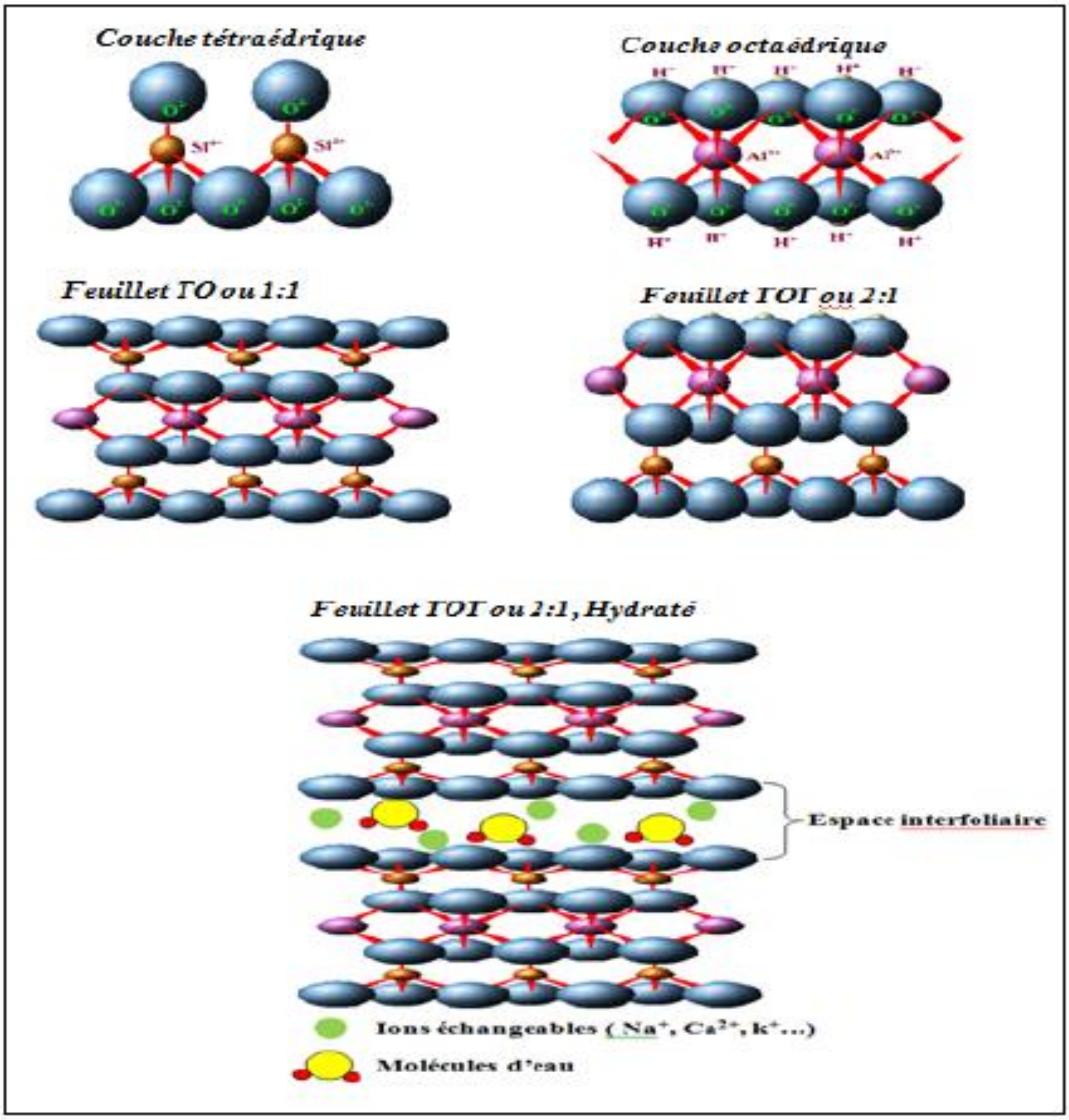

Figure I.6. Structure of clay [72].

6.1.3. Classification

The classification of clay minerals is primarily determined by the following structural parameters: *Layer stacking sequence*: T/O (1:1), T/O/T (2:1), or T/O/T/O (2:1:1), *Nature of the octahedral cations*, *Magnitude of the layer charge*, *Composition of the interlayer space*, including exchangeable cations, water molecules, or other species. Two principal layer types are commonly distinguished: **TO (1:1)** layers, composed of one tetrahedral (T) sheet directly bonded to one octahedral (O) sheet, and **TOT (2:1)** layers, consisting of an octahedral sheet sandwiched between two tetrahedral sheets.

Table I.3. Classification of phyllosilicates recommended by AIPEA**.** Examples of species occurring in soils are underlined. Species marked with an asterisk occur only in soils from Brazil and Georgia, USA, and are rare in temperate soils [72].

Layer Type	**Interlayer Filling**	**Layer Charge for $O_{10}(OH)_2$**	**Group**	**Subgroup *(based on octahedral nature)***	**Example**
1:1	Empty or H_2O	x ≈ 0	Serpentine-kaolinite	Serpentine (trioctahedral)	Berthierine, Odinite, Cronstedtite
				Kaolinite (dioctahedral)	Kaolinite
2:1	Empty	x ≈ 0	Talc–pyrophyllite	Talc (trioctahedral)	–
				Pyrophyllite (dioctahedral)	–
2:1	Hydrated exchangeable cations	x ≈ 0.2 to 0.6 (tetrahedral or octahedral)	Smectite	Saponite (trioctahedral)	–
				Montmorillonite (dioctahedral)	*Montmorillonite*
		x ≈ 0.2 to 0.9 (tetrahedral or octahedral)	Vermiculite	Trioctahedral	–
				Dioctahedral	–
2:1	Non-hydrated cations	x ≈ 0.5 to 1 (tetrahedral)	Mica	Trioctahedral	–
				Dioctahedral	*Muscovite, Illite*
		x ≈ 0.2 (tetrahedral)	Brittle mica	Trioctahedral	–
				Dioctahedral	–
2:1:1	Hydroxides	x variable, iron excess in the hydroxide layer	Chlorite	Trioctahedral	Chamosite
		x variable, iron excess in the hydroxide layer		Dioctahedral	–

Table I.3 summarizes the AIPEA classification of phyllosilicates based on layer structure (1:1, 2:1, 2:1:1), interlayer composition, and layer charge. Mineral groups such as serpentine-kaolinite, talc-pyrophyllite, smectite, vermiculite, mica, brittle mica, and chlorite are further divided into dioctahedral or trioctahedral subgroups. Representative species, with soil-occurring types underlined, illustrate the diversity of structural and compositional variations influencing physicochemical properties and environmental behaviour.

6.1.4. Role of clays as supports in photocatalysis:

Clays have emerged as versatile and cost-effective supports for photocatalysts due to their layered structure, high specific surface area, tunable porosity, and inherent ion-exchange capacity. These characteristics facilitate the uniform dispersion of semiconductor nanoparticles, such as TiO_2, and reduce agglomeration, thereby increasing the number of active sites available for photocatalytic reactions [94]. Furthermore, clays can enhance the adsorption of target pollutants, promoting a synergistic "adsorption–photodegradation" mechanism that improves degradation efficiency. Their structural stability under irradiation and in aqueous media also contributes to catalytic reusability [105]. Recent studies have demonstrated that clay-TiO_2 composites exhibit superior photocatalytic performance compared to bare TiO_2, particularly in the degradation of dyes and emerging contaminants. For example, Laysandra et *al.* reported that TiO_2 immobilized on bentonite significantly enhanced Rhodamine B and methylene blue degradation under UV-Vis light, attributing the improvement to increased surface hydroxyl groups and efficient charge separation [96].

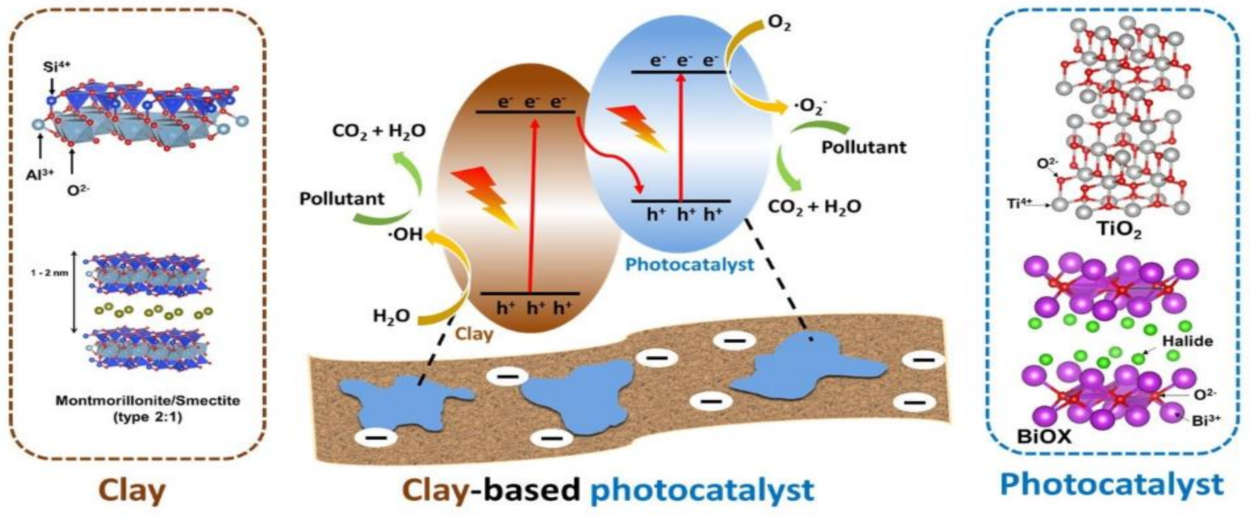

Figure I.7. Schematic representation of clay-based photocatalysts and their mechanism for organic pollutant degradation [115].

Similarly, clay-supported photocatalysts have been applied for the removal of pharmaceutical residues and heavy metals, highlighting their adaptability across environmental remediation contexts [116]. This dual function, serving both as an adsorbent and as a stable support matrix, positions clays as strategic materials for developing high-performance, sustainable photocatalytic systems. Figure I.6 illustrates the structure and functional mechanism of clay-based photocatalysts for the degradation of organic pollutants, highlighting the synergistic interactions between the clay support and the semiconductor phase. The montmorillonite (2:1) layered silicate provides a high specific surface area, interlayer space, and exchangeable cations, enabling efficient adsorption of pollutants and uniform dispersion of photocatalytic nanoparticles such as TiO_2 and BiOX. Upon photoexcitation, these semiconductors generate electron-hole pairs, which then participate in redox reactions with surface-adsorbed water and oxygen to produce reactive oxygen species ($^{\bullet}OH$, $O_2^{\bullet-}$). These radicals initiate oxidative degradation of organic contaminants, ultimately yielding CO_2 and H_2O [115]. The incorporation of clay not only enhances the adsorption capacity and pollutant pre-concentration near active sites but also improves charge carrier separation and prevents photocatalyst agglomeration, thereby substantially increasing the overall photocatalytic efficiency through a combined adsorption-photodegradation mechanism [117].

6.2. Bentonite:

6.2.1. Structural characteristics and surface properties of bentonite:

Bentonite is a natural smectite clay predominantly composed of montmorillonite, a 2:1 layered phyllosilicate in which an octahedral alumina sheet is sandwiched between two tetrahedral silica sheets [115,118]. Isomorphic substitutions within these layers, commonly Mg^{2+} for Al^{3+} in the octahedral sheet or Al^{3+} for Si^{4+} in the tetrahedral sheet, generate a permanent negative layer charge, balanced by exchangeable cations (Na^+, Ca^{2+}, K^+) in the interlayer spaces. This structural arrangement endows bentonite with a high cation-exchange capacity (CEC), a significant specific surface area, and swelling capacity, enabling the intercalation of organic or inorganic species and the effective dispersion of nanoparticles [119]. The surface chemistry is dominated by silanol (Si-OH) and aluminol (Al-OH) groups, which can act as reactive sites for adsorption, ion exchange, or chemical modification, enhancing compatibility with photocatalytic oxides such as TiO_2. Furthermore, the combination of micro and mesoporosity facilitates mass transfer and pollutant adsorption, while the layered morphology contributes to mechanical stability in composite photocatalysts [34], [111].

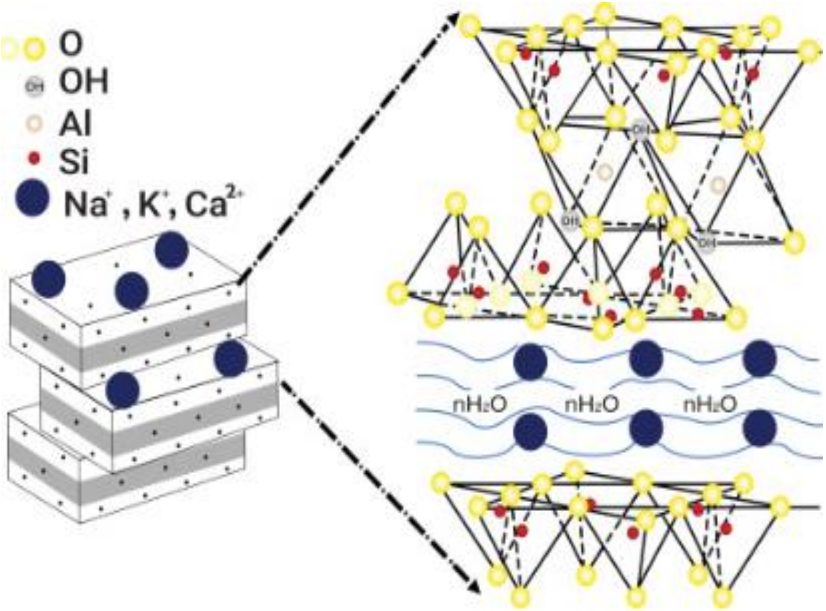

Figure I.8. Structure of bentonite clay [120].

6.2.2. Adsorption and ion-exchange mechanisms of bentonite in the photocatalytic process:

The adsorption and ion-exchange properties of clay minerals, particularly bentonite, are essential for enhancing photocatalytic processes by promoting pollutant pre-concentration and regulating surface charge. The layered structure of bentonite, primarily consisting of negatively charged aluminosilicate sheets, facilitates cation exchange through its interlayer spaces, thereby effectively sequestering dye molecules and metal ions from aqueous solutions [121].

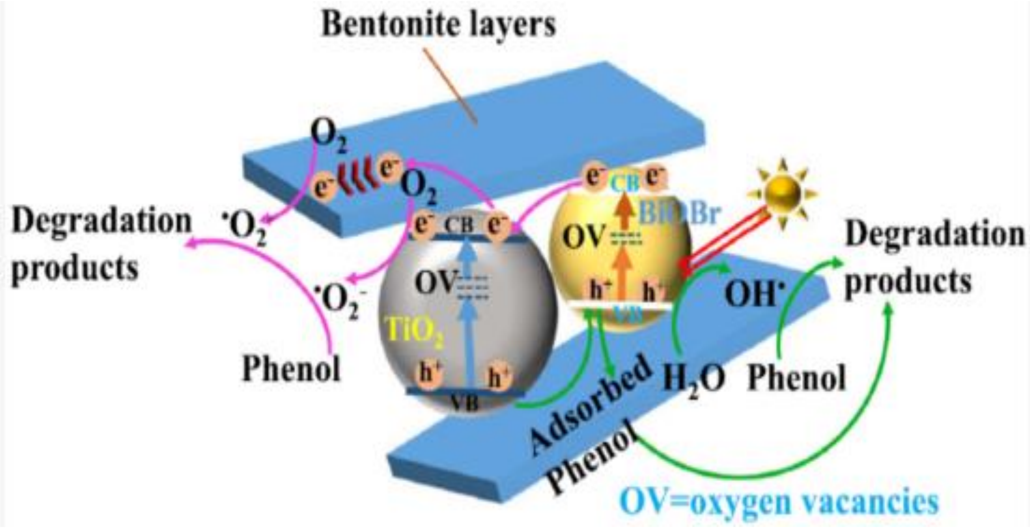

Figure I.9. Charge transfer mechanism for the degradation of phenol on TiO_2-BiOBr-bentonite ternary heterostructures [115].

This pre-adsorption enhances photocatalytic degradation by increasing the local pollutant concentration at the surface of the semiconductor, thereby improving charge transfer and the formation of reactive oxygen species [116,121]. Additionally, ion-exchange sites in bentonite can hold metal cations or semiconductor nanoparticles, stabilising them against aggregation and boosting interfacial electron transport [122]. For example, when integrated into hybrid photocatalysts like TiO_2-BiOBr-bentonite ternary heterostructures, these properties work together to improve light absorption, extend charge carrier lifetimes, and reduce electron-hole recombination through effective interfacial charge separation. This cooperative effect is schematically shown in Figure I.9. [115,119]. Recent research demonstrates that such clay-based composites have superior photocatalytic efficiency in the degradation of organic compounds due to the combined adsorption-photocatalysis process [113,122, 123].

7. TiO_2-Bentonite composites:

7.1. Techniques of synthesis:

The synthesis of TiO_2-bentonite composites has been widely investigated as a strategy to improve photocatalytic efficiency by harnessing the synergistic interaction between titanium dioxide and the high surface area, adsorption capacity, and ion-exchange properties of bentonite. A wide range of preparation methods has been reported, each conferring specific physicochemical attributes that critically determine the structural organization, surface properties, and catalytic performance of the resulting composites. Among these, the sol-gel method remains one of the most widely employed due to its ability to produce homogeneous dispersions of TiO_2 nanoparticles on bentonite surfaces, precise control over particle size, and tunable crystallinity through calcination [92], [124]. In this process, titanium precursors such as titanium isopropoxide (TTIP) undergo hydrolysis and condensation in the presence of dispersed bentonite, followed by drying and thermal treatment to achieve the desired anatase or mixed-phase composition [125]. Alternative methods include hydrothermal synthesis, which promotes strong interfacial bonding between TiO_2 and bentonite layers through crystallization under high-temperature and high-pressure aqueous conditions, resulting in enhanced structural stability and improved charge separation efficiency [126]. Impregnation and precipitation techniques are also frequently utilized, offering simplicity and scalability; however, these methods often yield less uniform TiO_2 distribution compared to sol-gel and hydrothermal approaches [118,127]. More recently, ultrasound-assisted and microwave-assisted syntheses have gained attention for their ability to accelerate reaction kinetics, improve TiO_2 dispersion within bentonite matrices, and reduce energy consumption [128]. The choice of synthesis technique directly impacts textural properties, surface chemistry, and ultimately the photocatalytic degradation efficiency toward refractory organic pollutants.

7.1.1. Synthesis of TiO_2-Bentonite composites using sol-gel method:

The sol-gel method is a widely employed and versatile approach for synthesizing TiO_2-bentonite composites, distinguished by its capacity to yield high-purity materials with uniform dispersion of active phases and controllable physicochemical properties. This method involves the hydrolysis and condensation of metal alkoxides or inorganic precursors under controlled conditions, enabling the formation of a colloidal sol that gradually evolves into a gel network. Incorporating bentonite into the sol-gel matrix enhances the surface area, adsorption capacity, and stability of the resulting photocatalyst, while also improving the dispersion of TiO_2 nanoparticles and reducing agglomeration. The layered silicate structure and high cation-exchange capacity of bentonite provide favourable sites for the immobilization of TiO_2, which in turn facilitates charge separation and enhances photocatalytic efficiency. Various synthesis parameters, including precursor type, pH, calcination temperature, and TiO_2 loading, significantly influence the structural, textural, and optical properties of the composite material [125,127,129]. Rapsomanikis et al. synthesized TiO_2-halloysite clay composites via the sol-gel method for the photocatalytic degradation of BB41. A distinctive aspect of this photocatalyst was the surface modification with silver particles, achieved by immersing the composite films in a 1.0 mM $AgNO_3$ solution for 10-20 minutes, followed by rinsing with double-distilled water and drying under nitrogen. Subsequent UV irradiation facilitated the reduction of Ag^+ to metallic Ag^0. The presence of these Ag nanoparticles was shown to enhance charge carrier separation in TiO_2, thereby improving its photocatalytic performance [130]. Incorporation of Ag nanoparticles, such as in Ag-AgCl-doped TiO_2-palygorskite, enhances visible-light responsiveness and significantly improves photocatalytic performance for Rhodamine B degradation [131]. In addition, the spectral response of TiO_2 can be extended by coupling with metal oxides such as Fe_2O_3, which exhibits strong visible-light photoactivity via Fenton-type processes. When incorporated into bentonite-supported TiO_2 through a sol-gel method, Fe_2O_3 significantly enhanced the photocatalytic degradation of methylene blue, achieving complete degradation within 2 hours. Beyond improving visible-light absorption, the magnetic properties of Fe_2O_3 also enabled facile recovery and reuse of the catalyst, enhancing its practical applicability [132]. Table I.4 provides a concise overview of the synthesis strategies and applications of various titania-clay composites in dye degradation through photocatalysis. A comparative analysis by Asma Raza et al [94] indicates that the sol-gel approach is the most widely employed method for fabricating titania-clay composites, relative to other reported techniques.

Table I.4. Summary of the synthesis of TiO_2-Bentonite composites and photocatalytic operational conditions reported in recent literature.

Catalyst composites	Method	Pollutants	Operating conditions	R (%)	Ref
TiO_2- Bentonite composites	Sol gel	methyl orange	$[MeO]_0$=10 mg/L pH 3 and 10 Lamp (UV-LRGP)	100	[133]
TiO_2- Bentonite composites	Sol-gel-assisted microwave	methylene blue	Amount of catalyst (10 mg) UV lamp (64 W)	98	[134]
TiO_2- Bentonite composites	Sol-gel	crude oil	150W UV (λ= 240-580 nm) $20mWcm^{-2}$	52	[135]
Cu/TiO_2/bentonite	Thermal decomposition	Deltamethrin	pH 12, natural sunlight	97.48	[113]
TiO_2/Bentonite/ZnO	Sol gel	methyl orange	pH=5, $[MeO]_0$=20 ppm, Amount of catalyst (4 g/L)	95	[136]
TiO_2- Bentonite composites	impregnation	methylene blue	Amount of catalyst (5 mg), $[MeB]_0$=50 ppm, 10-watt UV lamp	99.91	[137]
Bentonite/TiO_2/Ag	Sol gel	Direct red 80	Amount of catalyst (0.03 g), 10mg/L, UV lamp	77	[138]

7.1.2. Role of bentonite loading:

Bentonite incorporation influences the structural and photocatalytic performance of TiO_2-bentonite composites by controlling surface area, porosity, and light-harvesting capacity[139]. Optimal bentonite content facilitates uniform nanoparticle dispersion, prevents TiO_2 agglomeration, and provides an abundance of active sites for adsorption-photodegradation processes [118]. However, excessive bentonite content can dilute the active TiO_2 phase, reducing light absorption and limiting electron-hole pair generation. In contrast, insufficient bentonite may result in particle aggregation and lower pollutant adsorption capacity [140]. For

TiO_2/ clinoptilolite prepared by the sol-gel method, a 90/10 ratio demonstrated the highest activity, as lower clay content increased surface area, enhanced degradation of cyanide and MV-2B dye, and aided catalyst recovery by preventing TiO_2 agglomeration [94]. Recent investigations indicate that optimized bentonite/TiO_2 ratios, typically within the range of 20-50 wt%, can significantly enhance photocatalytic efficiency; for example, composites containing ~20 % TiO_2 on bentonite achieved up to 99.94 % methylene blue removal under UV irradiation, the findings highlight that an optimised bentonite loading balances surface area, adsorption capacity, and active site availability, thereby improving charge separation and minimising electron-hole recombination, which are crucial for effective photocatalysis in environmental remediation [118].

8. Conclusion

This chapter has established the theoretical foundation of the present study, beginning with a comprehensive examination of refractory organic pollutants (ROPs), their physicochemical attributes, persistence within environmental matrices, and the consequent ecological and human health risks. Emphasis was accorded to Rhodamine B, chosen as a model compound because of its extensive application, pronounced chemical stability, and resistance to conventional treatment processes. A critical review of advanced oxidation processes (AOPs) highlighted heterogeneous semiconductor photocatalysis as a particularly promising route for the degradation of such pollutants, offering the potential for complete degradation under appropriate operational conditions. Within this context, the sol-gel method was presented as a versatile and controllable synthesis route for nanostructured photocatalysts, enabling precise modulation of textural, morphological, and optical properties. Titanium dioxide (TiO_2), as the most extensively studied photocatalyst, was discussed in terms of its crystalline phases, key operational parameters, and inherent limitations, including electron-hole recombination and restricted visible-light activity. The incorporation of clay minerals, notably bentonite, was identified as an effective strategy to enhance photocatalytic performance by improving TiO_2 dispersion, increasing surface area, and augmenting pollutant adsorption capacity. The synthesis and optimization of TiO_2-bentonite composites via the sol-gel method, along with an evaluation of bentonite loading effects, emerged as a critical research direction to overcome existing performance limitations. These considerations provide the conceptual foundation and scientific rationale for the experimental investigations detailed in the subsequent chapters

References:

[1] M. Luan, “Treatment of refractory organic pollutants in industrial wastewater by wet air oxidation”.

[2] H. K. Morker and B. Saini, “A study of advanced oxidation processes for the removal of refractory pollutants from pharmaceutical wastewater,” in *Development in Wastewater Treatment Research and Processes*, Elsevier, 2024, pp. 271–287. doi: 10.1016/B978-0-323-99278-7.00006-7.

[3] M. Srivastav, M. Gupta, S. K. Agrahari, and P. Detwal, “Removal of Refractory Organic Compounds from Wastewater by Various Advanced Oxidation Process - A Review,” *CEE*, vol. 6, no. 1, pp. 8–16, Mar. 2019, doi: 10.2174/2212717806666181212125216.

[4] E. O. Alegbe and T. O. Uthman, “A review of history, properties, classification, applications and challenges of natural and synthetic dyes,” *Heliyon*, vol. 10, no. 13, p. e33646, Jul. 2024, doi: 10.1016/j.heliyon.2024.e33646.

[5] S. K. Srivastava, “Recent advances in removal of pharmaceutical pollutants in wastewater using metal oxides and carbonaceous materials as photocatalysts: a review,” *RSC Appl. Interfaces*, vol. 1, no. 3, pp. 340–429, 2024, doi: 10.1039/D3LF00142C.

[6] T. Zhang, X. Huang, J. Qiao, Y. Liu, J. Zhang, and Y. Wang, “Recent developments in synthesis of attapulgite composite materials for refractory organic wastewater treatment: a review,” *RSC Adv.*, vol. 14, no. 23, pp. 16300–16317, 2024, doi: 10.1039/D4RA02014F.

[7] C. Zhao *et al.*, “Study on the degradation performance of coking wastewater using an in-situ enhanced Fe2+/Fe3+ cycle dual-cathode Electro-Fenton system,” *Journal of Environmental Chemical Engineering*, vol. 12, no. 6, p. 114591, Dec. 2024, doi: 10.1016/j.jece.2024.114591.

[8] B. Belete, B. Desye, A. Ambelu, and C. Yenew, “Micropollutant Removal Efficiency of Advanced Wastewater Treatment Plants: A Systematic Review,” *Environ Health Insights*, vol. 17, p. 11786302231195158, Jan. 2023, doi: 10.1177/11786302231195158.

[9] A. K. Singh, “Recent advancement in bioremediation of pharmaceutical wastewater,” in *Development in Wastewater Treatment Research and Processes*, Elsevier, 2024, pp. 51–70. doi: 10.1016/B978-0-323-99278-7.00003-1.

[10] Y. Liu, S. Cong, H. Yu, D. Zou, and Y. Gao, “Microplastics Remediation in the Aqueous Environment,” in *Microplastic Occurrence, Fate, Impact, and Remediation*, vol. 73, C. Wang, S. Babel, and E. Lichtfouse, Eds., in Environmental Chemistry for a Sustainable World, vol. 73. , Cham: Springer Nature Switzerland, 2023, pp. 87–107. doi: 10.1007/978-3-031-36351-1_4.

[11] S. L. Alfee and M. C. Bloor, “A global review of river sediment contamination and remobilization through climate change-induced flooding,” *Sustainable Environment*, vol. 11, no. 1, p. 2440957, Dec. 2025, doi: 10.1080/27658511.2024.2440957.

[12] M. Matthies, K. Solomon, M. Vighi, A. Gilman, and J. V. Tarazona, “The origin and evolution of assessment criteria for persistent, bioaccumulative and toxic (PBT) chemicals and persistent organic pollutants (POPs),” *Environ. Sci.: Processes Impacts*, vol. 18, no. 9, pp. 1114–1128, 2016, doi: 10.1039/C6EM00311G.

[13] S. S, N. Rajamohan, S. S, A. R, and R. M, “Sustainable remediation of pesticide pollutants using covalent organic framework – A review on material properties, synthesis methods and application,” *Environmental Research*, vol. 246, p. 118018, Apr. 2024, doi: 10.1016/j.envres.2023.118018.

[14] L. O. Ajala, J. E. H. Wilson, M. Jiru, and M. O. Iwunze, “Perspective on health and ecological risk assessments of potentially toxic metal(loid)s using aquatic biodiversity as biomonitoring indicators,” *Toxicology Reports*, vol. 15, p. 102086, Dec. 2025, doi: 10.1016/j.toxrep.2025.102086.

[15] W. Wang, J.-S. Chang, K.-Y. Show, and D.-J. Lee, “Anaerobic recalcitrance in wastewater treatment: A review,” *Bioresource Technology*, vol. 363, p. 127920, Nov. 2022, doi: 10.1016/j.biortech.2022.127920.

[16] V. Katheresan, J. Kansedo, and S. Y. Lau, “Efficiency of various recent wastewater dye removal methods: A review,” *Journal of Environmental Chemical Engineering*, vol. 6, no. 4, pp. 4676–4697, Aug. 2018, doi: 10.1016/j.jece.2018.06.060.

[17] Q. Lu, W. Gao, J. Du, L. Zhou, and Y. Lian, “Discovery of Environmental Rhodamine B Contamination in Paprika during the Vegetation Process,” *J. Agric. Food Chem.*, vol. 60, no. 19, pp. 4773–4778, May 2012, doi: 10.1021/jf300067z.

[18] A. K. Al-Buriahi *et al.*, “Elimination of rhodamine B from textile wastewater using nanoparticle photocatalysts: A review for sustainable approaches,” *Chemosphere*, vol. 287, p. 132162, Jan. 2022, doi: 10.1016/j.chemosphere.2021.132162.

[19] Keerthika V R, Reshma S, John Moses, Sadhna S, and Eunice J, “Advanced Oxidation Process: Tearting Organic Pollutant,” *Int Res J Adv Engg Hub*, vol. 3, no. 03, pp. 330–338, Mar. 2025, doi: 10.47392/IRJAEH.2025.0045.

[20] M. A. Oturan and J.-J. Aaron, “Advanced Oxidation Processes in Water/Wastewater Treatment: Principles and Applications. A Review,” *Critical Reviews in Environmental Science and Technology*, vol. 44, no. 23, pp. 2577–2641, Dec. 2014, doi: 10.1080/10643389.2013.829765.

[21] G. Dong *et al.*, “Advanced oxidation processes in microreactors for water and wastewater treatment: Development, challenges, and opportunities,” *Water Research*, vol. 211, p. 118047, Mar. 2022, doi: 10.1016/j.watres.2022.118047.

[22] P. Ganesh Kumar, S. Kanmani, P. Senthil Kumar, and K. Vellingiri, “Efficacy of simultaneous advanced oxidation and adsorption for treating municipal wastewater for indirect potable reuse,” *Chemosphere*, vol. 321, p. 138115, Apr. 2023, doi: 10.1016/j.chemosphere.2023.138115.

[23] M. Sillanpää, M. C. Ncibi, and A. Matilainen, “Advanced oxidation processes for the removal of natural organic matter from drinking water sources: A comprehensive review,”

Journal of Environmental Management, vol. 208, pp. 56–76, Feb. 2018, doi: 10.1016/j.jenvman.2017.12.009.

[24] M. Noman, M. Siddique, K. S. Ali, and F. Khan, “Treatment of Industrial Wastewater (IWW) and Reuse through Advanced Oxidation Processes (AOPs): A Comprehensive Overview”.

[25] M. Umar, F. Roddick, L. Fan, and H. A. Aziz, “Application of ozone for the removal of bisphenol A from water and wastewater – A review,” *Chemosphere*, vol. 90, no. 8, pp. 2197–2207, Feb. 2013, doi: 10.1016/j.chemosphere.2012.09.090.

[26] U. Hübner *et al.*, “Advanced oxidation processes for water and wastewater treatment – Guidance for systematic future research,” *Heliyon*, vol. 10, no. 9, p. e30402, May 2024, doi: 10.1016/j.heliyon.2024.e30402.

[27] K. Całus-Makowska, J. Dziubińska, A. Grosser, and A. Grobelak, “Application of the Fenton and photo-Fenton processes in pharmaceutical removal: New perspectives in environmental protection,” *Desalination and Water Treatment*, vol. 321, p. 100949, Jan. 2025, doi: 10.1016/j.dwt.2024.100949.

[28] R. Tanveer, A. Yasar, A.-S. Nizami, and A. B. Tabinda, “Integration of physical and advanced oxidation processes for treatment and reuse of textile dye-bath effluents with minimum area footprint,” *Journal of Cleaner Production*, vol. 383, p. 135366, Jan. 2023, doi: 10.1016/j.jclepro.2022.135366.

[29] X. Liu *et al.*, “A review on percarbonate-based advanced oxidation processes for remediation of organic compounds in water,” *Environmental Research*, vol. 200, p. 111371, Sep. 2021, doi: 10.1016/j.envres.2021.111371.

[30] L. El Gaini, “Enhancing solar-driven photocatalysis: Synergistic integration of biochar, semiconductors, and magnetic materials for degrading organic pollutants,” *Desalination and Water Treatment*, vol. 320, p. 100798, Oct. 2024, doi: 10.1016/j.dwt.2024.100798.

[31] C. Hayet, “Degradation of Orange G by UV/TiO2/IO4 $^{-}$process: Effect of operational parameters and estimation of electrical energy consumption,” *Indian J Chem Technol*, 2023, doi: 10.56042/ijct.v30i3.62814.

[32] C. Liu *et al.*, “Knowledge-Driven Design and Lab-Based Evaluation of B-doped TiO_2 Photocatalysts for Ammonia Synthesis,” *Advanced Energy Materials*, vol. 13, no. 8, p. 2204126, Feb. 2023, doi: 10.1002/aenm.202204126.

[33] F. I. El-Dossoki, T. M. Atwee, A. M. Hamada, and A. A. El-Bindary, “Photocatalytic degradation of Remazol Red B and Rhodamine B dyes using TiO2 nanomaterial: estimation of the effective operating parameters,” *Desalination and Water Treatment*, vol. 233, pp. 319–330, Sep. 2021, doi: 10.5004/dwt.2021.27519.

[34] A. Setiawan, V. F. Qur’ani, T. A. Ramadani, M. L. Ashari, D. Dermawan, and A. P. Iswara, “Potential of Local Natural Bentonite Impregnated with N-TiO_2 to Degrade Methylene Blue Using Photocatalytic Process,” *Future Cities and Environment*, vol. 10, no. 1, p. 14, Jun. 2024, doi: 10.5334/fce.220.

[35] R. Krakowiak *et al.*, “TiO_2–Fe_3O_4 Composite systems-preparation, physicochemical Characterization, and an Attempt to Explain the Limitations That Arise in Catalytic Applications,” *Applied Sciences*, vol. 12, no. 17, p. 8826, Sep. 2022, doi: 10.3390/app12178826.

[36] A. Nasir, S. Khalid, T. Yasin, and A. Mazare, “A Review on the Progress and Future of TiO2/Graphene Photocatalysts,” *Energies*, vol. 15, no. 17, p. 6248, Aug. 2022, doi: 10.3390/en15176248.

[37] Z.-D. Meng, S. Sarkar, L. Zhu, K. Ullah, S. Ye, and W.-C. Oh, “Sonocatalytic Degradation of Rhodamine B in the Presence of TiO_2 Nanoparticles by Loading WO_3,” *Korean Journal of Materials Research*, vol. 24, no. 1, pp. 6–12, Jan. 2014, doi: 10.3740/MRSK.2014.24.1.6.

[38] C. Chang, S. Rad, L. Gan, Z. Li, J. Dai, and A. Shahab, “Review of the sol–gel method in preparing nano TiO_2 for advanced oxidation process,” *Nanotechnology Reviews*, vol. 12, no. 1, p. 20230150, Nov. 2023, doi: 10.1515/ntrev-2023-0150.

[39] J. Qi, G. Jiang, Y. Wan, J. Liu, and F. Pi, “Nanomaterials-modulated Fenton reactions: Strategies, chemodynamic therapy and future trends,” *Chemical Engineering Journal*, vol. 466, p. 142960, Jun. 2023, doi: 10.1016/j.cej.2023.142960.

[40] J. Cao, J. Li, B. Yang, Z. Chen, A. R. Mahjoub, and M. Xing, “Gambling of homogeneous and heterogeneous Fenton in wastewater treatment,” *Cell Reports Physical Science*, vol. 5, no. 5, p. 101966, May 2024, doi: 10.1016/j.xcrp.2024.101966.

[41] J. C. Colmenares and Y.-J. Xu, Eds., *Heterogeneous Photocatalysis*. in Green Chemistry and Sustainable Technology. Berlin, Heidelberg: Springer Berlin Heidelberg, 2016. doi: 10.1007/978-3-662-48719-8.

[42] S. J. Armaković, M. M. Savanović, and S. Armaković, “Titanium Dioxide as the Most Used Photocatalyst for Water Purification: An Overview,” *Catalysts*, vol. 13, no. 1, p. 26, Dec. 2022, doi: 10.3390/catal13010026.

[43] M. Michman, “Homogeneous vs. heterogeneous processes in electrocatalysis. Different types of catalysis in organic electrooxidation,” *Journal of Molecular Catalysis A: Chemical*, vol. 107, no. 1–3, pp. 393–398, May 1996, doi: 10.1016/1381-1169(95)00238-3.

[44] F. Poovan, V. G. Chandrashekhar, K. Natte, and R. V. Jagadeesh, “Synergy between homogeneous and heterogeneous catalysis,” *Catal. Sci. Technol.*, vol. 12, no. 22, pp. 6623–6649, 2022, doi: 10.1039/D2CY00232A.

[45] A. Kurt, “Cefuroxime oxidation with new generation anodes: Evaluation of parameter effects, kinetics and total intermediate products,” *Environmental Research and Technology*, vol. 4, no. 4, pp. 317–328, Dec. 2021, doi: 10.35208/ert.867139.

[46] K. S. Varma *et al.*, “Photocatalytic performance and interaction mechanism of reverse micelle synthesized Cu-TiO2 nanomaterials towards levofloxacin under visible LED light,” *Photochem Photobiol Sci*, vol. 21, no. 1, pp. 77–89, Jan. 2022, doi: 10.1007/s43630-021-00141-8.

[47] X. Bai *et al.*, “In-situ synthesized 2D MXene/TiO2/Fe hybrid with (001)–(101) surface heterojunction for degradation of tetracycline under visible light,” *Chemosphere*, vol. 338, p. 139546, Oct. 2023, doi: 10.1016/j.chemosphere.2023.139546.

[48] T. Z. Liza, M. M. H. Tusher, F. Anwar, M. F. Monika, K. F. Amin, and F. N. U. Asrafuzzaman, “Effect of Ag-doping on morphology, structure, band gap and photocatalytic activity of bio-mediated TiO2 nanoparticles,” *Results in Materials*, vol. 22, p. 100559, Jun. 2024, doi: 10.1016/j.rinma.2024.100559.

[49] X. Zou, J. Ke, J. Hao, X. Yan, and Y. Tian, “A new method for synthesis of ZnO flower-like nanostructures and their photocatalytic performance,” *Physica B: Condensed Matter*, vol. 624, p. 413395, Jan. 2022, doi: 10.1016/j.physb.2021.413395.

[50] X. Luo, Z. Lou, L. Wang, X. Zheng, and T. Zhang, “Fabrication of flower-like ZnO nanosheet and nanorod-assembled hierarchical structures and their enhanced performance in gas sensors,” *New J. Chem.*, vol. 38, no. 1, pp. 84–89, 2014, doi: 10.1039/C3NJ00776F.

[51] L. Zhang, X. Wu, and J. Li, “Sn-doped BiOI assisted the excellent photocatalytic performance of multi-shelled ZnO microspheres under simulated sunlight,” *Chemosphere*, vol. 290, p. 133309, Mar. 2022, doi: 10.1016/j.chemosphere.2021.133309.

[52] S. Zhang, R. Wang, X. Cheng, J. Lian, X. Liu, and J. Tang, “Degradation of Azo Dye Orange II Using BiOI/HKUST-1 Activated Persulfate under Visible Light Irradiation,” *Water*, vol. 16, no. 13, p. 1805, Jun. 2024, doi: 10.3390/w16131805.

[53] Z. U. H. Khan, S. Sabahat, N. S. Shah, H. Ajab, J. Iqbal, and F. Ullah, “Electrochemical Advanced Oxidation Processes as a feasible approach towards treatment of pesticides contaminated water and environmental sustainability: A review,” *Journal of Water Process Engineering*, vol. 70, p. 107083, Feb. 2025, doi: 10.1016/j.jwpe.2025.107083.

[54] S. G. Ullattil and P. Periyat, “Sol-Gel Synthesis of Titanium Dioxide,” in *Sol-Gel Materials for Energy, Environment and Electronic Applications*, S. C. Pillai and S. Hehir, Eds., in Advances in Sol-Gel Derived Materials and Technologies. , Cham: Springer International Publishing, 2017, pp. 271–283. doi: 10.1007/978-3-319-50144-4_9.

[55] M. Parashar, V. K. Shukla, and R. Singh, “Metal oxides nanoparticles via sol–gel method: a review on synthesis, characterization and applications,” *J Mater Sci: Mater Electron*, vol. 31, no. 5, pp. 3729–3749, Mar. 2020, doi: 10.1007/s10854-020-02994-8.

[56] S. Esposito, “‘Traditional’ Sol-Gel Chemistry as a Powerful Tool for the Preparation of Supported Metal and Metal Oxide Catalysts,” *Materials*, vol. 12, no. 4, p. 668, Feb. 2019, doi: 10.3390/ma12040668.

[57] S.-W. Kim, Y. Hou, K. Madhan, K. Senthilkumar, H.-S. Kim, and W.-J. Kim, “Sol-Gel nano TiO2 synthesis using TTIP: Latest trends, a comprehensive review of attribute optimization and various applications,” *Materials Today*, p. S136970212500207X, May 2025, doi: 10.1016/j.mattod.2025.05.009.

[58] L. P. Singh *et al.*, “Sol-Gel processing of silica nanoparticles and their applications,” *Advances in Colloid and Interface Science*, vol. 214, pp. 17–37, Dec. 2014, doi: 10.1016/j.cis.2014.10.007.

[59] "Aqueous and Nonaqueous Sol-Gel Chemistry," in *Metal Oxide Nanoparticles in Organic Solvents*, in Engineering Materials and Processes. , London: Springer London, 2009, pp. 7–18. doi: 10.1007/978-1-84882-671-7_2.

[60] S. Pandey and S. B. Mishra, "Sol–gel derived organic–inorganic hybrid materials: synthesis, characterizations and applications," *J Sol-Gel Sci Technol*, vol. 59, no. 1, pp. 73–94, Jul. 2011, doi: 10.1007/s10971-011-2465-0.

[61] A. Vinukonda, N. Bolledla, R. K. Jadi, R. Chinthala, and V. R. Devadasu, "Synthesis of nanoparticles using advanced techniques," *Next Nanotechnology*, vol. 8, p. 100169, 2025, doi: 10.1016/j.nxnano.2025.100169.

[62] S. Sopan Mahato, D. Mahata, S. Panda, and S. Mahata, "Perspective Chapter: Sol-Gel Science and Technology in Context of Nanomaterials – Recent Advances," in *Sol-Gel Method - Recent Advances*, J. Pal Singh, S. Shankar Acharya, S. Kumar, and S. Kumar Dixit, Eds., IntechOpen, 2023. doi: 10.5772/intechopen.111378.

[63] M. Borlaf and R. Moreno, "Colloidal sol-gel: A powerful low-temperature aqueous synthesis route of nanosized powders and suspensions," *Open Ceramics*, vol. 8, p. 100200, Dec. 2021, doi: 10.1016/j.oceram.2021.100200.

[64] K. Kajihara and M. Goto, "Cosolvent-free synthesis of macroporous silica gels and monolithic silica glasses from tetraalkoxysilane-water binary systems: comparison between tetramethoxysilane and tetraethoxysilane," *J Sol-Gel Sci Technol*, vol. 104, no. 3, pp. 497–502, Dec. 2022, doi: 10.1007/s10971-022-05799-9.

[65] A. Das, M. Patra, R. R. Wary, P. Gupta, and R. G. Nair, "Photocatalytic performance analysis of Degussa P25 under various laboratory conditions," *IOP Conf. Ser.: Mater. Sci. Eng.*, vol. 377, p. 012101, Jun. 2018, doi: 10.1088/1757-899X/377/1/012101.

[66] D. R. Eddy *et al.*, "Heterophase Polymorph of TiO2 (Anatase, Rutile, Brookite, TiO2 (B)) for Efficient Photocatalyst: Fabrication and Activity," *Nanomaterials*, vol. 13, no. 4, p. 704, Feb. 2023, doi: 10.3390/nano13040704.

[67] R. Nawaz *et al.*, "Photodegrading hazardous pollutants using black TiO2 materials with different morphology and estimation of energy requirement," *Materials Chemistry and Physics*, vol. 309, p. 128401, Nov. 2023, doi: 10.1016/j.matchemphys.2023.128401.

[68] J. Wang *et al.*, "Disruption Symmetric Crystal Structure Favoring Photocatalytic CO_2 Reduction: Reduced *COOH Formation Energy Barrier on Al Doped CuS/TiO_2," *Adv Funct Materials*, vol. 34, no. 42, p. 2406549, Oct. 2024, doi: 10.1002/adfm.202406549.

[69] G. Meinhold, "Rutile and its applications in earth sciences," *Earth-Science Reviews*, vol. 102, no. 1–2, pp. 1–28, Sep. 2010, doi: 10.1016/j.earscirev.2010.06.001.

[70] D. A. H. Hanaor and C. C. Sorrell, "Review of the anatase to rutile phase transformation," *J Mater Sci*, vol. 46, no. 4, pp. 855–874, Feb. 2011, doi: 10.1007/s10853-010-5113-0.

[71] F. Scarpelli, T. F. Mastropietro, T. Poerio, and N. Godbert, "Mesoporous TiO2 Thin Films: State of the Art," in *Titanium Dioxide - Material for a Sustainable Environment*, D. Yang, Ed., InTech, 2018. doi: 10.5772/intechopen.74244.

[72] M. S. Bégin-Colin *et al.*, “Modification contrôlée des propriétés cristallochimiques et physico-chimiques de matériaux nanostructurés à base de TiO2 pour la maitrise des propriétés photocatalytiques”.

[73] B. Hudec, “Structures for nanoscale DRAM memories - PhD thesis,” 2012, *Unpublished*. doi: 10.13140/2.1.4370.5288.

[74] A. H. Mamaghani, F. Haghighat, and C.-S. Lee, “Hydrothermal/solvothermal synthesis and treatment of TiO2 for photocatalytic degradation of air pollutants: Preparation, characterization, properties, and performance,” *Chemosphere*, vol. 219, pp. 804–825, Mar. 2019, doi: 10.1016/j.chemosphere.2018.12.029.

[75] A. M. Alotaibi *et al.*, “Chemical Vapor Deposition of Photocatalytically Active Pure Brookite TiO_2 Thin Films,” *Chem. Mater.*, vol. 30, no. 4, pp. 1353–1361, Feb. 2018, doi: 10.1021/acs.chemmater.7b04944.

[76] A. K. Vishwakarma and L. Yadava, “Fabrication and Characterization of Nano-TiO_2 Thin Film Using Physical Vapor Deposition Method,” *adv sci engng med*, vol. 10, no. 7, pp. 723–726, Jul. 2018, doi: 10.1166/asem.2018.2239.

[77] Z. Wang *et al.*, “Preparation and characterization of TiO2 nanoparticles by two different precipitation methods,” *Ceramics International*, vol. 46, no. 10, pp. 15333–15341, Jul. 2020, doi: 10.1016/j.ceramint.2020.03.075.

[78] E. Endarko and S. R. Adawiyah, “Experimental Study of TiO2 Nanoparticles Fabrication by Sol-gel and Co-precipitation Methods for TiO2/SnO2 Composite Thin Film as Photoanode,” *J. I. Dasar*, vol. 20, no. 1, p. 61, Jan. 2019, doi: 10.19184/jid.v20i1.9154.

[79] F. Puga, J. A. Navío, C. Jaramillo-Páez, P. Sánchez-Cid, and M. C. Hidalgo, “Microwave-assisted sol-gel synthesis of TiO2 in the presence of halogenhydric acids. Characterization and photocatalytic activity,” *Journal of Photochemistry and Photobiology A: Chemistry*, vol. 394, p. 112457, May 2020, doi: 10.1016/j.jphotochem.2020.112457.

[80] N. Shakeel, I. Piwoński, P. Iqbal, and A. Kisielewska, “Green Synthesis of Titanium Dioxide Nanoparticles: Physicochemical Characterization and Applications: A Review,” *IJMS*, vol. 26, no. 12, p. 5454, Jun. 2025, doi: 10.3390/ijms26125454.

[81] D. Navas, S. Fuentes, A. Castro-Alvarez, and E. Chavez-Angel, “Review on Sol-Gel Synthesis of Perovskite and Oxide Nanomaterials,” *Gels*, vol. 7, no. 4, p. 275, Dec. 2021, doi: 10.3390/gels7040275.

[82] L. Forni *et al.*, “Non-conventional sol–gel synthesis for the production of boron-alumina catalyst applied to the vapour phase Beckmann rearrangement,” *Applied Catalysis A: General*, vol. 248, no. 1–2, pp. 47–57, Aug. 2003, doi: 10.1016/S0926-860X(03)00147-9.

[83] Y. V. Divyasri *et al.*, “Nanostructures in Photocatalysis: Opportunities and Challenges for Environmental Applications,” in *Nanostructured Materials for Environmental Applications*, S. Balakumar, V. Keller, and M. V. Shankar, Eds., Cham: Springer International Publishing, 2021, pp. 1–32. doi: 10.1007/978-3-030-72076-6_1.

[84] V. T. Lukong, K. O. Ukoba, and T. C. Jen, “Heat-assisted sol–gel synthesis of tio2 nanoparticles structural, morphological and optical analysis for self-cleaning application,”

Journal of King Saud University - Science, vol. 34, no. 1, p. 101746, Jan. 2022, doi: 10.1016/j.jksus.2021.101746.

[85] Y. N. Rajeev, C. M. Magdalane, G. Ramalingam, L. B. Kumar, N. Alwadai, and M. S. Al-Buriahi, "Photocatalytic activity of hierarchical CTAB-assisted TiO2 nanoparticles for polluted water treatment using solar light illumination," *Appl. Phys. A*, vol. 128, no. 4, p. 299, Apr. 2022, doi: 10.1007/s00339-022-05406-2.

[86] H. Y. Lin, J. L. Li, and C. C. Wang, "Study on Preparation of TiO_2 Nanoparticle by Sol-Gel Method," *AMR*, vol. 599, pp. 44–47, Nov. 2012, doi: 10.4028/www.scientific.net/AMR.599.44.

[87] G. Neri, "Non-Conventional Sol–Gel Routes to Nanosized Metal Oxides for Gas Sensing: From Materials to Applications," *sci adv mater*, vol. 2, no. 1, pp. 3–15, Mar. 2010, doi: 10.1166/sam.2010.1062.

[88] M. G. Kim *et al.*, "Effects of Calcination Temperature on the Phase Composition, Photocatalytic Degradation, and Virucidal Activities of TiO_2 Nanoparticles," *ACS Omega*, vol. 6, no. 16, pp. 10668–10678, Apr. 2021, doi: 10.1021/acsomega.1c00043.

[89] A. Saidani *et al.*, "Effect of Calcination Temperature on the Photocatalytic Activity of Precipitated ZnO Nanoparticles for the Degradation of Rhodamine B Under Different Light Sources," *Water*, vol. 17, no. 1, p. 32, Dec. 2024, doi: 10.3390/w17010032.

[90] F. He, F. Ma, J. Li, T. Li, and G. Li, "Effect of calcination temperature on the structural properties and photocatalytic activities of solvothermal synthesized TiO2 hollow nanoparticles," *Ceramics International*, vol. 40, no. 5, pp. 6441–6446, Jun. 2014, doi: 10.1016/j.ceramint.2013.11.094.

[91] T. Ishigaki *et al.*, "Enhanced visible-light photocatalytic activity of anatase-rutile mixed-phase nano-size powder given by high-temperature heat treatment," *R. Soc. open sci.*, vol. 7, no. 1, p. 191539, Jan. 2020, doi: 10.1098/rsos.191539.

[92] W. Alahmad, F. Hedhili, S. M. Al-Shomar, H. S. Albaqawi, N. A. Al-Shammari, and S. Abdelrahman, "Modeling sustainable photocatalytic degradation of acidic dyes using Jordanian nano-Kaolin–TiO2 and solar energy: Synergetic mechanistic insights," *Heliyon*, vol. 10, no. 17, p. e36978, Sep. 2024, doi: 10.1016/j.heliyon.2024.e36978.

[93] M. Paiu, D. Lutic, L. Favier, and M. Gavrilescu, "Heterogeneous Photocatalysis for Advanced Water Treatment: Materials, Mechanisms, Reactor Configurations, and Emerging Applications," *Applied Sciences*, vol. 15, no. 10, p. 5681, May 2025, doi: 10.3390/app15105681.

[94] A. Raza, R. Rehman, and M. Batool, "Recent Review of Titania-Clay-Based Composites Emerging as Advanced Adsorbents and Photocatalysts for Degradation of Dyes over the Last Decade," *Adsorption Science & Technology*, vol. 2022, p. 3823008, Jan. 2022, doi: 10.1155/2022/3823008.

[95] N. M. Chauke, R. L. Mohlala, S. Ngqoloda, and M. C. Raphulu, "Harnessing visible light: enhancing TiO2 photocatalysis with photosensitizers for sustainable and efficient environmental solutions," *Front. Chem. Eng.*, vol. 6, p. 1356021, Feb. 2024, doi: 10.3389/fceng.2024.1356021.

[96] L. Laysandra *et al.*, “Adsorption and photocatalytic performance of bentonite-titanium dioxide composites for methylene blue and rhodamine B decoloration,” *Heliyon*, vol. 3, no. 12, p. e00488, Dec. 2017, doi: 10.1016/j.heliyon.2017.e00488.

[97] S. H. Paiman, S. F. Md Noor, N. Ngadi, A. H. Nordin, and N. Abdullah, “Insight into photocatalysis technology as a promising approach to tackle microplastics pollution through degradation and upcycling,” *Chemical Engineering Journal*, vol. 467, p. 143534, Jul. 2023, doi: 10.1016/j.cej.2023.143534.

[98] F. Amano, A. Yamamoto, and J. Kumagai, “Highly Active Rutile TiO2 for Photocatalysis under Violet Light Irradiation at 405 nm,” *Catalysts*, vol. 12, no. 10, p. 1079, Sep. 2022, doi: 10.3390/catal12101079.

[99] A. J. Jadhav, A. D. Goswami, D. H. Trivedi, P. V. Chavan, N. L. Jadhav, and D. V. Pinjari, “A comprehensive review on pure and doped titanium oxide nanoparticles for photocatalytic applications,” *Inorganic Chemistry Communications*, vol. 181, p. 115206, Nov. 2025, doi: 10.1016/j.inoche.2025.115206.

[100] V. Etacheri, C. Di Valentin, J. Schneider, D. Bahnemann, and S. C. Pillai, “Visible-light activation of TiO2 photocatalysts: Advances in theory and experiments,” *Journal of Photochemistry and Photobiology C: Photochemistry Reviews*, vol. 25, pp. 1–29, Dec. 2015, doi: 10.1016/j.jphotochemrev.2015.08.003.

[101] R. Ameta, M. S. Solanki, S. Benjamin, and S. C. Ameta, “Photocatalysis,” in *Advanced Oxidation Processes for Waste Water Treatment*, Elsevier, 2018, pp. 135–175. doi: 10.1016/B978-0-12-810499-6.00006-1.

[102] B. Tang, H. Chen, H. Peng, Z. Wang, and W. Huang, “Graphene Modified TiO2 Composite Photocatalysts: Mechanism, Progress and Perspective,” *Nanomaterials*, vol. 8, no. 2, p. 105, Feb. 2018, doi: 10.3390/nano8020105.

[103] H. Sudrajat and M. Nobatova, “Heterojunction photocatalysts: where are they headed?,” *RSC Appl. Interfaces*, vol. 2, no. 3, pp. 599–619, 2025, doi: 10.1039/D5LF00037H.

[104] J. Chen, F. Qiu, W. Xu, S. Cao, and H. Zhu, “Recent progress in enhancing photocatalytic efficiency of TiO 2 -based materials,” *Applied Catalysis A: General*, vol. 495, pp. 131–140, Apr. 2015, doi: 10.1016/j.apcata.2015.02.013.

[105] K. Sahel *et al.*, “Photocatalytic degradation of anionic and cationic dyes over TiO2 P25, and Ti-pillared clays and Ag-doped Ti-pillared clays,” *Applied Clay Science*, vol. 95, pp. 205–210, Jun. 2014, doi: 10.1016/j.clay.2014.04.014.

[106] D. Ewis, M. M. Ba-Abbad, A. Benamor, and M. H. El-Naas, “Adsorption of organic water pollutants by clays and clay minerals composites: A comprehensive review,” *Applied Clay Science*, vol. 229, p. 106686, Nov. 2022, doi: 10.1016/j.clay.2022.106686.

[107] A. Mei *et al.*, “Photocatalytic materials modified with carbon quantum dots for the degradation of organic pollutants under visible light: A review,” *Environmental Research*, vol. 214, p. 114160, Nov. 2022, doi: 10.1016/j.envres.2022.114160.

[108] A. Ochirkhuyag and J. Temuujin, “The Catalytic Potential of Modified Clays: A Review,” *Minerals*, vol. 14, no. 6, p. 629, Jun. 2024, doi: 10.3390/min14060629.

[109] W. Freitas *et al.*, “The Role of Clay Mineral-Derived Photocatalysts in Insights of Remediation,” *Ceramics*, vol. 5, no. 4, pp. 862–882, Oct. 2022, doi: 10.3390/ceramics5040063.

[110] W. Bleam, “Clay Mineralogy and Chemistry,” in *Soil and Environmental Chemistry*, Elsevier, 2017, pp. 87–146. doi: 10.1016/B978-0-12-804178-9.00003-3.

[111] N. Kumari and C. Mohan, “Basics of Clay Minerals and Their Characteristic Properties,” in *Clay and Clay Minerals*, G. Morari Do Nascimento, Ed., IntechOpen, 2021. doi: 10.5772/intechopen.97672.

[112] A. Jamil, O. P. Ching, and A. M. Shariff, “Mixed matrix hollow fibre membrane comprising polyetherimide and modified montmorillonite with improved filler dispersion and CO 2 /CH 4 separation performance,” *Applied Clay Science*, vol. 143, pp. 115–124, Jul. 2017, doi: 10.1016/j.clay.2017.03.017.

[113] M. B. De Farias, M. P. Spaolonzi, T. L. Da Silva, M. G. C. Da Silva, and M. G. A. Vieira, “Natural and synthetic clay-based materials applied for the removal of emerging pollutants from aqueous medium,” in *Advanced Materials for Sustainable Environmental Remediation*, Elsevier, 2022, pp. 359–392. doi: 10.1016/B978-0-323-90485-8.00012-6.

[114] Q. Wang, C. Zhu, J. Yun, and G. Yang, “Isomorphic Substitutions in Clay Materials and Adsorption of Metal Ions onto External Surfaces: A DFT Investigation,” *J. Phys. Chem. C*, vol. 121, no. 48, pp. 26722–26732, Dec. 2017, doi: 10.1021/acs.jpcc.7b03488.

[115] C. Chuaicham *et al.*, “Recent Clay-Based Photocatalysts for Wastewater Treatment,” *Separations*, vol. 10, no. 2, p. 77, Jan. 2023, doi: 10.3390/separations10020077.

[116] Y. Qi *et al.*, “A Critical Review of Clay Mineral-Based Photocatalysts for Wastewater Treatment,” *Catalysts*, vol. 14, no. 9, p. 575, Aug. 2024, doi: 10.3390/catal14090575.

[117] D. Kim *et al.*, “Synthesis and Characterization of Montmorillonite-Supported Tio_2 Composites for Enhanced UV Absorption,” *Clays and clay miner.*, vol. 68, no. 6, pp. 533–543, Dec. 2020, doi: 10.1007/s42860-020-00094-6.

[118] L. Laysandra *et al.*, “Adsorption and photocatalytic performance of bentonite-titanium dioxide composites for methylene blue and rhodamine B decoloration,” *Heliyon*, vol. 3, no. 12, p. e00488, Dec. 2017, doi: 10.1016/j.heliyon.2017.e00488.

[119] M. Lamrani, M. Mouchane, H. Taybi, and A. Mouadili, “Comprehensive Review on the Adsorption Properties of Clay Minerals for Enhanced Removal of Toxic Dyes and Heavy Metals,” *J Water Environ Nanotechnol*, vol. 10, no. 1, Feb. 2025, doi: 10.22090/jwent.2025.01.08.

[120] J. M. Huggett, “SEDIMENTARY ROCKS | Clays and Their Diagenesis,” in *Encyclopedia of Geology*, Elsevier, 2005, pp. 62–70. doi: 10.1016/B0-12-369396-9/00311-7.

[121] D. Gandhi, R. Bandyopadhyay, and B. Soni, “Naturally occurring bentonite clay: Structural augmentation, characterization and application as catalyst,” *Materials Today: Proceedings*, vol. 57, pp. 194–201, 2022, doi: 10.1016/j.matpr.2022.02.346.

[122] T. Shahwan, Ç. Üzüm, A. E. Eroğlu, and I. Lieberwirth, “Synthesis and characterization of bentonite/iron nanoparticles and their application as adsorbent of cobalt ions,” *Applied Clay Science*, vol. 47, no. 3–4, pp. 257–262, Feb. 2010, doi: 10.1016/j.clay.2009.10.019.

[123] J. Chanani, F. Buazar, and Y. Nikpour, “Promoted Photocatalytic Activity of Green Titanium Oxide-Clay Nanocomposite Toward Polychlorinated Biphenyl Degradation in Actual Samples,” *Water Air Soil Pollut*, vol. 234, no. 6, p. 364, Jun. 2023, doi: 10.1007/s11270-023-06356-y.

[124] A. Sayqal *et al.*, “Breakdown cost and recycling processes of Bentonite/TiO2 quantum dots of photo and solar degradation of Congo Red dye and industrial dyes wastes,” *Optical Materials*, vol. 157, p. 116408, Nov. 2024, doi: 10.1016/j.optmat.2024.116408.

[125] N. Saelim, R. Magaraphan, and T. Sreethawong, “Preparation of sol–gel TiO2/purified Na-bentonite composites and their photovoltaic application for natural dye-sensitized solar cells,” *Energy Conversion and Management*, vol. 52, no. 8–9, pp. 2815–2818, Aug. 2011, doi: 10.1016/j.enconman.2011.02.016.

[126] C. Yang, Y. Zhu, J. Wang, Z. Li, X. Su, and C. Niu, “Hydrothermal synthesis of TiO2–WO3–bentonite composites: Conventional versus ultrasonic pretreatments and their adsorption of methylene blue,” *Applied Clay Science*, vol. 105–106, pp. 243–251, Mar. 2015, doi: 10.1016/j.clay.2015.01.002.

[127] M. Sirait, N. Bukit, and N. Siregar, “Preparation and characterization of natural bentonite in to nanoparticles by co-precipitation method,” presented at the THE 6TH INTERNATIONAL CONFERENCE ON THEORETICAL AND APPLIED PHYSICS (THE 6th ICTAP), Makassar, Indonesia, 2017, p. 020006. doi: 10.1063/1.4973084.

[128] F. Rastgar, S. Allahyari, and N. Rahemi, “Ultrasound-assisted adsorptive desulfurization of model fuel using plasma-surface modified- Na.bentonite,” *Process Safety and Environmental Protection*, vol. 198, p. 107206, Jun. 2025, doi: 10.1016/j.psep.2025.107206.

[129] F. Kooli, Y. Liu, R. Al-Faze, and A. Al Suhaimi, “Effect of acid activation of Saudi local clay mineral on removal properties of basic blue 41 from an aqueous solution,” *Applied Clay Science*, vol. 116–117, pp. 23–30, Nov. 2015, doi: 10.1016/j.clay.2015.07.044.

[130] “Nanocrystalline TiO2 and Halloysite clay mineral composite films prepared by sol-gel method: Synergistic effect and the case of silver modification to the photocatalytic degradation of Basic Blue- 41 azo dye in water.,” *Global NEST Journal*, vol. 16, no. 3, pp. 485–498, Mar. 2014, doi: 10.30955/gnj.001323.

[131] H. Yang, B. Yang, W. Chen, and J. Yang, “Preparation and Photocatalytic Activities of TiO2-Based Composite Catalysts,” *Catalysts*, vol. 12, no. 10, p. 1263, Oct. 2022, doi: 10.3390/catal12101263.

[132] O. A. Zelekew, D.-H. Kuo, J. M. Yassin, K. E. Ahmed, and H. Abdullah, “Synthesis of efficient silica supported TiO2/Ag2O heterostructured catalyst with enhanced photocatalytic performance,” *Applied Surface Science*, vol. 410, pp. 454–463, Jul. 2017, doi: 10.1016/j.apsusc.2017.03.089.

[133] M. Kassir *et al.*, “Adsorption and photocatalysis activity of TiO2/bentonite composites,” *Desalination and Water Treatment*, vol. 98, pp. 196–215, Dec. 2017, doi: 10.5004/dwt.. 2017.21578.

[134] A. Mishra, M. Sharma, A. Mehta, and S. Basu, “Microwave Treated Bentonite Clay Based TiO_2 Composites: An Efficient Photocatalyst for Rapid Degradation of Methylene Blue,”

J Nanosci Nanotechnol, vol. 17, no. 2, pp. 1149–1155, Feb. 2017, doi: 10.1166/jnn.. 2017.12674.

[135] T. Pernyeszi and I. Dékány, "Photocatalytic degradation of hydrocarbons by bentonite and TiO2 in aqueous suspensions containing surfactants," *Colloids and Surfaces A: Physicochemical and Engineering Aspects*, vol. 230, no. 1–3, pp. 191–199, Dec. 2003, doi: 10.1016/j.colsurfa.2003.09.023.

[136] J. Tian, J. Wang, J. Dai, X. Wang, and Y. Yin, "N-doped TiO2/ZnO composite powder and its photocatalytic performance for degradation of methyl orange," *Surface and Coatings Technology*, vol. 204, no. 5, pp. 723–730, Dec. 2009, doi: 10.1016/j.surfcoat.2009.09.028.

[137] Department of Chemistry, Faculty of Mathematics and Natural Sciences, Sriwijaya University, Jalan Palembang Prabumulih Km 32 Indralaya, Ogan Ilir, Indonesia, 30662, M. Said, N. Erlangga, D. Alfarado, S. Suheryanto, and E. Nurnawati, "Adsorption and Photocatalytic Activity of Bentonite–Titanium Dioxide on The Degradation of Methylene Blue Dyes," *IJFAC*, vol. 8, no. 3, pp. 126–132, Oct. 2023, doi: 10.24845/ijfac.v8.i3.126.

[138] V. Javanbakht and M. Mohammadian, "Photo-assisted advanced oxidation processes for efficient removal of anionic and cationic dyes using Bentonite/TiO2 nano-photocatalyst immobilized with silver nanoparticles," *Journal of Molecular Structure*, vol. 1239, p. 130496, Sep. 2021, doi: 10.1016/j.molstruc.2021.130496.

[139] S. Sangare, S. Belaidi, M. Saoudi, C. Bouaziz, N. Seraghni, and T. Sehili, "Iron-TiO2 pillared clay nanocomposites: Eco-friendly solutions for photocatalytic removal of organic and pathogen contaminants," *Inorganic Chemistry Communications*, vol. 160, p. 111923, Feb. 2024, doi: 10.1016/j.inoche.2023.111923.

[140] Z. Sun, Y. Chen, Q. Ke, Y. Yang, and J. Yuan, "Photocatalytic degradation of a cationic azo dye by TiO2/bentonite nanocomposite," *Journal of Photochemistry and Photobiology A: Chemistry*, vol. 149, no. 1–3, pp. 169–174, Jun. 2002, doi: 10.1016/S1010-6030(01)00649-9.

Chapter II: Experimental procedures and characterization techniques

1. Introduction

In this chapter, the experimental methodology and characterization techniques employed in this thesis are presented, including the chemical reagents, catalyst synthesis protocols, and photocatalytic evaluation. The characterization techniques employed include thermo-gravimetric and differential scanning calorimetry (TG/DSC), X-ray diffraction (XRD), Brunauer-Emmett-Teller (BET) surface area analysis, Fourier-transform infrared spectroscopy with attenuated total reflectance (FTIR-ATR), point of zero charge determination (pH_{pzc}), and UV–Vis diffuse reflectance spectroscopy (UV-Vis DRS).

2. Experimental procedures:

2.1. Chemicals:

- The chemicals II.1 were used without prior purification to synthesize the catalysts or adjust the pH of solutions.

Table II.1. Chemical product properties and utilisation

Chemical product	Formula	Purty	Provenance	Utilisation
Titanium tetra-isopropoxide	$Ti\ (OC_3H_7)_4$	97%	Sigma-Aldrich	Reagents of synthesis
Nitric acid	HNO_3	69%	Sigma-Aldrich	
Ethanol	C_2H_5OH	96%	Riedel-de Haen	
Sulfuric acid	H_2SO_4	96%	Sigma-Aldrich	Adjustment of pH
Sodium Hydroxide	NaOH	≥ 97%	Biochem Chemopharma	
Distilled water	H_2O	-	LAMES laboratory	Preparation of the solution and the hydrolysing agent
Degussa P-25	TiO_2	99.5	Sigma Aldrich	Comparison with the synthesized TiO_2
Bentonite	$Al_2O_3\ 2SiO_2\ 2H_2O$	Natural product	Western Algeria	Synthesis of TiO_2-BN composite

- The Rhodamine B dye (RhB) has been selected as a model of organic pollutants in this study. Table II.2 shows its physicochemical properties. Rhodamine B is a synthetic organic dye commonly used as a tracer in water studies to evaluate flow characteristics, including volume, rate, and direction. Due to their fluorescent properties, rhodamine dyes can be detected efficiently and cost-effectively using devices known as fluorometers. As an artificial dye, it exhibits low biodegradability and can remain in aquatic environments, causing environmental problems.

Table II.2. Physicochemical properties of Rhodamine B dye

Commune name	Rhodamine B 
Chemical formula	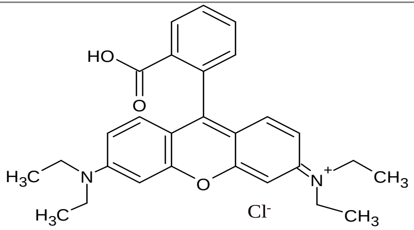
Name (IUPAC)	Chloride of [9-(2-carboxyphenyl)-6-diethylamino-3-xanthenylidene]-diethylammonium
Chemical formula	$C_{28}H_{31}CIN_2O_3$
Molecular weight (g/mol)	479.02
pKa	3.4
λ_{max} (nm)	553
Solubility ($mg.L^{-1}$)	$1,2 \times 10^4$
Henry constant ($atm .m^3. mol^{-1}$)	$2,2 \times 10^{-21}$
Class	Cationic dye
Name (CI)	Basic Violet 10
Henry constant	$2,2 \times 10^{-21}$

A scan over a range of 200 to 800 nm was carried out for a solution of RhBat a concentration of 10 mg/L in a natural pH of 4.80. According to the absorption spectrum, the maximum absorption wavelength of Rhodamine B is 553 nm, as shown in the Figure II.3 (a).

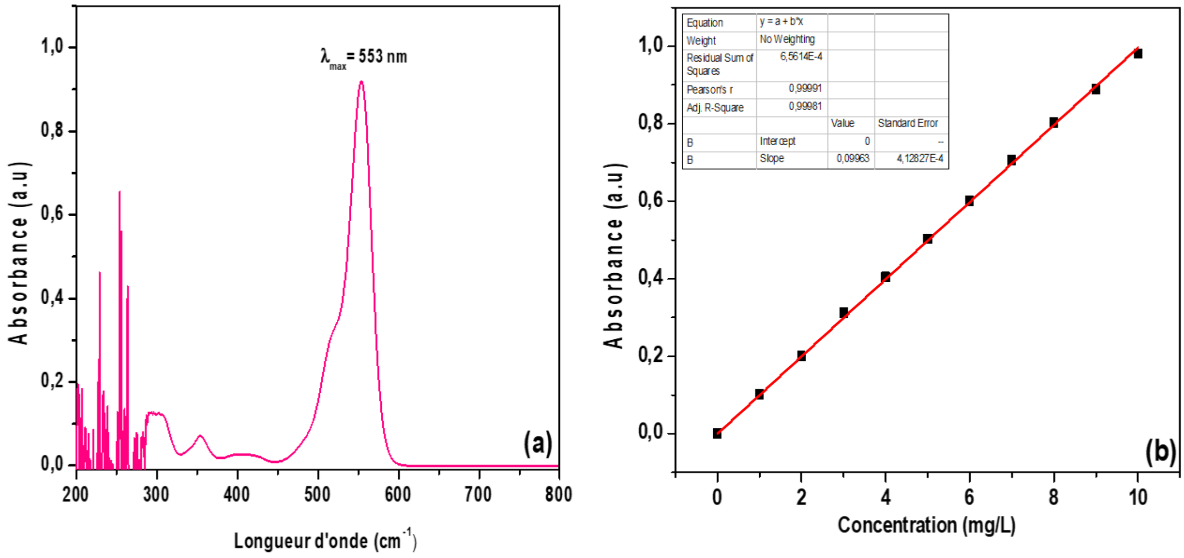

Figure II.1. (a) Absorption spectrum of Rhodamine B in aqueous solution (10 mg/L), (b) Rhodamine B calibration curve

The calibration curve was established using RhB dye solutions at various concentrations, as measured by UV spectroscopy. The RhB concentrations ranged from 1 to 10 mg/L. The calibration was performed within the linear range defined by the Beer-Lambert law and was subsequently used to convert absorbance values obtained during the photodegradation experiments into RhB concentrations. The final dye concentration was determined from absorbance values using the following equation:

$$C = \frac{\text{A−intercept}}{\text{slope}} \qquad \text{(Equation II.1)}$$

C represents the concentration of RhB in solution, and A is the absorbance measured at 553 nm.

2.2. Photocatalyst preparation:

2.2.1. Synthesis of TiO_2 nanoparticles:

The synthesis of TiO_2 nanoparticles was carried out using a non-conventional sol-gel method, as described by V.T. Lukong et al [1]. In this study, Titanium tetraisopropoxide was dissolved in ethanol (1:5 *v/v*) under vigorous stirring (550 rpm) at ambient temperature for 30 minutes**,** forming a white colloidal suspension. A diluted HNO_3 solution (pH = 3) was then gradually added dropwise to facilitate precursor hydrolysis**.** The mixture was stirred at 60°C for another hour to ensure complete hydrolysis and then dried at 100°C. The obtained titania xerogel was crushed and calcined at 400, 600, and 800°C for 2 hours to get a nanocrystalline TiO_2. The experimental scheme is shown below in Figure II.3:

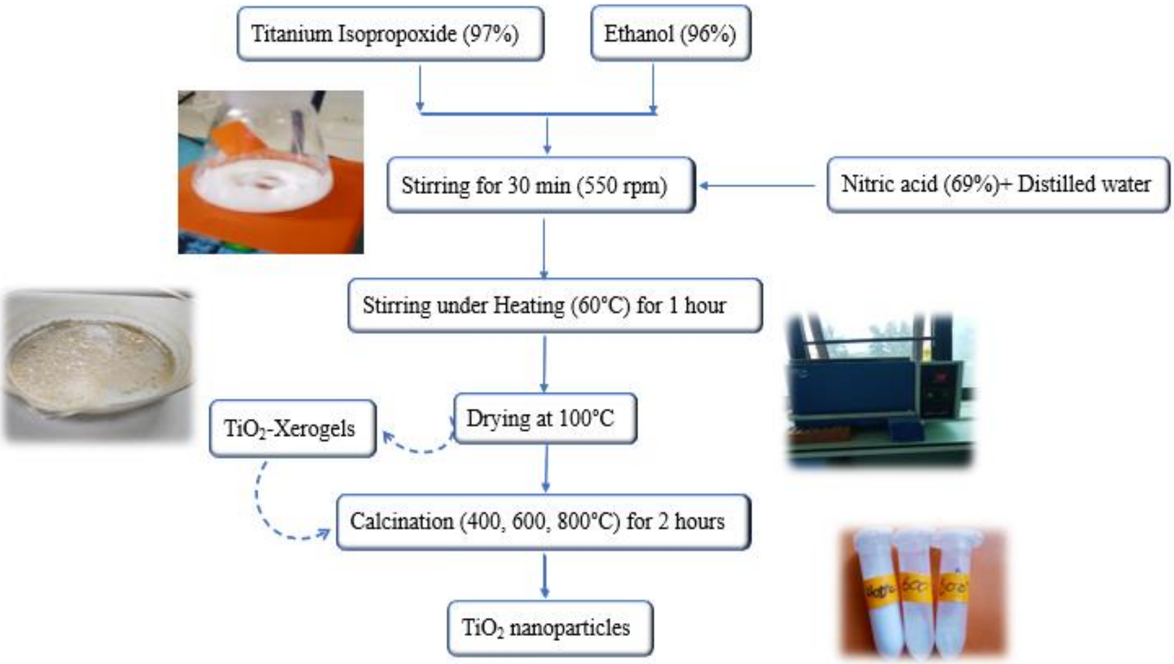

Figure II.2. Flow chart of the synthesis method of TiO_2 nanoparticles by the non-conventional sol-gel method.

2.2.2. Synthesis of TiO_2-bentonite composites (TiO_2-BN):

Before using the clay, a portion of bentonite was washed with distilled water and dried in an oven for 24 hours at 105°C to remove impurities.

Titanium dioxide/Bentonite composites (TiO_2-BN) were synthesized at different weight ratios of TiO_2 (10%, 30%, and 50%) using the non-conventional sol-gel method, which involved the synthesis of TiO_2 nanoparticles as shown in the Figure II.3. A known amount was added to the mixture of the Titanium tetra-isopropoxide and ethanol after stirring for 30 min (550 rpm). The nitric acid (pH 3) was added dropwise under continuous stirring. The mixture was stirred and heated at 60°C for another hour. After being dyed at 100°C for 24 hours, the sample was calcined at 400°C for 2 hours to obtain the TiO_2-BN composites. Figure II.5 displays the morphological appearance of the raw bentonite, TiO_2-400, and the 50% TiO_2-bentonite composite samples. The observed variation in colour and texture among the samples reflects the physicochemical changes induced by the incorporation of TiO_2 into the bentonite matrix.

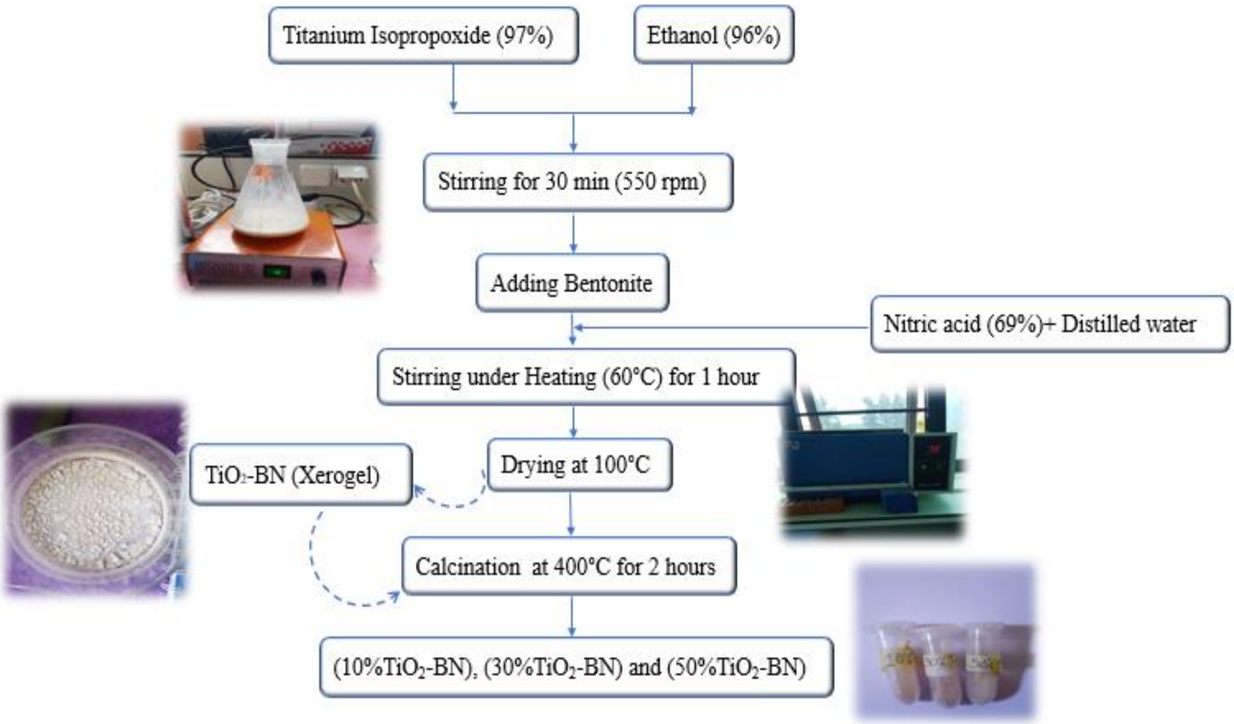

Figure II.3. Flow chart of the synthesis method of TiO_2-BN composites by non-conventional sol-gel method.

Figure II.4. Physical aspect of Bentonite, TiO_2-400 °C, and 50% TiO_2-BN samples

2.3. Photocatalytic studies:

This test examines the photodegradation of a persistent organic pollutant through the heterogeneous photocatalysis process, used the synthesised samples. Figure II.6 illustrates that the cylindrical water-jacketed photoreactor (400 ml) promotes the homogeneity of mobile photocatalyst diffusion with a magnetic stirrer. A commercial UV lamp (λ = 254 nm, intensity = 5400 µW/cm²) served as the light source; another lamp was used to compare the effect of intensity and wavelength (λ = 365 nm, intensity = 1280 µW/cm²) on the photodegradation process. The photocatalytic activity of the samples was evaluated at room temperature. Before the photodegradation tests, the suspension was vigorously stirred magnetically in the dark for 30 minutes under constant stirring at 350 rpm to ensure adsorption-desorption equilibrium. During the experiment, aliquots (5 mL) were drawn from the suspension at regular intervals and centrifuged at 3500 rpm for 15 minutes to remove solids. The residual concentration was analyzed using UV–vis spectrophotometry (JENWAY 6300, U.K.). The concentration of RhB after illumination was monitored at λ = 553. The photodegradation efficiency (R%) was substantially estimated from the equation:

$$\boldsymbol{R}(\%) = \left(\frac{\boldsymbol{C0-Ct}}{\boldsymbol{C0}}\right) \times \mathbf{100} \qquad \textbf{(Equation II.2)}$$

C_0 and C_t are the dye concentrations at the initial and defined time t, respectively.

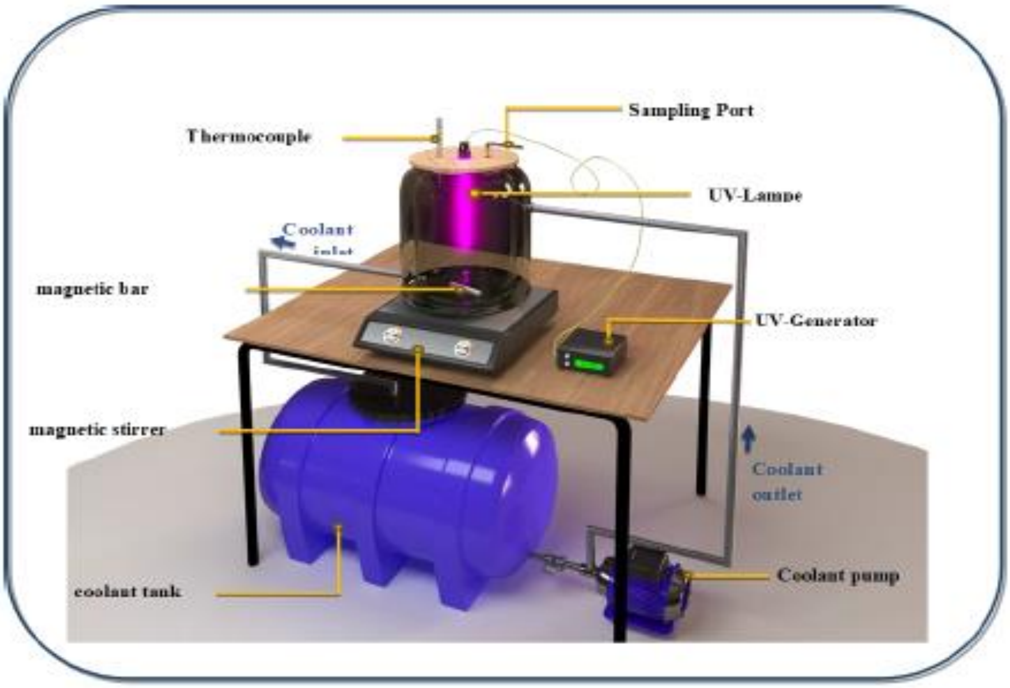

Figure II.5. Photocatalytic Reactor Setup for UV Irradiation Experiments.

3. Characterization techniques:

3.1. X-ray diffraction (XRD):

X-ray diffraction (XRD) is an analytical technique used to measure the average spacing between different crystalline planes, determine the orientation of a single crystal or grain, study the crystal structure of an unknown material, and measure the size, shape, and internal stress of small crystalline regions. Since the wavelength of X-rays is in the range of the distances between the atoms in a crystal lattice, a special interference phenomenon of diffraction can provide information about the distances between the atoms. X-ray wavelengths typically range from approximately 10 nm to 0.01 Å (1×10^{-3} nm) [2]. X-ray diffraction (XRD) analyses were performed using a Bruker D2 PHASER diffractometer employing Cu Kα radiation ($\lambda = 1.5406$ Å). Data were collected over a 2θ range of 10-80° in continuous scanning mode, with a step size of 0.010° and a counting time of 19.10 s per step.

Figure. II.6. Bruker 2D PHASER diffractometer used for XRD measurements (Technology platform for the physicochemical Analysis, CRAPC, University of Constantine, Algeria)

This technique involves placing material onto a cylindrical sample holder, which is positioned at the centre of the diffractometer chamber and rotates around a vertical axis. The electromagnetic waves (X-rays) of wavelength λ that are applied to the sample interact with the electron clouds of the atoms comprising the crystal lattice of the material, characterized by interplanar spacings hkl, where h, k, and l are Miller indices. The diffracted rays are detected as signals, which are subsequently processed to enable the identification of crystalline phases and the determination of the unit cell parameters of the analyzed sample. Bragg’s law (Equation II.3) demonstrates that the diffraction angles are related to the characteristics of the crystal lattice and the incident radiation (wavelength λ) (see Figure II.8). Thus, each family of crystallographic planes (hkl) corresponds to a diffracted ray.

$2.d_{hkl}\sin\theta = n.\lambda$ (Equation II.3)

Where:

- hkl (Å): interplanar distance between two planes of the (hkl) family;
- θ (°): angle between the incident and diffracted beams (Bragg angle);
- λ (Å): wavelength of the incident beam;
- n: order of Bragg diffraction.

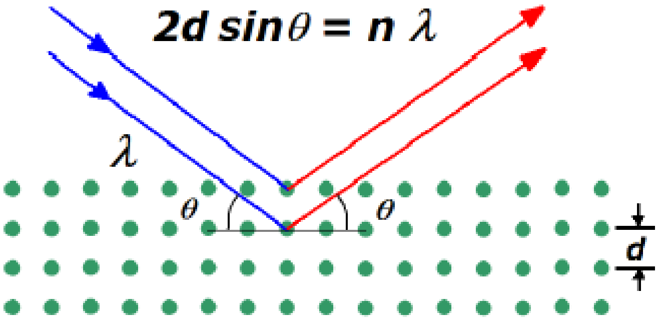

Figure II.7. schematic diagram of Bragg's law [2].

3.2. Transform Infrared Spectroscopy- Attenuated Total Reflectance (FTIR-ATR):

Attenuated total reflectance (ATR) is the most widely used sampling methodology for Fourier transform infrared (FTIR) spectroscopy (Figure II.9**)**. ATR-FTIR quickly and easily measures a broad range of sample types, including liquids, solids, powders, semisolids, and pastes. Fourier-transform infrared (FTIR) spectroscopy is a non-destructive absorption spectroscopic technique. This characterization method allows the identification of functional groups present in the sample based on the vibrational modes of molecular bonds. The infrared radiation range is divided into near, mid, and far IR. We are particularly interested in the mid-IR region [4000-400 cm^{-1}], which corresponds to the molecular vibration domain. FTIR analysis was conducted at the technology platform laboratory (CRAPC, University of Biskra).

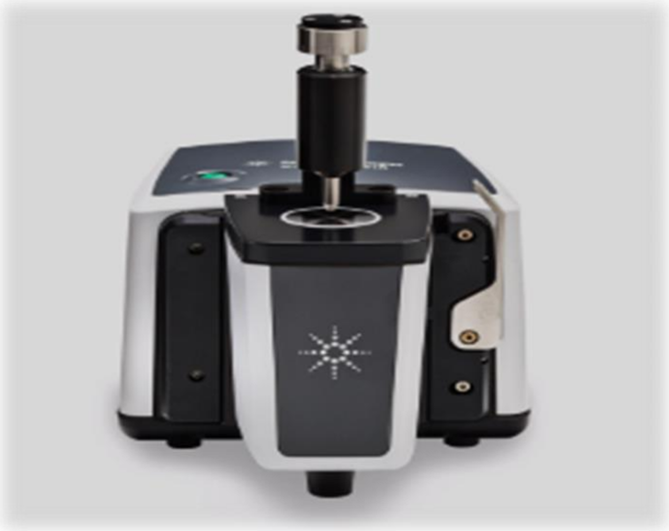

Figure II.8. Spectrometer Agilent for FTIR/ATR analysis, Technology platform for the physicochemical Analysis, CRAPC, University of Biskra, Algeria.

3.3. Morphological analysis (SEM/EDX):

In this study, scanning electron microscopy (SEM) coupled with energy-dispersive X-ray spectroscopy (EDX) was performed at the Technology Platform for Physicochemical Analysis of Materials, CRAPC, University of Constantine. SEM analysis is a non-destructive technique for characterising solid samples. The microscope operated at an accelerating voltage of 20 kV. It aims to image the microstructural characteristics of solid specimens, such as morphology, surface topography, and composition on the micrometre scale. The SEM technique relies on the emission of electrons produced by the cathode (primary electrons) and the detection of secondary electrons that emerge from the surface upon the impact of primary electrons. The images are generated by collecting secondary electrons with a detector consisting of a scintillator coupled to a photomultiplier. In general, the energy dispersive spectrometry (EDX) coupled with SEM is used to analyse and perform quantitative assessments of the chemical composition of samples .

Figure II.9. (a) scanning electron microscopy (SEM) and (b) Energy dispersive spectrometry (EDX), Technology platform for the physicochemical Analysis, CRAPC, University of Constantine, Algeria.

1.4. Brunauer- Emmett- Teller (BET) :

The specific surface area of the samples studied was measured using the BET (Brunauer-Emmett-Teller) method. The principle of this method is based on the physisorption of gas molecules onto the surface of the solid; in this study, nitrogen was employed as the adsorbate. The quantity of gas physisorbed at the material's surface is measured under specific temperature and relative pressure P/P_0 of the gas used, where P_0 is the saturation vapour pressure of the gas. This analysis was conducted at the technology platform for the physicochemical Analysis, CRAPC, University of Constantine. The instrument used was a Nitrogen adsorption apparatus (2017, Quantachrome, version 5.21) (Figure II.11). After degassing at 80°C under vacuum for 600 min, the mass of the sample was measured before and after analysis.

Figure II.10. Nitrogen adsorption apparatus (2017, Quantachrome instruments, version 5.21) (Technology platform for the physicochemical Analysis, CRAPC, University of Constantine, Algeria).

3.5. Thermogravimetric-differential scanning calorimetry (TG/DSC):

Thermogravimetry/Differential Scanning Calorimetry (TG/DSC) is a coupled thermal analysis technique that simultaneously monitors mass variations and heat flow of a sample under a controlled atmosphere (inert or oxidizing). Thermogravimetry (TG) measures the sample's loss or gain of mass, enabling the detection of phenomena such as dehydration, thermal decomposition, or oxidation. On the other hand, DSC (Differential Scanning Calorimetry) records the heat flows associated with physical or chemical transformations (endothermic or exothermic reactions), such as melting, crystallisation, or phase transitions. The TG/DSC combination provides valuable information for characterising the studied materials' thermal stability, decomposition stages, and thermodynamic properties. In our study, the thermal transformation of TiO_2-xerogel was analyzed using differential thermal scanning calorimetry and thermal gravimetric analysis (TG/DSC) with the Mettler Toledo STARe System TGA/DSC 3+ instrument, applying a heating rate of 10°C/min from room temperature to 1000 °C, followed by cooling back to room temperature. The analysis took place at the technology platform for the physicochemical analysis of materials, CRAPC, University of Constantine.

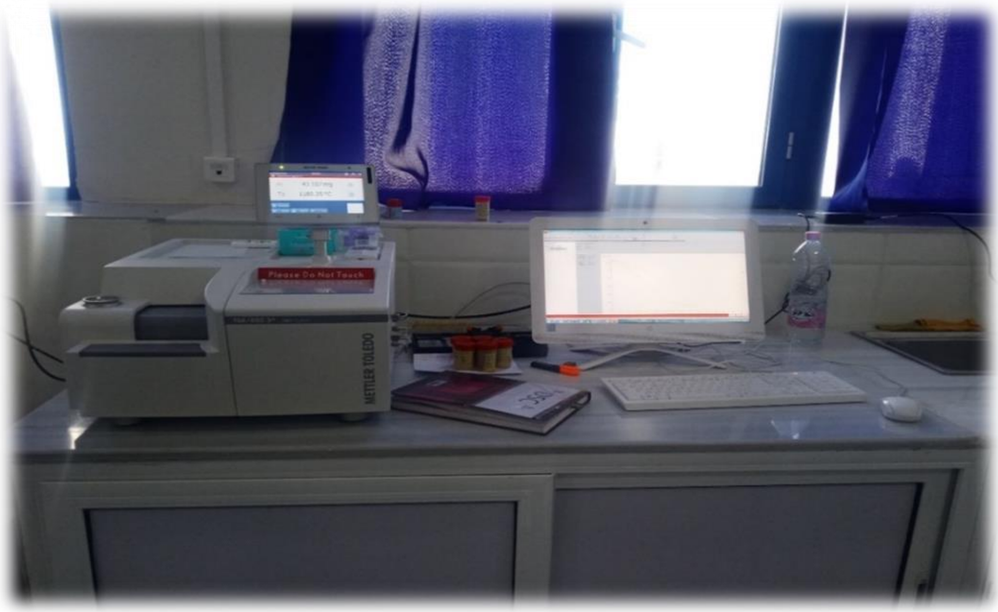

Figure II.11. Differential thermal scanning calorimetric and thermal gravimetric analysis (TG/DSC) apparatus. (Technology platform for the physicochemical Analysis, CRAPC, University of Constantine, Algeria).

3.6. UV/Visible spectroscopy

The spectroscopic technique was used to determine the band gap energy (Eg) of synthesized TiO_2 samples. In our study, the ultraviolet-visible (UV-vis) spectroscopic analysis of our samples was carried out at the research laboratory of the Laboratory USTHB university in the 200-900 nm range using a UV-Visible spectrometer (UV-VIS Double-Beam Spectrophotometer from Jasco (model V-650) (Figure II.13). The gap energies (E_g) were calculated using the Tauc formula (equations II.4 and II.5):

$$F(R)\,(h\nu)^2 = A\,h\nu - E_g \qquad \text{(Equation II.4)}$$

$$F(R) = [\,1 - R / 2R\,] \qquad \text{(Equation II.5)}$$

Where:
F(R) : Kubelka-Munk equation
$h\upsilon$: lumineuses Energy
A: constant
Eg: Band gap Energy

The principle of this technique is based on the interaction of light with matter. When a beam of light of intensity I_0 strikes the surface of a sample, the chemical species changes its energy state from E_n to E_{n+1} through energy absorption or vice versa. On the other hand, the sample transmits a portion of light of intensity I weaker than the incident intensity I_0. The photometer therefore measures and compares the intensity emitted by the source and reflected by the sample.

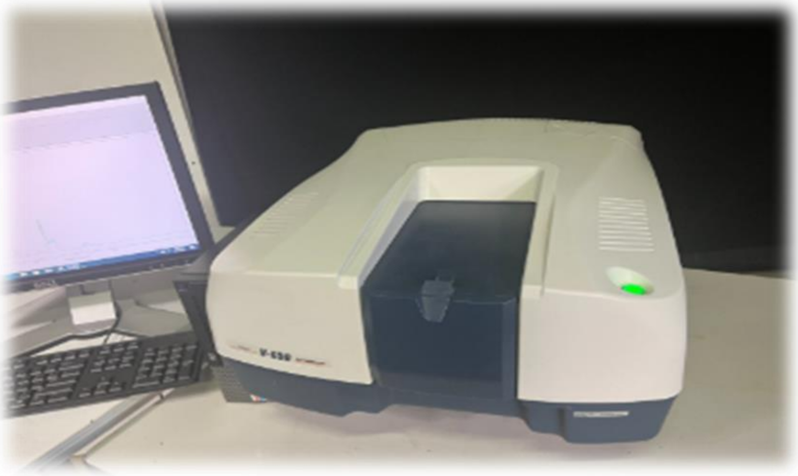

Figure II.12. V-650 UV-VIS Double-Beam Spectrophotometer from Jasco (Technology platform for the physicochemical Analysis, CRAPC, University of USTHB, Algeria)

3.7. Point of zero charge (PZC) analysis:

The Point of zero charge (PZC) is the pH value at which the sample's surface exhibits a zero charge, and all the active sites are neutral [3]. Its value was determined by the method described by Reham et al [4].

Figure II.14. Procedure of the determination of the point of zero charge (PZC)

In 5 beakers, 0.1 g of the sample was added to 50 mL of $NaNO_3$ (0.1 N) solution with different pH values, ranging from 2 to 11, using NaOH or HNO_3 solution (0.1 mol/L). After 24 hours of stirring at room temperature, the final pH (pH_f) of each suspension was noted. pH_{pzc} is the Point of intersection of the curve (pH_f-pH_i) as a function of initial pH (pH_i) and the x-axis.

4. Conclusion

This chapter presents the synthesis routes, experimental protocols, and characterization techniques used to investigate the structural, surface, and optical characteristics of the synthesised TiO_2 and TiO_2-BN materials. The adopted synthesis method, notably the modified sol-gel process followed by calcination at various temperatures, aims to enhance the photocatalytic activity of the materials. A range of characterisation tools, including TG/DSC, XRD, BET, FTIR-ATR, pH_{PZC}, and UV-Vis DRS, provides essential insights into the properties governing their photocatalytic behaviour. The information gathered here establishes the necessary groundwork for interpreting photocatalytic performance for the photodegradation of Rhodamine B, which will be explored in the following chapters.

References:

[1] V. T. Lukong, K. O. Ukoba, and T. C. Jen, "Heat-assisted sol–gel synthesis of TiO_2 nanoparticles: structural, morphological and optical analysis for self-cleaning application," *Journal of King Saud University - Science*, vol. 34, no. 1, p. 101746, Jan. 2022, doi: 10.1016/j.jksus.2021.101746.

[2] M. A. Fendrich, "Solar concentration for the environment industry: photocatalytic materials and application technologies".

[3] T. Mahmood, M. T. Saddique, A. Naeem, P. Westerhoff, S. Mustafa, and A. Alum, "Comparison of Different Methods for the Point of Zero Charge Determination of NiO," *Ind. Eng. Chem. Res.*, vol. 50, no. 17, pp. 10017–10023, Sep. 2011, doi: 10.1021/ie200271d.

[4] T. U. Rehman *et al.*, "Fabrication of stable superabsorbent hydrogels for successful removal of crystal violet from waste water," *RSC Adv.*, vol. 9, no. 68, pp. 40051–40061, 2019, doi: 10.1039/C9RA08079A.

[5] I. Arora, H. Chawla, A. Chandra, S. Sagadevan, and S. Garg, "Advances in the strategies for enhancing the photocatalytic activity of TiO2: Conversion from UV-light active to visible-light active photocatalyst," *Inorganic Chemistry Communications*, vol. 143, p. 109700, Sep. 2022, doi: 10.1016/j.inoche.2022.109700.

Chapter III: Results and discussion

Part 1: Photodegradation of Rhodamine B using TiO_2 nanocatalyst synthesized via non-conventional sol-gel method

1. Introduction

This chapter presents the characterization results and photocatalytic activity of TiO_2 nanoparticles prepared via a non-conventional sol-gel method, calcined at 400, 600, and 800°C. A comprehensive analysis was performed, using XRD, TG/DSC, FTIR/ATR, and SEM/EDX techniques. The BET surface area, pH_{pzc}, and the band gap of the samples were also measured. The photodegradation efficiency of Rhodamine B (RhB) with TiO_2 materials was examined under UV irradiation, emphasising the effects of operational parameters such as initial dye concentration and photocatalyst loading for each calcined. sample. A detailed analysis of pH changes and light wavelengths was conducted on the sample calcined at 400°C. The photocatalytic performance of TiO_2 nanocatalysts was benchmarked against the commercial Degussa P-25.

2. Characterisation:

2.1. TG/DSC analysis of TiO_2-xerogel:

Thermogravimetric and differential scanning calorimetry (TG/DSC) analyses were conducted to evaluate the thermal stability of the samples and identify phase transitions.

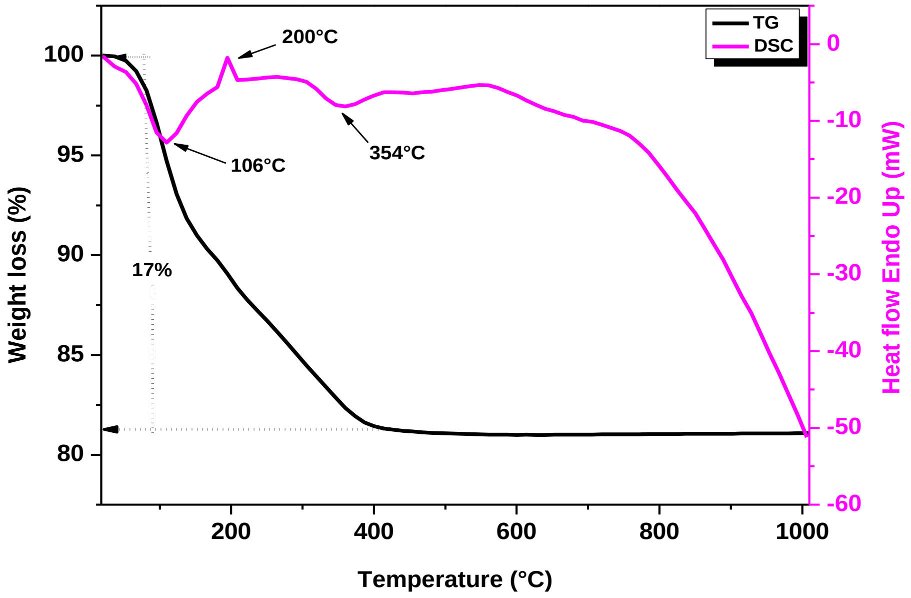

Figure III.1. TG/DSC curves of TiO_2 -Xerogel

The (TG/DSC) curves for TiO2-Xerogel are shown in Figure III.1. The thermogram plot revealed that the sample had a sharp weight loss (17%) in the range of 80-400°C accompanied by two endothermic peaks of DSC at 106°C caused by evaporation of moisture and another peak at 354°C attributed to oxidative decomposition of the residues or intermediate products formed during the synthesis [1]. Other exothermic peaks were observed in the DSC at 200°C due to the transformation from the amorphous to the anatase phase [2], [3]. The XRD results explain these observations.

2.2. XRD and BET analysis :

X-ray diffraction (XRD) analysis was conducted to determine the crystalline structure, phase composition, and crystallite size of TiO_2 nanoparticles synthesized via a non-conventional sol-gel method and calcined at different temperatures. The XRD pattern of different TiO_2 nano 289 catalysts are shown in Figure 4. Distinct peaks at 2θ= 25.35°, 37,78°, 48,07°, and 75,09° (JCPDS290 card no. 21-1272) correspond to (101), (004), (200), and (215) planes of the anatase phase, respectively. While the peaks at 2θ= 27.44°, 36.09°, 41.25°,54.33°, 62.78° 69.02°, and 76.62° (JCPDS card no. 21-1276) corresponding to (110), (101), (111), (211), (002), (301) and (202) planes of rutile structure. The crystallite sizes were calculated using the Debye–Scherrer equation [4]:

$$D = \frac{K\lambda}{2\beta\cos\theta\alpha} \qquad \text{Equation III.1}$$

Where D is the size of the crystallite, λ is the wavelength of Cu$K\alpha$ radiation (λ = 1.5406 Å), θ is the Bragg angle of diffraction, and β is the full width at half maximum (FWHM).

The fractions of anatase and rutile in each sample were calculated using the Spurr and Myers equations [5]:

$$A = \left(\frac{1}{1+1.26\frac{IR}{IA}}\right) \times 100 \qquad \text{Equation III.2}$$

F_A represents the weight fraction of anatase. I_R and I_A are the intensities of the diffraction peaks for rutile (110) and anatase (101), respectively.

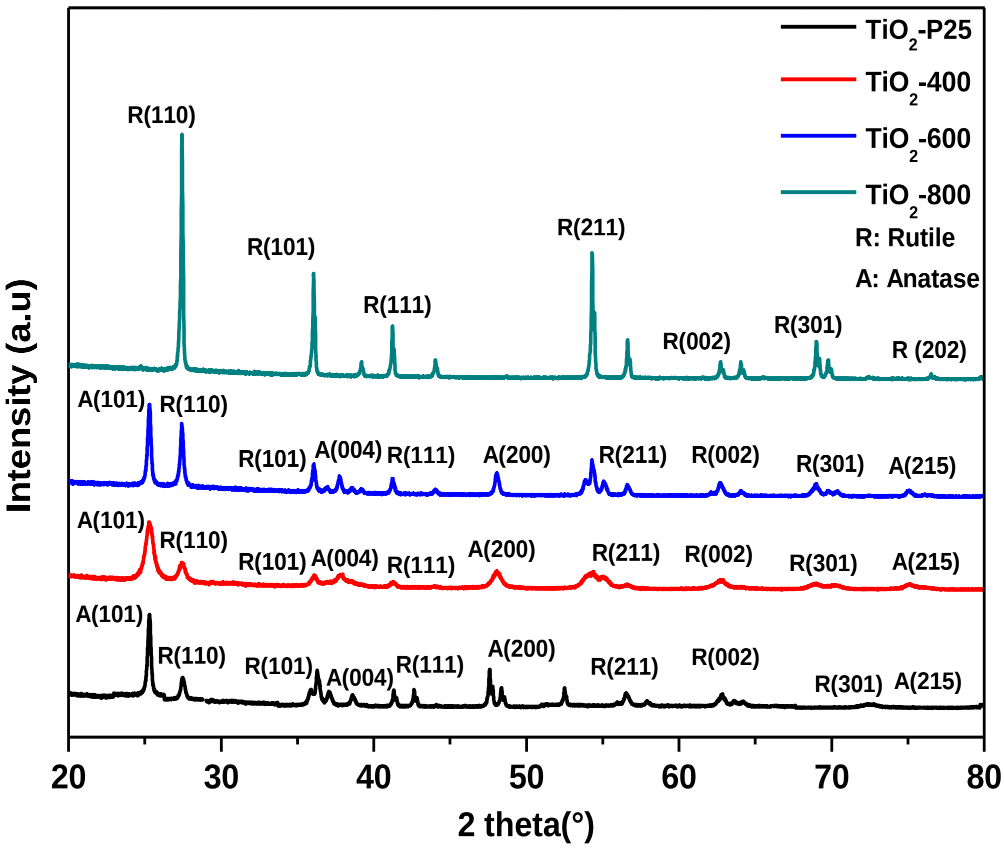

Figure III.2. XRD patterns of TiO_2 samples

The XRD analysis patterns indicated the presence of anatase and rutile phases for TiO_2-400 and TiO_2-600, and rutile for the TiO_2-800 sample. The transformation from anatase to rutile in the nanocomposites is promoted by increasing the calcination temperature [6]. This transformation was confirmed by TG/DSC analysis.

As shown in Tab.2, the anatase phase composition decreased with increasing calcination temperatures from (67,89 %) until the formation of the rutile phase (100%). The crystallite size of both the anatase and rutile phases gradually increases up to 600 °C. Beyond this temperature, anatase disappears due to the phase transition, as the increasing calcination temperature promotes crystallite growth and induces sintering effect [7]. The calculated crystallite sizes of anatase and rutile were 19.33 and 25.33 nm, for TiO_2-P25. As a well-known commercial photocatalyst composed of a mixed-phase anatase/rutile structure, the content of the rutile and anatase phases was 79.88% and 19.74%, respectively. Therefore, the results of the BET surface area are presented in Table 2. As the calcination temperature increased, the specific surface area decreased significantly, from 62.83 m² g⁻¹ to 2.00 m² g⁻¹, due to the effects of high calcination temperatures on nanocrystalline growth and sintering [8].

Table III.1. Crystalline, optical, and Textural properties of TiO_2 samples.

Samples	Crystallite Size (nm)	Phase composition (%)	BET surface area (m^2/g)	Band gap (eV)	Point zero charge	R (%)
TiO_2-400	Anatase (15.75) Rutile (18.94)	Anatase (67.89) Rutile (32.10)	62.83	3.19	6.3	96,11
TiO_2-600	Anatase (32.60) Rutile (30.45)	Anatase (52.01) Rutile (47.98)	7.03	2.97	6.2	93,37
TiO_2-800	Rutile (37.27)	Rutile (100)	2.00	2.86	5.7	81,25
TiO_2-P25	Anatase (19.37) Rutile (25.23)	Anatase (79.88) Rutile (19.74)	55	3.6	5.6 [9]	92,07

2.3. FTIR-ATR analysis:

Figure III.3 presents the FTIR-ATR spectra of TiO_2 samples calcined at 400 °C, 600 °C, and 800 °C in the range of 400–4000 cm⁻¹. It has been reported that the broad absorption band observed in the 400–900 cm⁻¹ region has been attributed to the vibrational modes of the Ti-O-Ti linkages [10], The distinct peak around 421.8 cm⁻¹, observed for the TiO_2-400 sample, which is commonly attributed to the Ti–O stretching vibration associated with the anatase structure in the TiO_2 lattice, identified as the predominant phase based on XRD analysis [11]. In contrast, the spectra of TiO_2-600 and TiO_2-800 exhibit broader and less intense absorption features in the low-wavenumber region, reflecting changes in the structural characteristics of the materials. For TiO_2-600, the principal absorption bands are observed at 500.61 and 669.19 cm⁻¹, while for TiO_2-800 are located at 514.8 and 698.2 cm⁻¹. These band positions are associated with structural changes, including crystallite growth, increased particle agglomeration, and the phase transition from anatase to rutile at high temperatures, which is consistent with the phase transformation revealed by XRD analysis [12], [13]. Moreover, the peaks at 2364 and 2370 cm⁻¹, observed in the TiO_2-600 and TiO_2-800 samples, respectively, correspond to CO_2 adsorbed from the ambient air during the measurement, as indicated by their very low transmittance values [6].

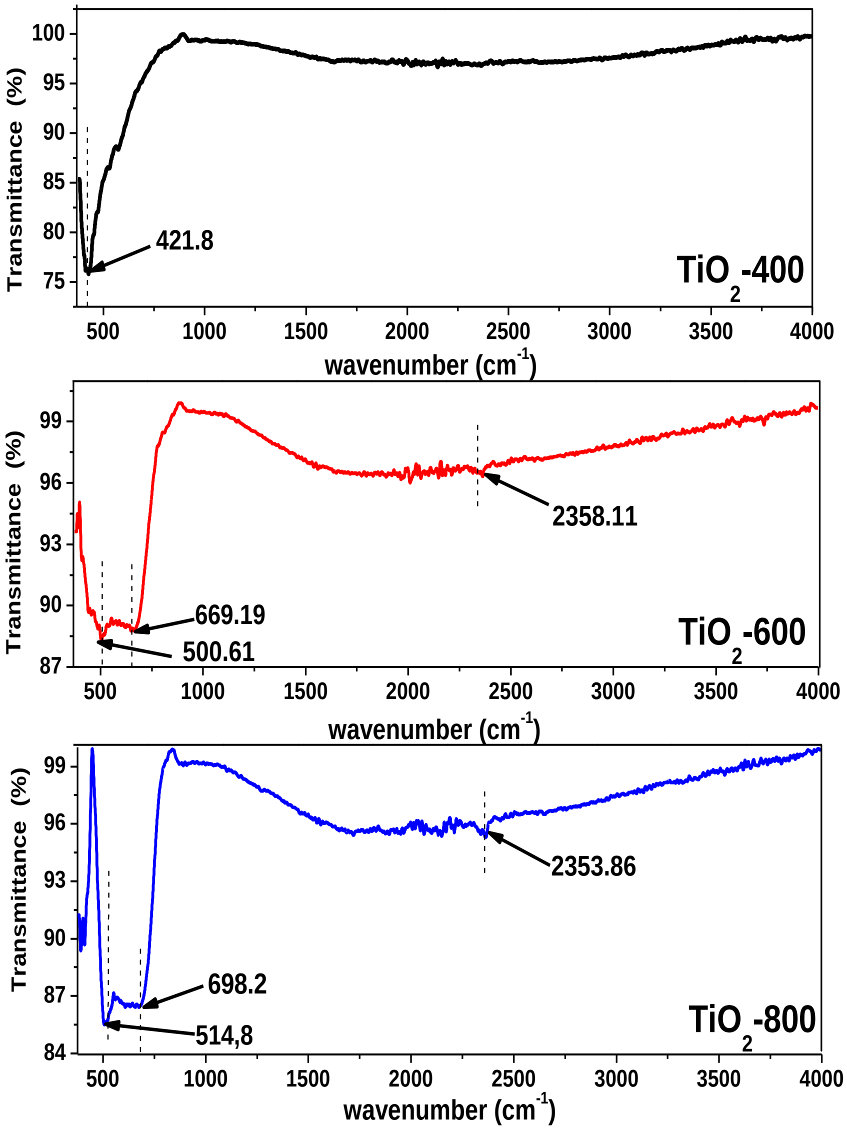

Figure III.3. FTIR-ATR spectra of the TiO_2 samples.

2.4. Morphological analysis (SEM-EDX):

Figure III.4 shows the SEM-EDX images of TiO_2 samples. For the TiO_2-400, there is a wide distribution of particle sizes, including both micrometric particles and smaller ones, which contribute to its high specific surface area. As the calcination temperature increases, smaller particles progressively decrease due to crystallite growth and intensified agglomeration, ultimately resulting in the dominance of larger micrometric particle structures. These results exhibit that TiO_2-400 exhibits nanometric features. A progressive increase in particle agglomeration is observed with increasing calcination temperature, due to the high surface energy of nanostructured particles and sintering effect at high temperatures [14], [15]. This trend reflects temperature-induced sintering and correlates with the observed decrease in surface area and increase in crystallite size [16]. The TiO_2-600 exhibits increased agglomeration and grain growth, as seen in the SEM images, resulting in a reduction in surface area. Nevertheless, its mixed-phase composition enhances photocatalysis due to the synergistic effect between the anatase and rutile phases, which improves charge carrier separation and transport [17], [18].In contrast, the TiO_2-800 sample reveals significant particle growth and dense agglomeration, resulting in a reduced surface area and porosity compared to other samples [19]. Furthermore, while XRD analysis confirmed the nanocrystalline nature of TiO_2, SEM observations revealed micrometric particles, attributed to the agglomeration of nanocrystallites during synthesis and subsequent calcination processes [18], [20]. The elemental analysis pattern (EDX) confirmed the presence of titanium and oxygen ions with different percentages and weights. It also confirms the absence of impurities and successfully synthesizes pure TiO_2 materials.

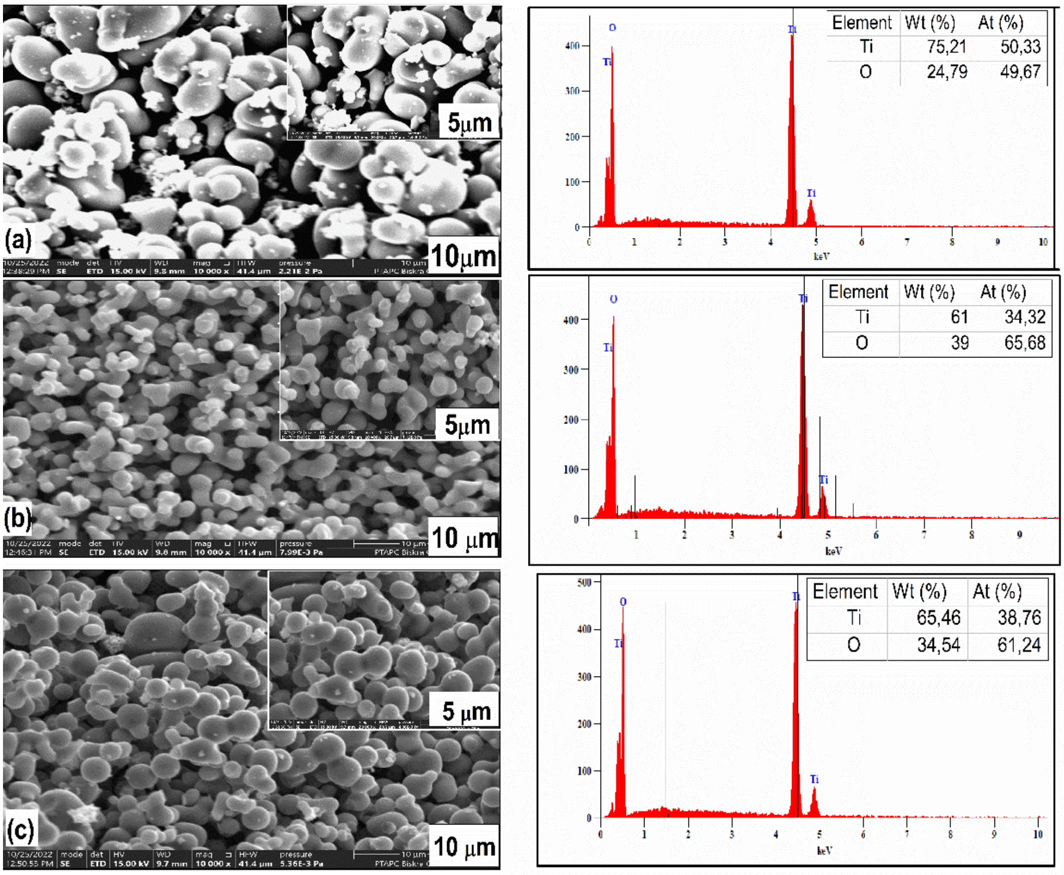

Element	Wt (%)	At (%)
Ti	75,21	50,33
O	24,79	49,67

Element	Wt (%)	At (%)
Ti	61	34,32
O	39	65,68

Element	Wt (%)	At (%)
Ti	65,46	38,76
O	34,54	61,24

Figure III.4. SEM-EDX analysis of TiO_2 samples, (a) TiO_2-400, (b) TiO_2-600, (c) TiO_2-800.

2.5. UV–Vis Spectroscopy:

UV-Vis analysis was conducted to explore the optical properties of TiO_2 materials. The band gap was calculated using the following equation:

$(\alpha h\nu)^n = A\,(h\nu - E_g)$ Equation III.3

where α is the absorption coefficient, E_g is the band gap value of the nanoparticle, hν is the photon energy, A indicate the constant related to the effective masses associated with the bonds, and n represents a value dependent on the nature of the transition (n = 2 for direct transition) [21]. Figure III.5. (a-c) shows the UV-Vis absorption spectra for the synthesized TiO_2 nanoparticles. The maximum absorption edges for the TiO_2-400, TiO_2-600, and TiO_2-800 samples were at 396 nm, 428 nm, and 461 nm, respectively. The absorption edge shifts towards higher wavelengths with increased calcination temperature due to the phase transformation from anatase to rutile [11], [22].

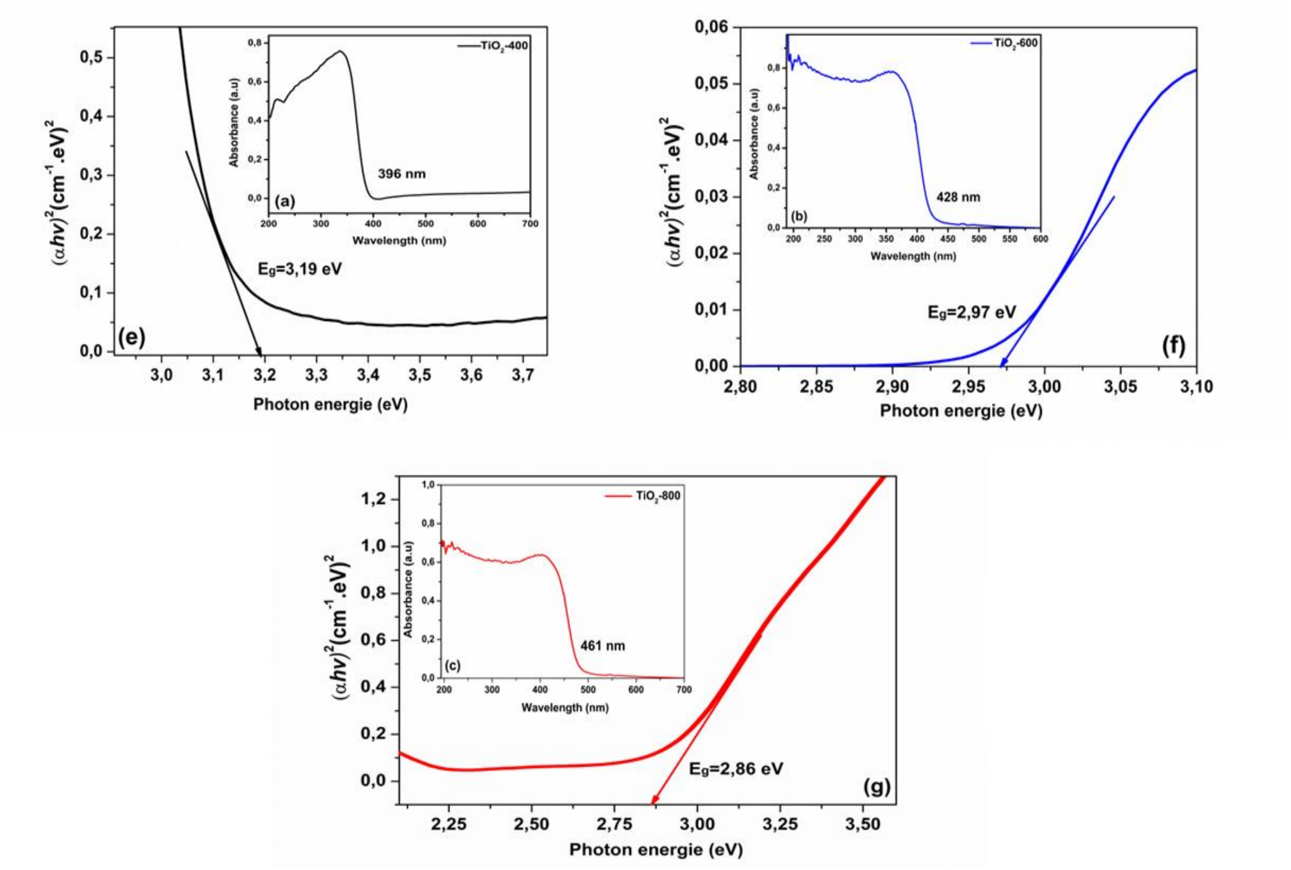

Figure III.5. UV–vis, (a-c) Absorption spectra and (e-g) Tauc plots of TiO_2 samples

Figure III.5. (e-g) displays the Tauc plots of TiO_2 samples. The band gap of TiO_2 nanocatalysts calcined at 400, 600, and 800°C was 3.19, 2.97, and 2.86 respectively, as mentioned in table

III.1. The reduction in band gap energy is attributed to the increase in particle size, crystallinity and the creation of oxygen vacancies (defect sites) at higher calcination temperatures, which agreed with the XRD results [15]. Additionally, the rutile phase is known to exhibit a smaller band gap value than the anatase phase; as the calcination temperature increases, the transformation from anatase to the rutile phase is favoured, attributed to the decrease in the band gap [2].

2.6. Zero Point Charge (PH_{pzc}):

The pH at which the surface charge is neutral is defined by the pH of point zero charge (PZC) [23]. Figure .8 shows the variation of the point of zero charge (pH_{pzc}) for all calcined TiO_2 samples. As reported in the literature, the pH_{pzc} for anatase and rutile ranges from 2 to 8.9 [24]. The PZC values presented in Table 1 are 6.3, 6.2, 5.7 and 5.6 for samples TiO_2-400, TiO_2-600, TiO_2-800 and TiO_2-P25, respectively. The PZC of the mixture (Anatase-rutile) samples is slightly bigger than that of the rutile sample [25], [26]. Studies demonstrate that solids with a reduced specific surface area often exhibit lower PZC values. However, in the case of the same TiO_2 polymorphs, the variations in PZC values induced by changes in calcination temperature remain negligible, despite modifications in surface area, hydroxyl group density, and crystallinity [27],[28].

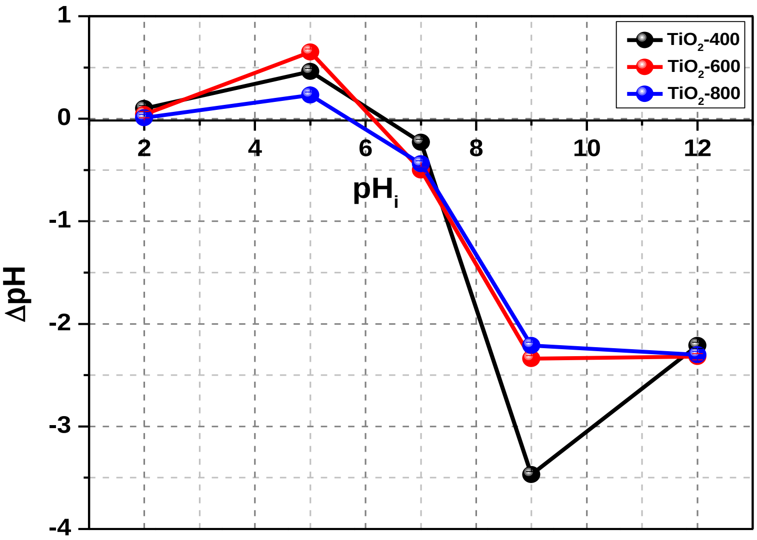

Figure III.6. PZC determination of TiO_2 samples

Accordingly, the key structural, textural, and morphological features of synthesized TiO_2 materials are summarized to establish their correlation and highlight the relationships between these properties. In this context, X-ray diffraction (XRD) analysis revealed that increasing the calcination temperature influenced the crystalline structure of TiO_2, promoting the formation of a mixed anatase–rutile phase and a predominant rutile phase at higher temperatures. This phase evolution was further supported by TG/DSC analysis, which showed thermal transitions corresponding to the amorphous-to-anatase transformation and the subsequent growth of the rutile phase. In addition, FTIR spectra also exhibited temperature-dependent variations in Ti–O–Ti vibrations, consistent with the anatase-to-rutile transition indicated by XRD. Moreover, the specific surface area decreased significantly with calcination, from 62.83 m^2/g to 2 m^2/g, accompanied by an increase in particle size due to crystallite growth, as confirmed by SEM analysis. In addition, the band gap energy decreased with a rise in calcination temperature, due to the progressive formation of the rutile phase, which enhances visible light absorption. Finally, the pH_{pzc} measurements of all calcined samples revealed slight variations in surface charge properties with increasing calcination temperature, which influence dye catalyst interactions during photocatalysis

3. Results and discussion

3.1. Evaluation of photocatalytic performance of TiO_2 samples:

The evaluation of the photocatalytic performance of calcined TiO_2 samples with different textural, optical, and morphological properties was investigated by studying the effect of photocatalyst loading and initial concentration on each calcined sample. The effect of the initial pH of the solution and irradiation source was investigated for the sample TiO_2-400**.** The impact of calcination Temperature on Rhodamine B photodegradation efficiency was discussed, providing in-depth insight into the relationship between the physicochemical properties of TiO_2 material and the photodegradation efficiency of Rhodamine B dye.

3.1.1. Effect of photocatalyst loading:

The effect of calcined catalyst loading on Rhodamine B was investigated by varying the TiO2 nano-catalyst loading from 0.03 to 0.1 g/L, while maintaining a constant concentration of RhB dye (10 ppm) at natural pH for all experiments (Figure III.7). No significant dye adsorption was observed. Furthermore, increasing the catalyst loading for all samples leads to higher photodegradation efficiency, as a greater amount of photocatalyst provides more active sites for the generation of hydroxyl radicals under irradiation [29].

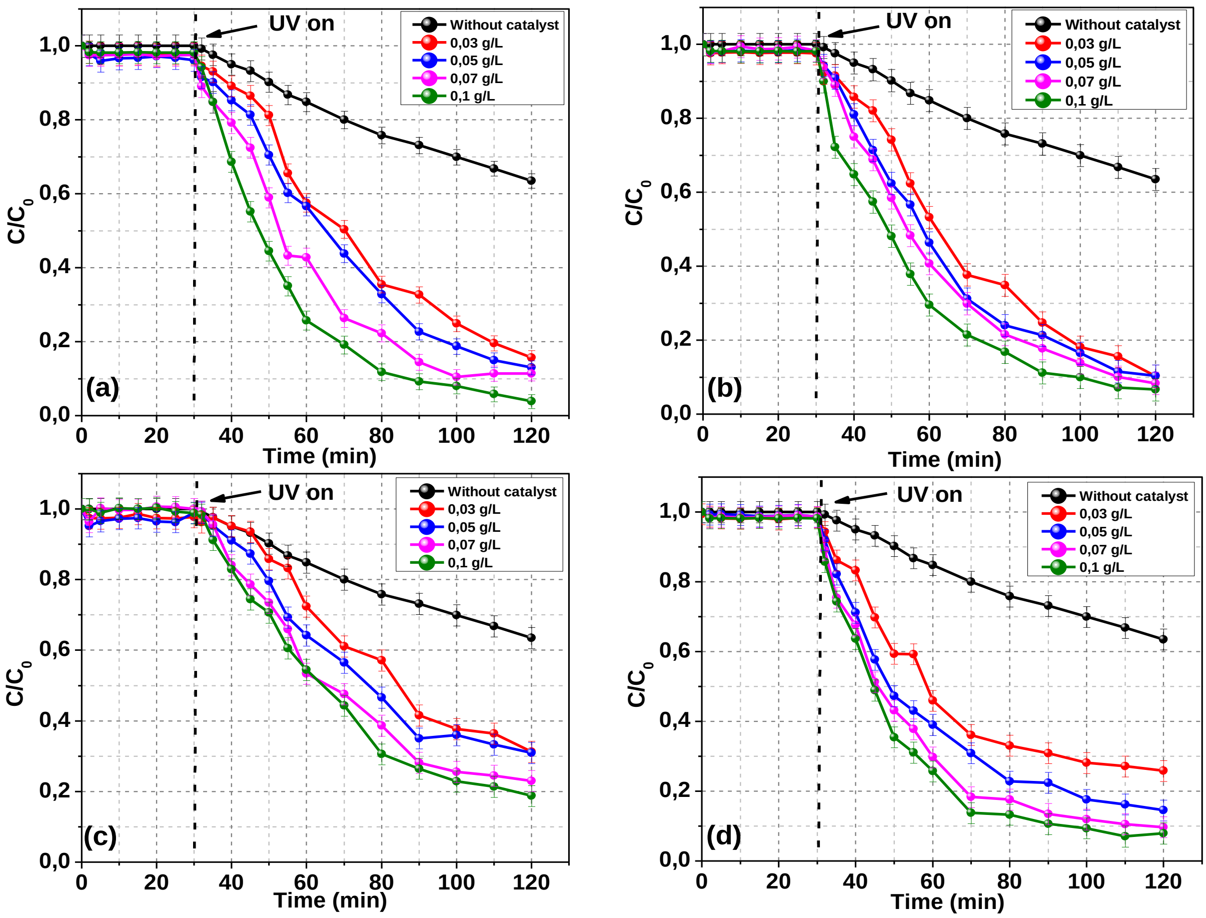

Figure III.7. Effect of TiO_2 loading on the photodegradation of Rhodamine B dye **(a)** TiO_2-400, **(b)** TiO_2-600, **(c)** TiO_2-800, **(d)** TiO_2-P25.

(Operational parameters: UV lamp: λ_{254nm}, intensity 4750 µW/cm², $[TiO_2]_0 = 0.1$ g/L, $[RhB]_0 = 10$ ppm; natural pH = 4.80)

3.1.2. Effect of initial dye concentration:

Figure III.8 illustrates the influence of the initial Rhodamine B concentration on the photocatalytic performance of all calcined TiO_2 samples at a fixed photocatalyst loading of 0.1 g/L. Degradation experiments were conducted with initial dye concentrations ranging from 1 to 10 ppm under natural pH conditions (pH 4.80), following 30 minutes of adsorption–desorption equilibrium and 90 minutes of UV irradiation. As expected, the photocatalytic degradation efficiency of all samples decreased with increasing initial Rhodamine B concentration under UV irradiation. This decline can be attributed to the higher number of dye molecules competing for adsorption sites on the photocatalyst surface, thereby reducing the availability of active sites necessary for hydroxyl radical generation and consequently diminishing the photocatalytic activity [30].

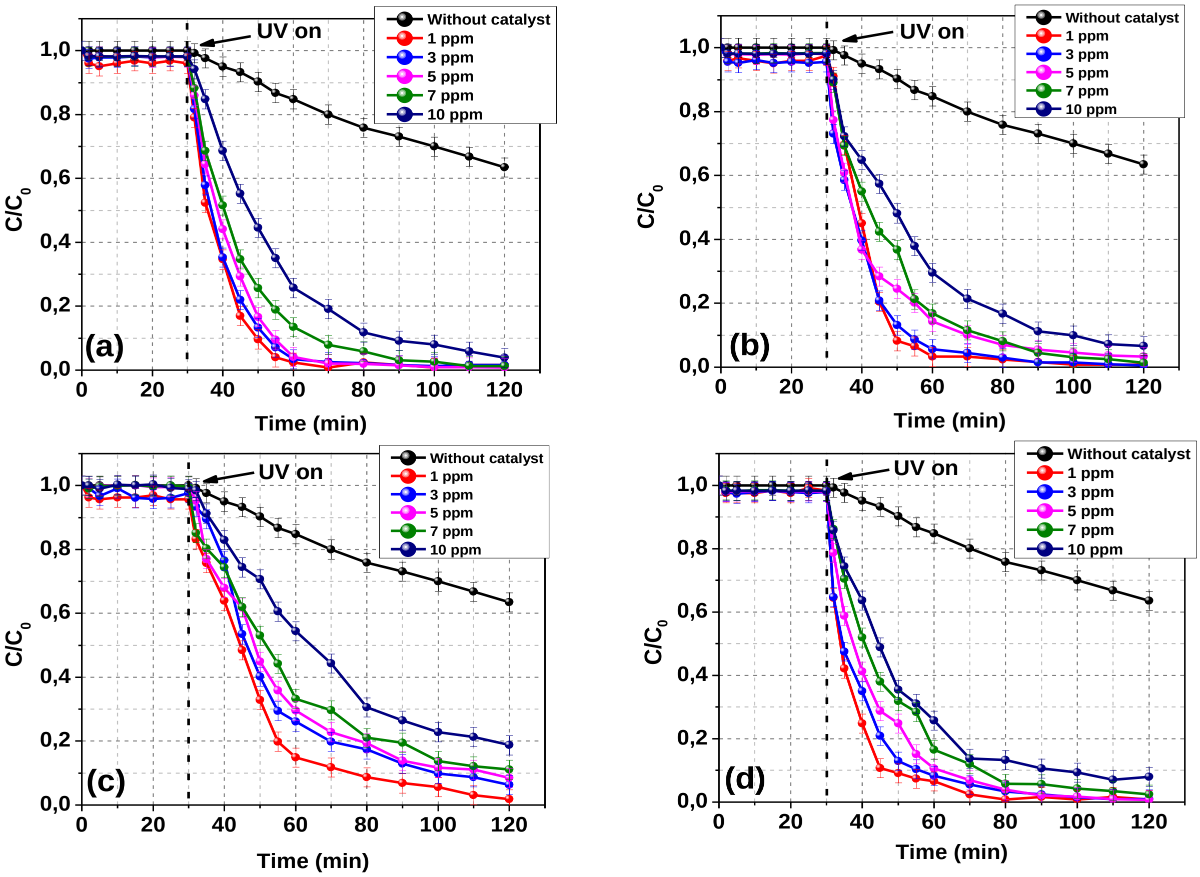

Figure III.8. Effect of initial concentration of Rhodamine on the photodegradation **(a)** TiO_2-400, **(b)** TiO_2-600, (**c**)TiO_2-800, (**d**) TiO_2-P25.

(Operational parameters: UV lamp: λ_{254nm}, intensity 4750 µW/cm², $[TiO_2]_0$ = 0.1 g/L, natural pH = 4.80).

Furthermore, the TiO_2-400 sample exhibits enhanced photocatalytic performance compared to TiO_2-P25. After 120 minutes of irradiation, TiO_2-400 maintains a stable photodegradation efficiency across initial Rhodamine B concentrations ranging from 1 to 7 ppm, with only a slight reduction observed at 10 ppm. In contrast, TiO_2-P25 exhibits a notably higher C/C_0 ratio at initial concentrations of 7 and 10 ppm, indicating a comparatively lower degradation efficiency under the same experimental conditions.

3.1.3. Effect of initial pH of the solution:

The pH of the medium plays a crucial role in the efficiency of the dye photodegradation process, as it influences the ionization state of the TiO_2 surface, dye adsorption and the generation of oxidation species [31]. In this study, the pH variations ranged from 1 to 12 for the suspension with a rhodamine B concentration of 10 ppm and a fixed amount (0.1 g/L) of TiO_2-400 nanocatalysts (Figure III.9). The pH was adjusted by adding appropriate amounts of NaOH or H_2SO_4 solution. The point of zero charge (pH_{pzc}) of TiO_2-400 is 6.3, as mentioned in Table III.1 The pKa of RhB is approximately 3.4 [32]. Rhodamine B degradation occurs via two mechanisms: N-deethylation, resulting in a blue shift in the absorption maximum, and structural disruption, leading to a gradual decrease in absorption intensity. Under acidic conditions, TiO_2 nanoparticles exhibit higher photodegradation efficiency (99.05%), which can be ascribed to the formation of hydrogen bonds between Rhodamine B molecules and the TiO_2 surface. This interaction facilitates charge transfer processes, thereby promoting N-deethylation and enhancing the overall photodegradation efficiency[33]. Furthermore, at low pH, the structure of the Rhodamine B dye shifts to an unstable quinoid form, which is more readily degraded, thereby enhancing the process efficiency [34]. In alkaline conditions, an attractive interaction exists between the N-ethyl group of RhB and the negatively charged surface of the catalyst. This interaction inhibits the N-deethylation process during photodegradation and reaches 74.50% at a pH value of 12 [21], [23].

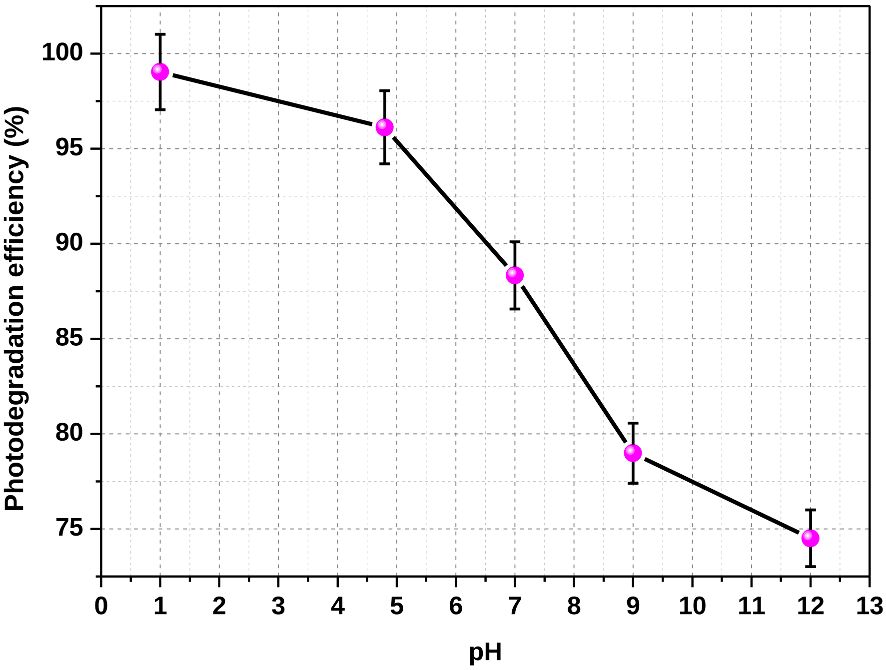

Figure III.9. Effect of pH solution on the photodegradation of Rhodamine B using the TiO_2-400 sample.
(Operational parameters: UV lamp: λ_{254nm}, intensity 4750 µW/cm², $[TiO_2]_0 = 0.1$ g/L, $[RhB]_0 = 10$ ppm, natural pH = 4.80).

3.1.4. Effect of irradiation source:

The impact of irradiation source (intensity and wavelength) on the photodegradation of Rhodamine B (RhB) with the TiO_2-400 sample was investigated using two distinct UV lamps: one emitting at 254 nm with an intensity of 5400 µW/cm², and the other at 365 nm with an intensity of 1280 µW/cm². The experiments were conducted under natural pH conditions using 0.1 g/L of TiO_2-400 photocatalyst and an initial RhB dye concentration of 10 ppm.

Figure III.10 illustrates the influence of wavelength and lamp intensity on RhB photodegradation. It is well established that TiO_2 generates electron–hole pairs when it absorbs radiation with energy greater than its band gap. For the TiO_2-400 sample, the band gap was 3.02 eV, as mentioned in Table III.. At 254 nm, the Photodegradation efficiency reached 36.48% for photolysis and 96.11% for photocatalysis, attributed to the higher photon energy that enhances hydroxyl radical generation and electron–hole pair formation, thereby improving the photodegradation process [30]. This result is consistent with section (3.1.2) observations, where TiO_2-400 demonstrated superior performance compared to TiO_2-P25 at an initial RhB dye concentration of 10 ppm under the same conditions. In comparison, photons at 365 nm induce limited photocatalytic activity for both photocatalysis and photolysis, due to insufficient energy for effective electron-hole pair generation [32], [33]. As reported by Mittal et al [9], [35], at low light intensities (0–20 mW/cm²), the photodegradation rate increases linearly with increasing light intensity, which explains the more efficient RhB discolouration observed under 254 nm compared to 365 nm irradiations.

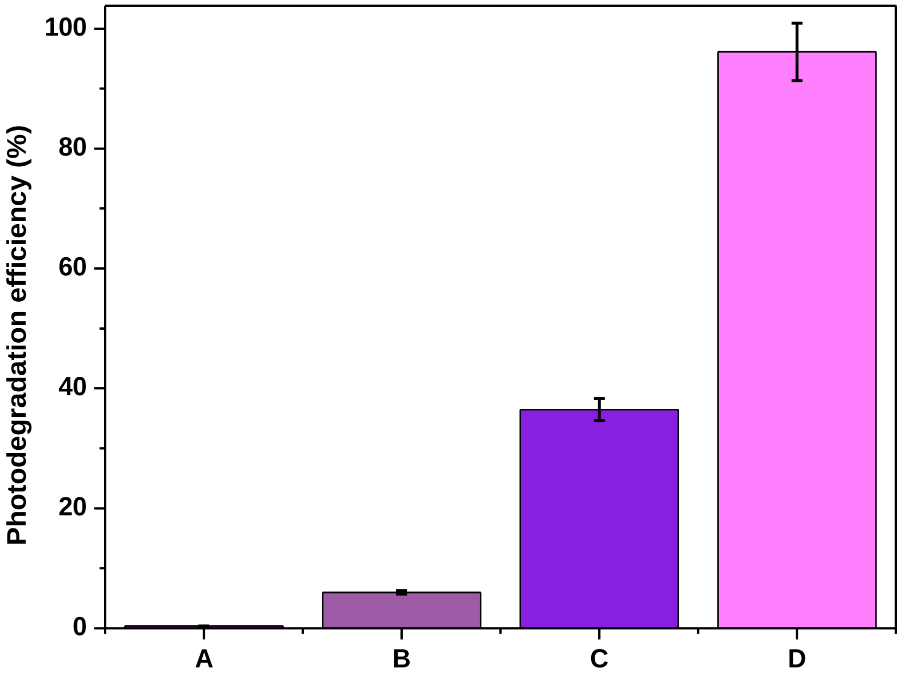

Figure III.10. Effect of Wavelength and intensity of lamps on photocatalytic degradation of RhB using TiO_2-400 sample. (A) Photolysis at 365 nm, (B) Photocatalysis at 365 nm, (c) Photolysis at 254 nm, (D) Photocatalysis at 254 nm

(Operational parameters: UV lamp: λ_{254nm}, intensity 4750 µW/cm², Irradiation time: 90 min, $[TiO_2]_0 = 0.1$ g/L, $[RhB]_0 = 10$ ppm, natural pH = 4.80).

3.2. Effect of calcination Temperature on Rhodamine B Photodegradation efficiency:

In this study, the calcination temperature is a critical factor, as its variation affects the photocatalytic performance of the TiO_2 material [29]. This factor influences phase composition, crystallinity, and surface characteristics, as shown in Table III.1. Figure III.11 illustrates the degradation efficiency of Rhodamine B using the TiO_2 photocatalyst calcined at different temperatures. Among all samples, TiO_2-400 exhibited the highest photodegradation efficiency, achieving nearly complete RhB degradation (96.11%). Several studies have indicated that 400°C is the optimal calcination temperature for the photodegradation of various organic pollutants [25], [26], [27]. The synergistic effect between the anatase and rutile phases in TiO_2 improves the photodegradation of Rhodamine B by facilitating charge separation and reducing electron-hole recombination [36]. However, the TiO_2-600 and TiO_2-800 samples exhibited a slight decrease in degradation efficiency, with rates of 93.37% and 81.25%, respectively, due to phase transitions and a reduced surface area, which hindered their photocatalytic performance. [37]. The TiO_2-P25 sample demonstrated a degradation rate of 92,07% compared to TiO_2-400, illustrating its potential as an effective photocatalyst. The photolysis experiment exhibited significantly lower degradation efficiency, highlighting the important role of a photocatalyst in achieving effective RhB degradation under UV irradiation.

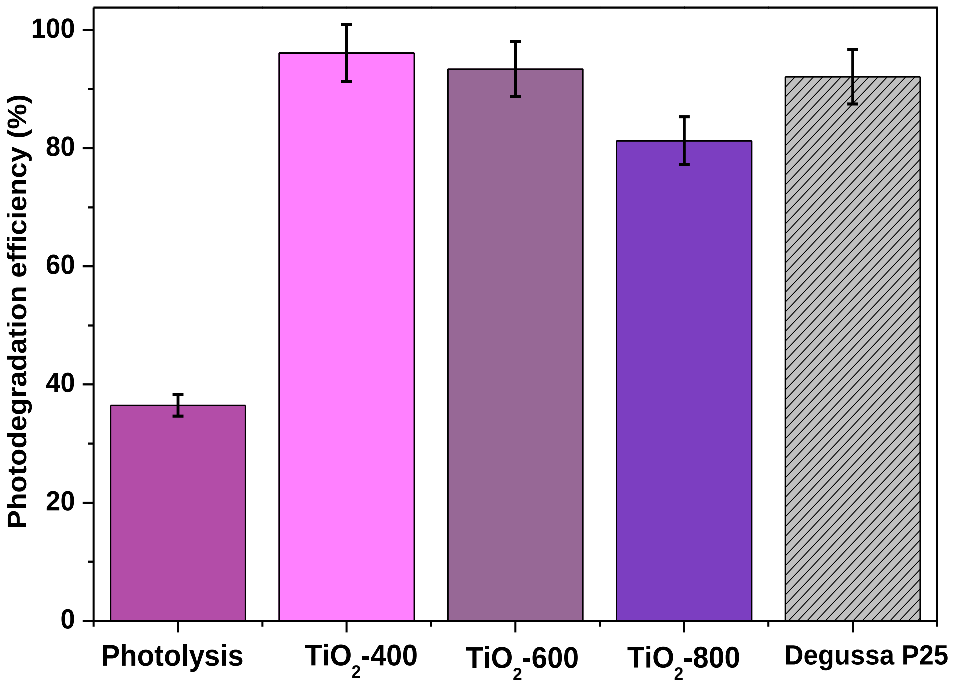

Figure III.11. Photodegradation efficiency of Rhodamine B using TiO_2 samples calcined at different temperatures compared to TiO_2-400 and photolysis.
(Operational parameters: UV lamp: λ_{254nm}, intensity 4750 µW/cm², $[TiO_2]_0 = 0.1$ g/L, $[RhB]_0 = 10$ ppm, natural pH = 4.80).

4. Photocatalytic Intensification: Comparative Analysis of Rhodamine B Degradation Efficiency

Several studies have investigated the influence of operational conditions and synthesis parameters on the photocatalytic performance of TiO_2 for the degradation of Rhodamine B. Among these parameters, increasing calcination temperature plays a crucial role, as it directly affects the physicochemical properties of TiO_2, including its crystalline structure, texture, and morphology. Table III.2 provides a comparative evaluation of Rhodamine B photodegradation efficiency using TiO_2 samples under different calcination temperatures and operational conditions. The findings highlight the importance of optimizing both calcination temperature and operational parameters to enhance the photocatalytic efficiency of TiO_2 for Rhodamine B degradation.

Table III.2. Comparative evaluation of Rhodamine B photodegradation efficiency using TiO_2 samples under different calcination temperatures and operational conditions

TiO_2 samples	Reaction conditions	Lamp	RhB Degradation (%)	Time irradiation (min)	Ref
TiO_2 calcined at 550	$[TiO_2]_0$= 0.3 $g.L^{-1}$ $[RhB]_0$=6 mg L^{-1} pH= 5	UV-lamp λ_{max}(nm) 280–100	99.8	75	[34]
TiO_2 calcined at 450	$[TiO_2]_0$= 1 g. L^{-1} $[RhB]_0$=5 mg. L^{-1} Natural pH	UV-lamp 125 W	100	270	[2]
Commercial Degussa P-25	$[TiO_2]_0$= 1.6 g. L^{-1} $[RhB]_0$=6.26×10^{-5} pH= 3.05	UV-LEDs 10–12 mW	96	180	[38]
TiO_2 without calcination	$[TiO_2]_0$= 0.1 g. L^{-1} $[RhB]_0$= 5 mg. L^{-1} Natural pH= 4.80	UVA lamp 12 W/m^2	81.5	180	[39]
TiO_2-400	$[TiO_2]_0$= 0.1 g. L^{-1} $[RhB]_0$= 10 mg. L^{-1} Natural pH= 4.80	UV lamp λ_{max}(254 nm) 1280 $\mu W/cm^2$	96,04	90	Current study
TiO_2-P25	$TiO_2]_0$= 0.1 g. L^{-1} $[RhB]_0$= 10 mg. L^{-1} Natural pH= 4.80	UV lamp λ_{max}(254 nm) 1280 $\mu W/cm^2$	92,07	90	Current study

5. Conclusion:

This study investigated the photocatalytic activity of titanium dioxide (TiO_2) as a photocatalyst for the degradation of RhB dye in aqueous solution under UV irradiation. TiO_2 material was synthesized using a non-conventional sol-gel method and calcined at various temperatures. The calcined samples were characterized through structural, morphological, textural, and optical analysis. Among the samples, TiO_2-400 can be classified as nanometric according to SEM analysis, whereas TiO_2-600 and TiO_2-800 exhibited larger particle sizes as a result of agglomeration and sintering effects. A correlation was established between the structural, morphological, textural, and optical properties of the synthesized TiO_2 materials and their photocatalytic performance, as investigated through operational parameters, highlighting the effect of increasing calcination temperature on the efficiency of Rhodamine B degradation under UV irradiation. The TiO_2-400 sample achieved the highest photodegradation efficiency (96.11%), followed by TiO_2-600 (93.37%), TiO_2-P25 (92.07%), and TiO_2-800 (81.25%). Compared to the benchmark TiO_2-P25, the TiO_2-400 sample exhibited not only higher overall photodegradation efficiency but also greater stability across varying initial RhB concentrations.

Part 2: Preparation of TiO_2-Bentonite composites via a non-conventional sol-gel route for the photodegradation of Rhodamine B

1. Introduction

The preceding section analyzed the photocatalytic efficiency of TiO_2 obtained by the sol–gel method, highlighting both its potential and its inherent limitations, particularly nanoparticle agglomeration and insufficient adsorption capacity. To address these constraints, TiO_2/bentonite composites were synthesized via a non-conventional sol-gel route. Bentonite, owing to its layered structure and high surface area, acts as a stabilizing support that promotes TiO_2 dispersion, enhances adsorption phenomena, and improves photocatalytic activity.

This section reports the structural and surface characterization of the composites (FTIR/ATR, XRD, BET, SEM/EDS, and pH_{pzc}). It systematically evaluates their performance in the photocatalytic degradation of Rhodamine B, considering the effects of dye concentration, catalyst loading, pH, irradiation source, and TiO_2 content.

2. Characterisation:

2.1. FTIR-ATR analysis:

Figure III.12 presents the FTIR-ATR spectra of Bentonite, TiO_2-400, and TiO_2/Bentonite composites containing 10%, 30%, and 50% TiO_2 in the spectral range of 400–4000 cm^{-1}. The spectrum of raw Bentonite displays several characteristic bands: a broad peak around 3618 cm^{-1} corresponding to the O–H stretching of structural hydroxyl groups, and a band at 1643 cm^{-1} assigned to the bending vibration of H–O–H from interlayer water molecules. In the lower wavenumber region, the peaks at 426.2 and 514.9 cm^{-1} are associated with Si–O–Si bending vibrations, while the band at 983.59 cm^{-1} corresponds to Si–O stretching vibrations of the tetrahedral silica structure [40]. The bands observed at approximately at 410.01 cm^{-1} (TiO_2-400), 420.25 cm^{-1} (10% TiO_2-BN), 418.39 cm^{-1} (30% TiO_2-BN), and 424.89 cm^{-1} (50%TiO_2-BN) are attributed to the Ti–O–Ti bridging stretching vibrations, indicating the presence of titanium oxide phases in TiO_2-BN composites [15], [41], Additionally, the peak at 1417 cm^{-1} for the raw bentonite attributed to carbonate impurities or surface-adsorbed species [42].

The presence and slight shifts in these bands in the TiO_2-BN composites suggest interactions between TiO_2 particles and the bentonite matrix, indicating successful incorporation and possible structural modifications upon composite formation.

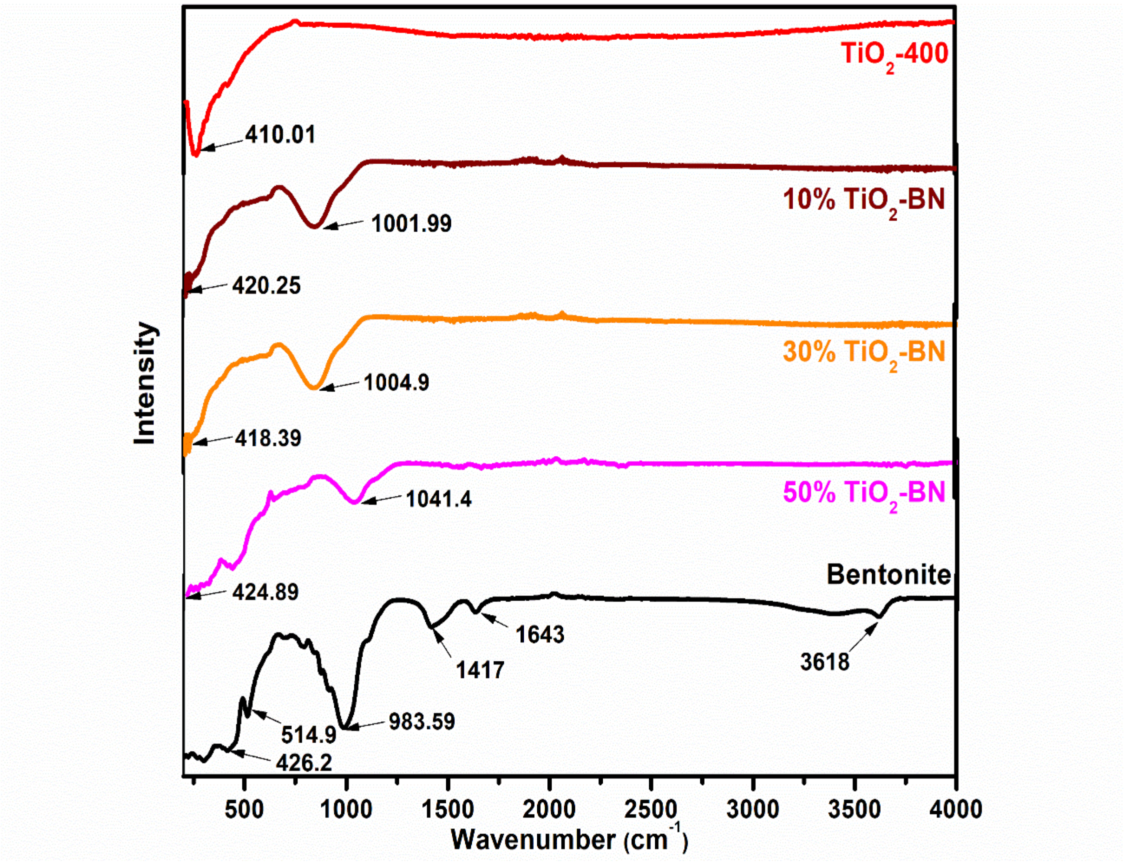

Figure III.12. FTIR-ATR analysis of bentonite and different synthesized samples.

2.2.XRD and BET analysis:

Figure III.13 displays the X-ray diffraction (XRD) patterns of pure Bentonite, TiO_2-400, and TiO_2-BN composites with 10%, 30%, and 50% TiO_2. The pattern of raw Bentonite shows the presence of montmorillonite at 19.77°, 26.60° and 61.89° [43], [44]. In the same context, TiO_2-400 exhibits sharp and intense peaks corresponding to the anatase phase of TiO_2, with reflections at 2θ= 25,35°, 37,78°, 48,07°, and 75,09°, assigned to the (101), (004), (200), and (215) planes, respectively. At the same time, the peaks at 2θ= 27,44°, 36,09°, 41.25°,54,33°, 62,78° and 69,02° (JCPDS card no. 21-1276) correspond to (110), (101), (111), (211), (002) and (301) planes of rutile. Upon TiO_2 incorporation, the diffraction peaks associated with the anatase phase are retained in all TiO_2-BN composites, and their intensities increase with higher TiO_2 content, indicating the successful deposition and preservation of crystalline TiO_2 within the clay matrix [45]. Notably, the characteristic peaks of Bentonite diminish in intensity as the TiO_2 loading increases, suggesting either partial coverage of the clay surface or structural changes resulting from TiO_2 interaction [45], [46].

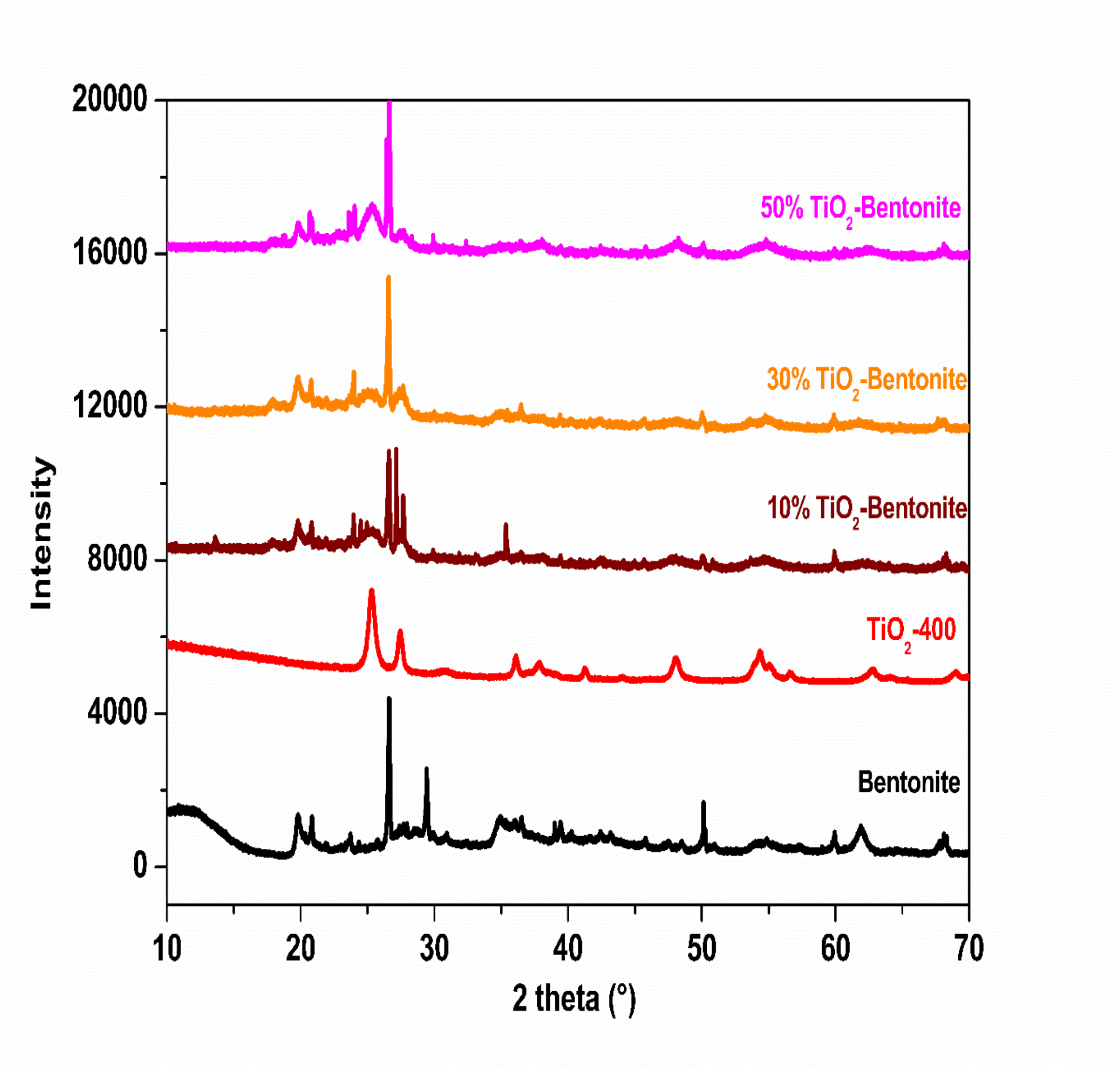

Figure III.13. XRD patterns of Bentonite, TiO_2-400 and TiO_2-BN samples.

Furthermore, the analysis of BET surface area indicates a clear pattern that corroborates the structural findings. Pure TiO_2 and raw bentonite exhibit surface areas of 62.83 m^2/g and 27.11 m^2/g, respectively. The 10%TiO_2-BN and 30% TiO_2-BN composites show surface areas of 58.44 m^2/g and 55.63 m^2/g, respectively, indicating moderate dispersion of TiO_2 nanoparticles without significant enhancement in textural properties compared with the 50%TiO_2-BN sample. However, a substantial increase in surface area is observed for the 50% TiO_2-BN composite, reaching 130.19 m^2/g. This remarkable enhancement reflects the evolution of a distinctly porous architecture characterised by enhanced interfacial interactions between TiO_2 and Bentonite, which can be attributed to the optimal distribution and possible exfoliation or delamination of clay layers throughout the synthesis process [40]. The combined XRD and BET results confirm the successful fabrication of TiO_2-BN heterostructures with improved crystallinity and surface characteristics at higher TiO_2 loadings.

Table III.3. BET surface area of Bentonite and different synthesized samples

Samples	**Surface area**
TiO_2	62.830
Bentonite	27.111
10% TiO_2-BN	58.441
30% TiO_2-BN	55.631
50% TiO_2-BN	130.188

2.3. SEM/EDS Analysis

The SEM and EDS analyses presented in Figure 3 provide critical insights into the morphological and elemental composition of TiO_2-BN composites: (a) Raw bentonite, (b) 10%TiO_2-BN, (c) 30%TiO_2-BN, and (d) 50%TiO_2-BN. The SEM micrograph of raw bentonite (a) reveals a smooth and layered surface morphology typical of clay minerals, characterized by compact, plate-like structures. As the TiO_2 content increases from 10% to 50% (b–d), a significant change in surface texture occurs; the composites display more irregular, porous, and rougher morphologies, indicating the progressive deposition of TiO_2 nanoparticles on the bentonite surface, which disrupts the original clay structure and introduces increased surface heterogeneity and potential active site. EDS spectra confirm the successful incorporation of TiO_2, evidenced by the emergence and intensification of Ti peaks alongside the existing signals for Si, Al, O, and minor elements such as Mg and Fe. The atomic and weight percentages of titanium increase proportionally with the TiO_2 loading (Table 1), confirming the compositional control achieved during the synthesis process. The enhanced oxygen signal is consistent with the progressive incorporation of TiO_2 into the composite structure. Furthermore, this elemental analysis illustrates a uniform spatial distribution of titanium, suggesting a homogeneous dispersion of TiO_2 nanoparticles within the bentonite matrix. This compositional and morphological evolution suggests that higher TiO_2 loadings enhance the surface complexity and potential photocatalytic activity of the materials, making them promising candidates for environmental remediation applications [47]

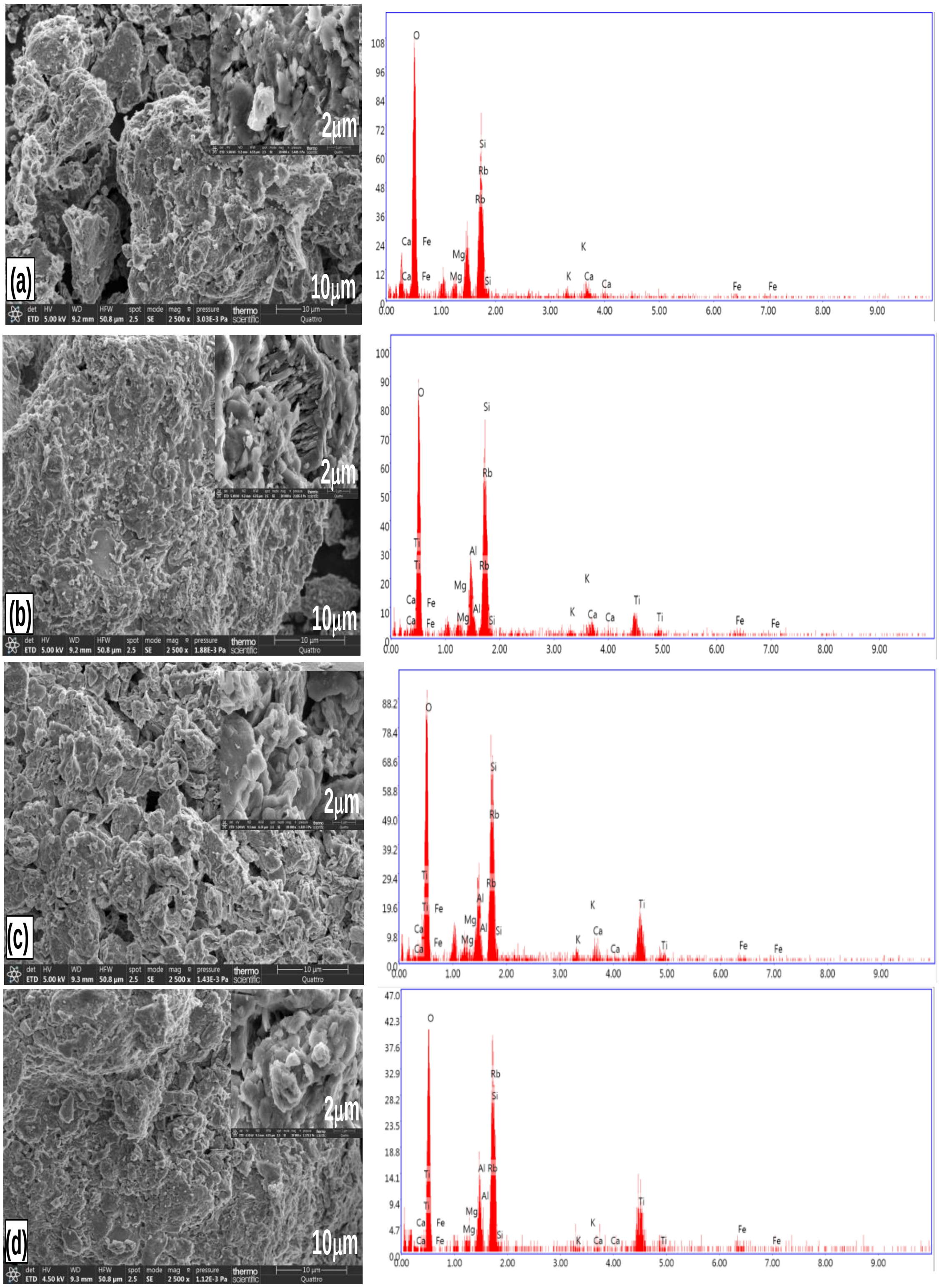

Figure III.14. SEM images and EDX spectra of (a) Bentonite, (b) 10% TiO_2-BN, (c) 30% TiO_2-BN, (d) 50% TiO_2-Bentonite

Table III.4. Elemental composition (Weight and Atomic %) of raw bentonite and TiO_2-BN composites at varying TiO_2 loadings, determined by EDS Analysis

Samples	**Raw bentonite**		**10%TiO_2-BN**		**30%TiO_2-BN**		**50%TiO_2-BN**	
Element	Weight (%)	Atomic (%)	Weight (%)	Atomic (%)	Weight (%)	Atomic (%)	Weight (%)	Atomic (%)
O	62.44	77.77	48.44	66.43	48.15	66.48	48.07	66.47
Mg	3.81	3.41	2.59	2.33	2.74	2.48	2.50	2.28
Al	5.41	7.10	8.87	7.21	8.04	6.58	8.89	7.29
Rb	16.58	5.60	3.15	0.81	2.03	0.53	5.59	1.45
Si	0.99	0.77	18.75	14.65	17.58	13.83	19.49	15.35
K	2.41	1.34	1.35	0.76	1.38	0.78	0.59	0.33
Ca	4.89	2.65	4.25	2.33	2.64	1.45	0.45	0.25
Fe	3.48	1.35	4.31	3.79	2.60	1.03	1.16	0.46
Ti	-	-	8.28	1.69	14.84	6.12	19.82	6.84

2.4.pH_{pzc} analysis

The pH at the point of zero charge (pH_{pzc}) indicates the pH level where the net surface charge of an adsorbent material is neutral. A comprehensive understanding of the point of zero charge (PZC) of bentonite–TiO_2 composites is crucial for the rational design and optimisation of their functional performance in various environmental applications, particularly in wastewater treatment systems, where they simultaneously serve as effective adsorbents and photocatalyst [44]. Figure III.15 illustrates the determination of the point of zero charge (pH_{pzc}) for bentonite, TiO_2, and the 50% TiO_2-BN composite. A quick and effective way to measure the pHpzc is the pH drift technique, as explained in the experimental procedures and characterisation section by [48]. For all materials, a positive ΔpH at low initial pH values (pH 2-6) shows the adsorption of H^+ ions from the solution, suggesting a negatively charged surface in this range. As the initial pH increases beyond roughly 6–7, ΔpH turns negative, indicating the release of protons and a shift to a positively charged surface. The pH_{pz}c is the point where ΔpH equals zero, which is about 6.8 for bentonite, 6.4 for the 50% TiO_2–BN composite, and 6.3 for TiO_2. These results show that TiO_2 has a more acidic surface compared to bentonite, while the 50% TiO_2–BN composite shows intermediate behaviour, reflecting the combined effects of both components. This change in surface charge due to TiO_2 addition could significantly influence adsorption and photocatalytic processes with ionic pollutants, especially in pH-sensitive environments, thereby improving the potential for environmental remediation using the composite.

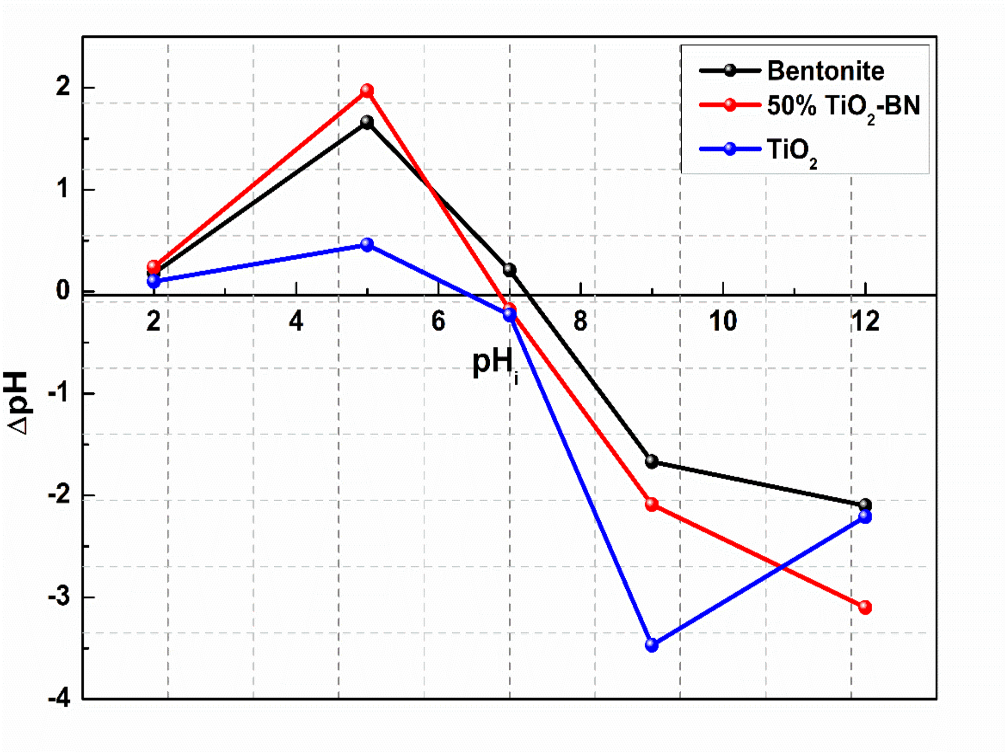

Figure III.15. Determination of the point of zero charge (pH_{pzc}) for Bentonite, TiO_2, and 50% TiO_2-Bentonite composites.

3. Evaluation of TiO_2, Bentonite, and UV Irradiation for Rhodamine B Degradation

Figure 5 shows a comparison of the photocatalytic degradation efficiency of Rhodamine B under UV light, using TiO_2 (0.1 g/L), bentonite (0.1 g/L), and their mixture at a 1:1 ratio. During the first 30 minutes in the dark, a notable adsorption of the dye onto the materials was observed, confirming minimal photocatalytic activity and emphasising the dominance of adsorption in this phase. When exposed to UV light, distinct differences in photocatalytic performance emerge among the tested systems. Bentonite, whether alone or under UV exposure, shows limited photocatalytic activity. This aligns with existing literature, which indicates that although natural clays have high surface areas and cation exchange capacities, they lack the electronic structure needed to produce reactive oxygen species upon irradiation [49]. Conversely, TiO_2 calcined at 400 °C (TiO_2-400) exhibits notable photocatalytic activity, due to its anatase-dominant crystalline form and sufficient surface area, both of which support effective charge carrier generation and dye degradation[8]. Degussa P-25, a commercial benchmark photocatalyst consisting of mixed anatase and rutile phases, surpasses TiO_2-400, which supports earlier findings that highlight the improved charge separation and higher reactivity of mixed-phase TiO_2 systems.

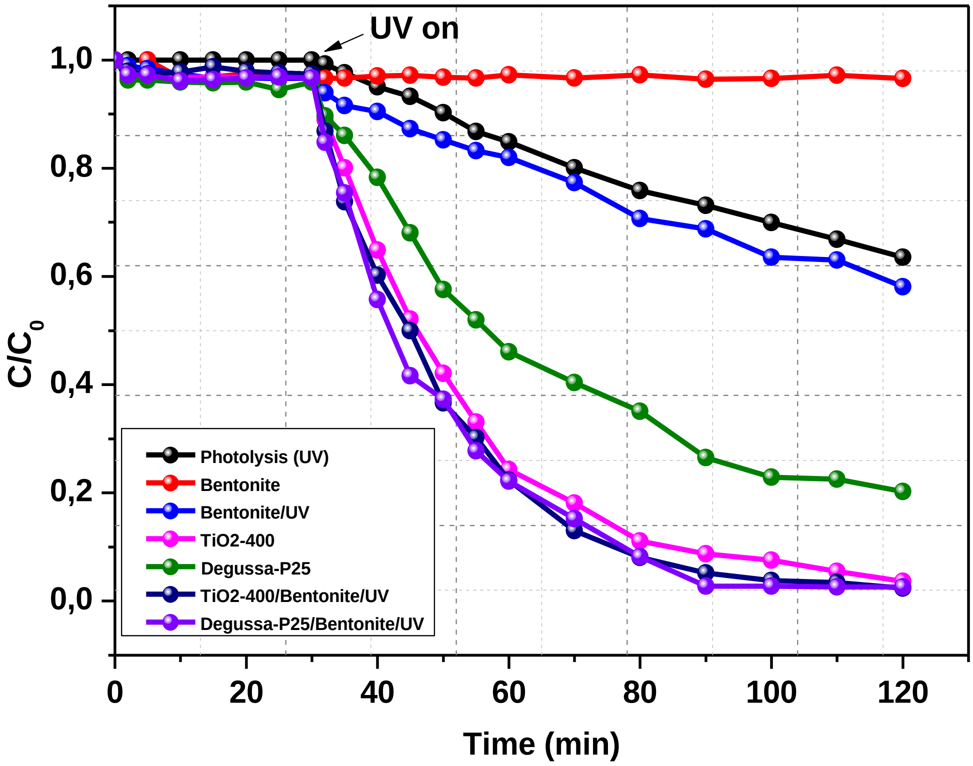

Figure III.16. Photocatalytic degradation of Rhodamine B under UV irradiation using Bentonite, TiO_2, and Degussa p-25.

The high degradation efficiency observed with the physical mixture of TiO_2 and bentonite in suspension under UV irradiation can be ascribed to a cooperative mechanism between the photocatalytic properties of TiO_2 and the physicochemical characteristics of bentonite. TiO_2, as the photoactive component, generates electron-hole pairs upon UV exposure, leading to the formation of reactive oxygen species responsible for dye oxidation. Although bentonite is not photocatalytically active, its high surface area and adsorption capacity facilitate the enrichment of dye molecules near TiO_2 particles, thereby enhancing their interaction with the reactive species generated. Furthermore, bentonite contributes to the improved dispersion of TiO_2 in aqueous media, minimizing particle aggregation and promoting greater light penetration and access to active sites. While no chemical bonding or structural integration exists between TiO_2 and bentonite in this physical mixture, their combination in suspension yields a modest yet meaningful synergistic effect, resulting in improved photocatalytic performance compared to the individual components. These findings highlight the importance of integrating the active phase into a supporting matrix through controlled synthesis strategies to achieve optimal and sustained photocatalytic efficiency.

4. Evaluation of photocatalytic performance of TiO_2-BN composites:

This section evaluates the photocatalytic performance of TiO_2–Bentonite (TiO_2–BN) composites through the degradation of Rhodamine B (RhB) under various experimental conditions. Key parameters influencing the efficiency of the photocatalytic process are systematically investigated, including the initial dye concentration, photocatalyst loading, solution pH, and irradiation source. Furthermore, the effect of TiO_2 content on the photodegradation rate of Rhodamine B was investigated to determine the optimal composition for enhanced photocatalytic efficiency.

4.1. Effect of photocatalyst loading:

The graphs (a), (b), and (c) in Figure III.17 illustrate the photocatalytic degradation of Rhodamine B using TiO_2–BN composites at varying catalyst loadings of 30 mg, 50 mg, 70 mg, and 100 mg under UV irradiation.

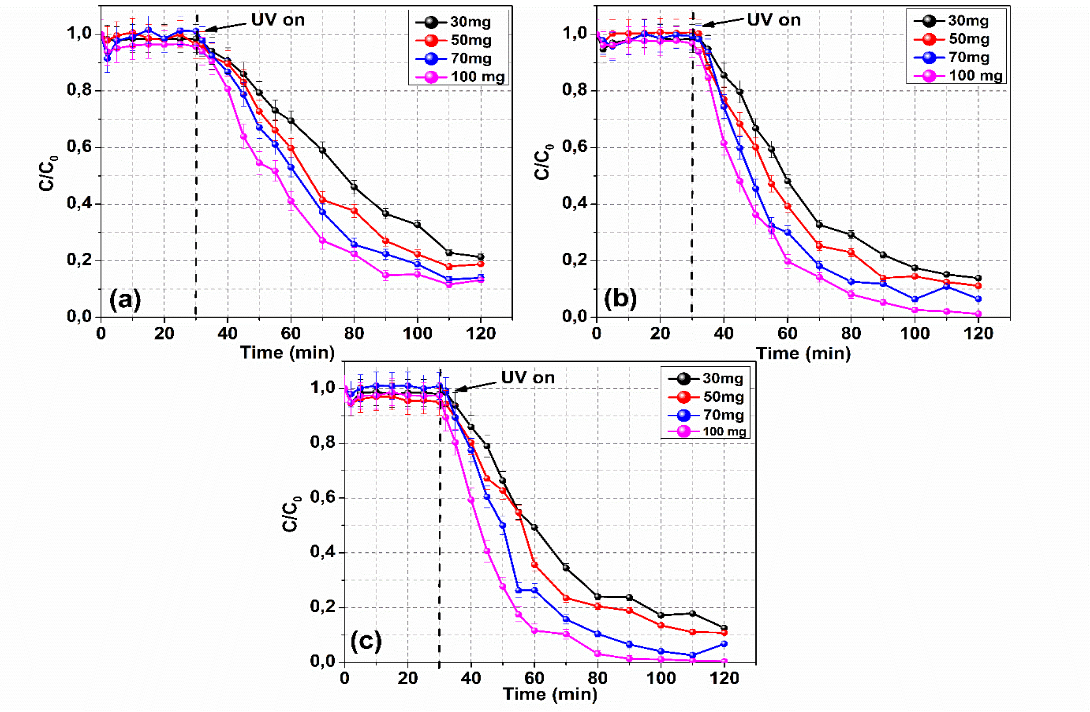

Figure III.17. Effect of TiO_2-BN catalyst loading on the photodegradation of Rhodamine B under UV Irradiation.

The highest degradation efficiency is consistently observed with the 100 mg loading, followed by 70 mg, 50 mg, and 30 mg. This trend can be attributed to the increased availability of active sites and enhanced photon absorption at higher catalyst dosages, which promote the generation of reactive species responsible for dye degradation [50]. However, the data also indicate diminishing returns beyond a certain threshold, particularly between 70 mg and 100 mg, suggesting that excessive catalyst amounts may lead to particle agglomeration or increased light scattering, thereby reducing photocatalytic efficiency [51], [52]

4.2. Effect of the initial dye concentration of rhodamine B:

The three plots (Figure III.18) illustrate the photocatalytic degradation profiles of Rhodamine B (RhB) at varying initial concentrations (1–10 ppm), using TiO_2-BN composites under UV irradiation. In each graph, the UV lamp was activated after 30 minutes of equilibrium adsorption-desorption. As the initial dye concentration increases, the degradation rate decreases, with lower concentrations (1–5 ppm) exhibiting more rapid and complete photodegradation compared to higher concentrations (7 and 10 ppm). This trend is attributed to the greater light penetration and availability of active sites at lower dye concentrations [53].

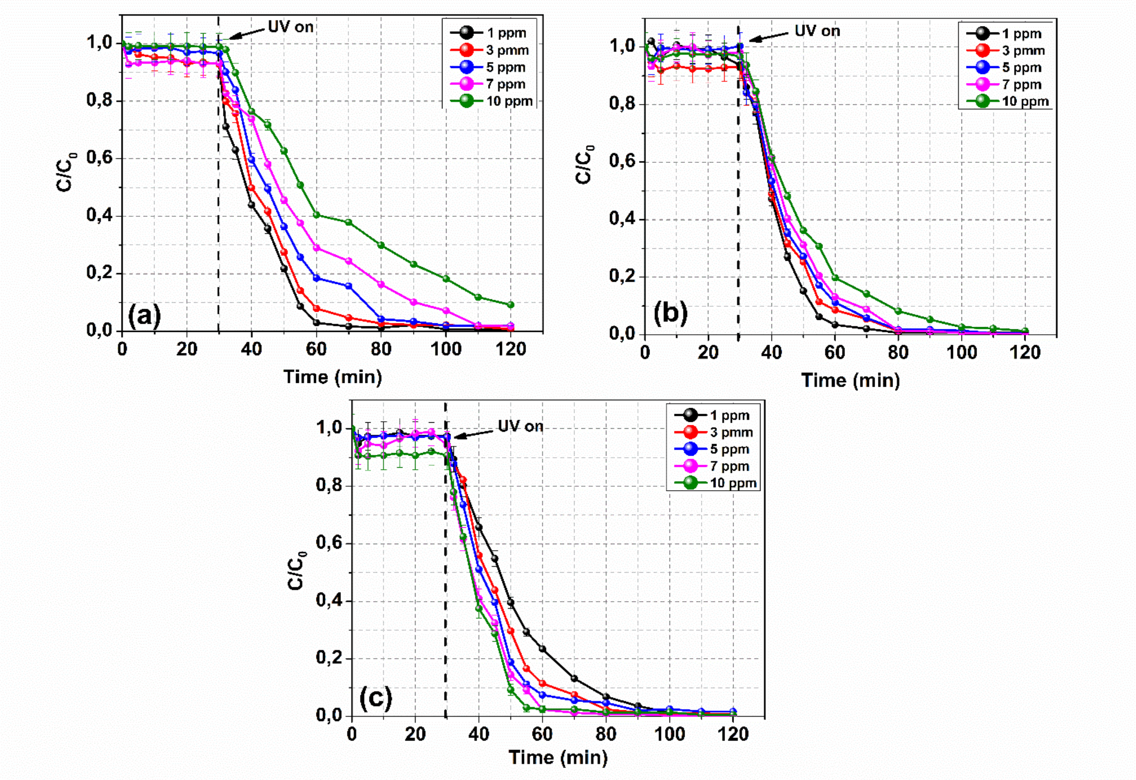

Figure III.18. Effect of initial Rhodamine B concentration on photodegradation efficiency using TiO_2-BN composites under UV Irradiation

Conversely, at higher concentrations, excess dye may shield the catalyst surface, limiting light absorption and thereby reducing photocatalytic efficiency [54]. The similarity in degradation trends across the three plots suggests consistent behaviour of the composites, while slight variations may reflect differences in catalyst composition or experimental conditions.

4.3. Effect of pH solution

Figure III.19 illustrates the effect of pH solution on the photodegradation efficiency of Rhodamine B when using a 50% TiO_2–BN composite under UV irradiation. The degradation efficiency remains very high at acidic to near-neutral pH values (pH 1–6), indicating that the photocatalytic activity is most effective within this range. This can be attributed to the positive surface charge of the photocatalyst at pH values below its point of zero charge pH_{pzc}, which enhances electrostatic attraction with dye molecules. When the pH increases beyond 6, especially within the range of pH 7 to 12, the degradation efficiency gradually decreases, reaching around 79% at pH 12. The decline can be explained by a change in the surface charge of the photocatalyst, which becomes negative at higher pH values, causing repulsive interactions with the dye molecules and reducing their adsorption [55].

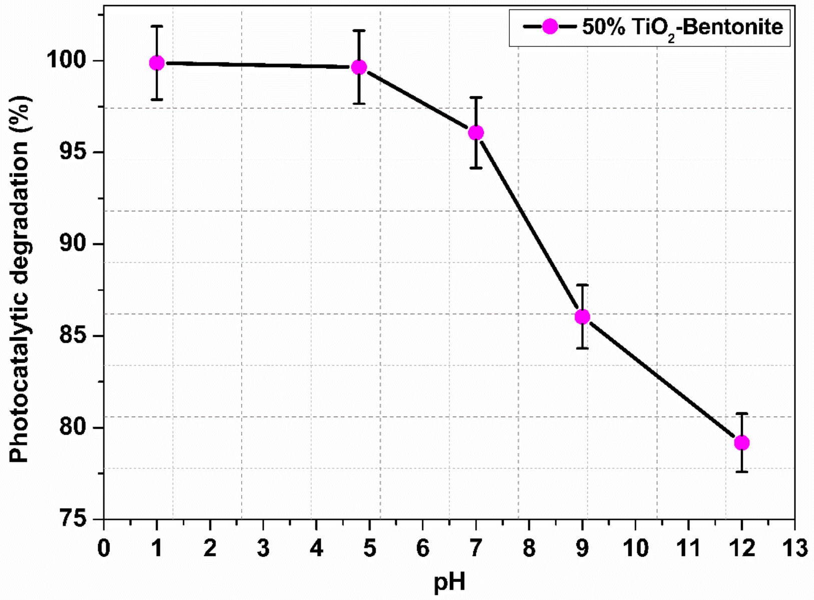

Figure III.19. Effect of pH solution on the photodegradation efficiency of Rhodamine B, using 50% TiO_2-BN.

Furthermore, in highly alkaline conditions, the presence of excess hydroxide ions (OH^-) may act as scavengers for photogenerated holes, thus inhibiting the formation of reactive oxidative species necessary for efficient dye degradation [56]. Given these observations, a neutral pH was selected for subsequent experiments. The choice of neutral pH offers a compromise between maintaining high photocatalytic efficiency and ensuring practical feasibility, as it reflects typical environmental and wastewater conditions where significant pH modification is often neither practical nor economical. Additionally, using near-neutral conditions reduces the likelihood of unwanted reactions and maintains the stability of the catalyst and dye, thereby enhancing the reliability and repeatability of the results.

4.4. Effect of irradiation source:

Figure III.20 illustrates the photodegradation efficiency of Rhodamine B using the 50% TiO_2-BN sample under two different UV irradiation sources. The observed variation in degradation efficiency can be attributed to the photon energy associated with each wavelength. Additionally, the structural and adsorptive properties of bentonite play a crucial role in enhancing the performance of the 50% TiO_2-BN composite [57]. This synergistic effect accounts for the nearly complete degradation of Rhodamine B observed under 254 nm irradiation in the presence of the composite (99.64%) , as the high-energy UV light enables efficient charge carrier generation and promotes the formation of reactive oxygen species (ROS). As reported by Livy Laysandra et al [40], the incorporation of bentonite into TiO_2 systems induces a synergistic interaction that significantly enhances photocatalytic activity. In contrast, irradiation at 365 nm provides photon energy only slightly above the TiO_2 band gap, resulting in markedly lower degradation efficiency (17.98%), even in the presence of the catalyst. This reduction is likely due to less efficient light absorption and a weaker generation of charge carriers. Moreover, the limited degradation observed under at 365 nm (0.37%) and 254 nm (47.51%) in the absence of the catalyst suggests that, although UV-C light possesses sufficient energy to induce partial dye degradation, the presence of a photocatalyst is essential to achieve efficient degradation. The bentonite also contributes to performance enhancement by preventing TiO_2 nanoparticle aggregation, improving dispersion, and maximizing the exposure of active sites under UV irradiation [58].

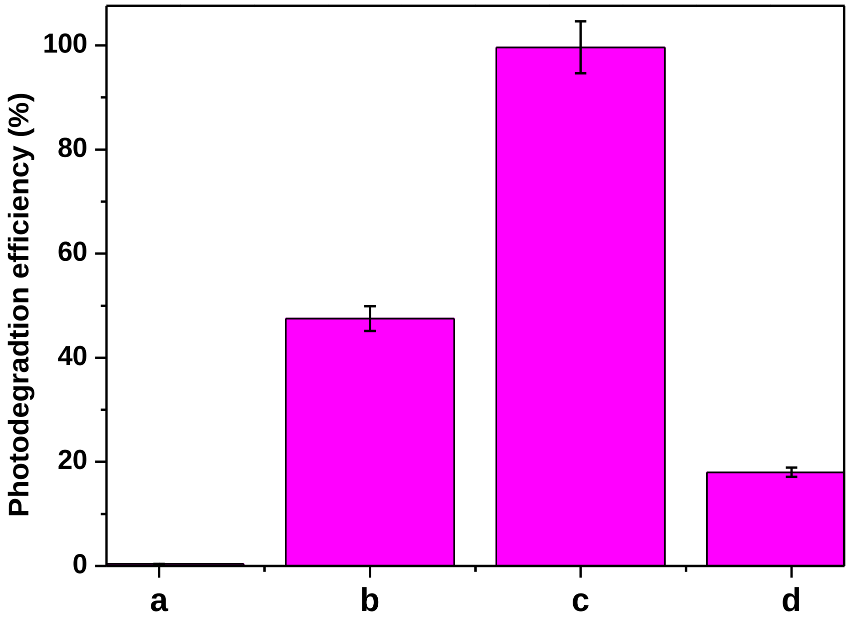

Figure III.20. Effect of the irradiation source on the Rhodamine B photodegradation efficiency using 50% TiO_2-BN
(a) Photolysis at 365 nm, (b) Photolysis at 254 nm, (c) 50% TiO_2-BN (Photocatalysis 254 nm), (d) 50% TiO_2-BN (Photocatalysis 365 nm)

4.5. Effect of the contents of TiO_2:

Figure III.21 illustrates the relationship between TiO_2 content and the photocatalytic degradation efficiency of Rhodamine B for TiO_2–BN composites under UV irradiation. A notable increase in degradation efficiency is observed as the TiO_2 content rises from 10% to 50%. At the lower loading of 10% TiO_2, the composite displays moderate efficiency (86.76%), likely due to the limited availability of photocatalytic active sites for light absorption and the generation of reactive oxygen species (ROS) [55]. Upon increasing the TiO_2 content to 30%, the degradation efficiency markedly improves, reaching approximately 99%, indicating a significant enhancement in photocatalytic activity. This improvement is attributed to the higher concentration of TiO_2 nanoparticles (as confirmed by EDX analysis), which facilitates greater photon absorption and promotes the generation of electron-hole pairs [59].

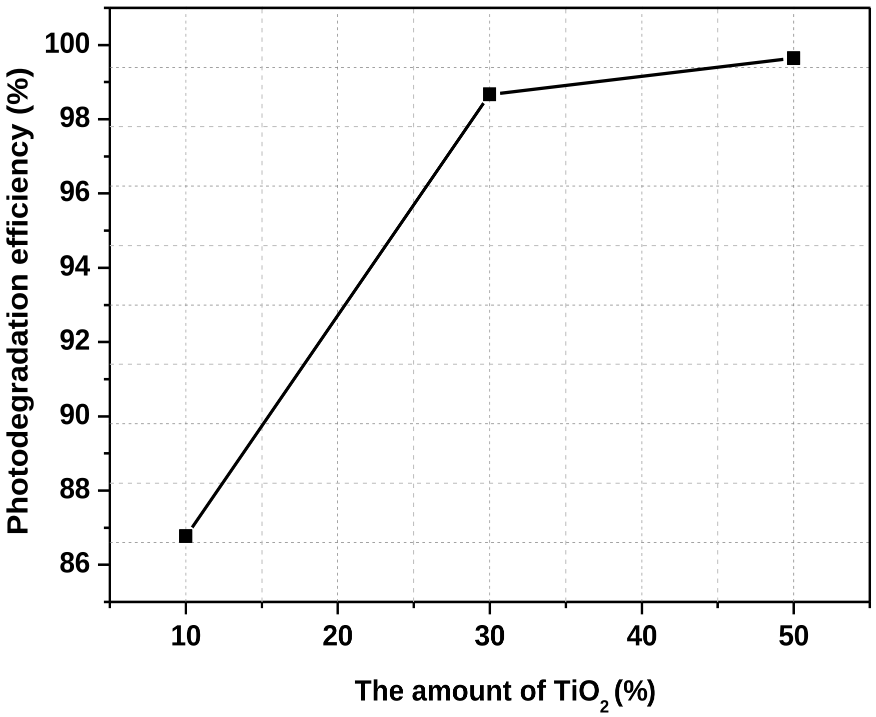

Figure III.21. Effect of TiO_2 content on the photodegradation efficiency of Rhodamine B using a 50% TiO_2- BN composite.

The marginal gain observed at 50% TiO_2 suggests that this composition represents an optimal balance between photocatalyst quantity and its uniform dispersion within the bentonite matrix. Bentonite plays a crucial role in preventing TiO_2 nanoparticle agglomeration, maintaining a high surface area, and thereby enhancing the accessibility of active sites and promoting the adsorption of dye molecules [60], [61]. The observed synergistic interaction between TiO_2 and bentonite is consistent with previous studies that highlight the improved photocatalytic efficiency in hybrid systems, attributed to enhanced charge separation, increased surface adsorption, and better light utilization [62]. Overall, these findings confirm that increasing the TiO_2 content within the composite significantly boosts the degradation efficiency of Rhodamine B, with the 50% TiO_2-BN sample demonstrating the most effective performance under UV irradiation.

5. Conclusion

This chapter has presented a comprehensive investigation into the synthesis, characterization, and photocatalytic evaluation of TiO_2/Bentonite composites prepared via a non-conventional sol–gel method for the degradation of Rhodamine B. The physicochemical analyses (FTIR-ATR, XRD, BET, SEM/EDS, and pHpzc) confirmed the successful incorporation of TiO_2 onto the bentonite matrix and revealed significant modifications in surface area, morphology, and surface charge properties, which are critical for photocatalytic applications.The control study underlined the individual and synergistic roles of TiO_2, bentonite, and UV irradiation, demonstrating that the combined system significantly enhances photodegradation efficiency. The photocatalytic performance of the TiO_2/Bentonite composites was then systematically evaluated under various operational parameters. Results showed that the degradation efficiency is strongly influenced by the initial dye concentration, catalyst dosage, solution pH, light source, and TiO_2/Bentonite ratio. Notably, the composite with 50% TiO_2 exhibited superior photocatalytic activity under UV light, highlighting the importance of optimizing the composition for enhanced performance. Overall, the findings of this chapter support the effectiveness of TiO_2/Bentonite composites as promising heterogeneous photocatalysts for environmental remediation, particularly in the treatment of dye-contaminated wastewater. This study also reinforces the relevance of material design and operational parameter optimization in developing sustainable and efficient advanced oxidation processes.

References:

[1] L. A. Rocha *et al.*, “Europium incorporated into titanium oxide by the sol-gel method,” *Mat. Res.*, vol. 8, no. 3, pp. 361–364, Sep. 2005, doi: 10.1590/S1516-14392005000300024.

[2] M. M. Mahlambi, A. K. Mishra, S. B. Mishra, R. W. Krause, B. B. Mamba, and A. M. Raichur, “Comparison of rhodamine B degradation under UV irradiation by two phases of titania nano-photocatalyst,” *J Therm Anal Calorim*, vol. 110, no. 2, pp. 847–855, Nov. 2012, doi: 10.1007/s10973-011-1852-7.

[3] J. Pagáčová *et al.*, “Crystallization of TiO2 xerogel,” *J Therm Anal Calorim*, vol. 142, no. 5, pp. 1643–1648, Dec. 2020, doi: 10.1007/s10973-020-09682-z.

[4] S. Mustapha *et al.*, “Facile synthesis and characterization of TiO2 nanoparticles: X-ray peak profile analysis using Williamson–Hall and Debye–Scherrer methods,” *Int Nano Lett*, vol. 11, no. 3, pp. 241–261, Sep. 2021, doi: 10.1007/s40089-021-00338-w.

[5] R. A. Spurr and Howard. Myers, “Quantitative Analysis of Anatase-Rutile Mixtures with an X-Ray Diffractometer,” *Anal. Chem.*, vol. 29, no. 5, pp. 760–762, May 1957, doi: 10.1021/ac60125a006.

[6] S. Saalinraj and K. C. Ajithprasad, “Effect of Calcination Temperature on Non-linear Absorption Co-efficient of Nano Sized Titanium Dioxide (TiO 2) Synthesised by Sol-Gel Method,” *Materials Today: Proceedings*, vol. 4, no. 2, pp. 4372–4379, 2017, doi: 10.1016/j.matpr.2017.04.008.

[7] N. Wetchakun, B. Incessungvorn, K. Wetchakun, and S. Phanichphant, “Influence of calcination temperature on anatase to rutile phase transformation in TiO2 nanoparticles synthesized by the modified sol–gel method,” *Materials Letters*, vol. 82, pp. 195–198, Sep. 2012, doi: 10.1016/j.matlet.2012.05.092.

[8] N. S. Allen, N. Mahdjoub, V. Vishnyakov, P. J. Kelly, and R. J. Kriek, “The effect of crystalline phase (anatase, brookite and rutile) and size on the photocatalytic activity of calcined polymorphic titanium dioxide (TiO 2),” *Polymer Degradation and Stability*, vol. 150, pp. 31–36, Apr. 2018, doi: 10.1016/j.polymdegradstab.2018.02.008.

[9] C. Hayet, “Degradation of Orange G by UV/TiO2/IO4 ¯process: Effect of operational parameters and estimation of electrical energy consumption,” *Indian J Chem Technol*, 2023, doi: 10.56042/ijct.v30i3.62814.

[10] Md. Rashid Al-Mamun, K. T. Hossain, S. Mondal, Most. Afroza Khatun, Md. Shahinoor Islam, and Dr. Md. Zaved Hossain Khan, “Synthesis, characterization, and photocatalytic performance of methyl orange in aqueous TiO2 suspension under UV and solar light irradiation,” *South African Journal of Chemical Engineering*, vol. 40, pp. 113–125, Apr. 2022, doi: 10.1016/j.sajce.2022.02.002.

[11] M. K. Singh and M. S. Mehata, “Phase-dependent optical and photocatalytic performance of synthesized titanium dioxide (TiO2) nanoparticles,” *Optik*, vol. 193, p. 163011, Sep. 2019, doi: 10.1016/j.ijleo.2019.163011.

[12] V. T. Lukong, K. O. Ukoba, and T. C. Jen, “Heat-assisted sol–gel synthesis of tio2 nanoparticles structural, morphological and optical analysis for self-cleaning application,” *Journal of King Saud University - Science*, vol. 34, no. 1, p. 101746, Jan. 2022, doi: 10.1016/j.jksus.2021.101746.

[13] M. S. Johnson, M. Ates, Z. Arslan, I. O. Farah, and C. Bogatu, “Assessment of Crystal Morphology on Uptake, Particle Dissolution, and Toxicity of Nanoscale Titanium Dioxide on Artemia Salina,” *Journal of Nanotoxicology and Nanomedicine*, vol. 2, no. 1, pp. 11–27, Jan. 2017, doi: 10.4018/jnn.2017010102.

[14] Y. Aristanti, Y. I. Supriyatna, N. P. Masduki, and S. Soepriyanto, “Effect of calcination temperature on the characteristics of TiO_2 synthesized from ilmenite and its applications

for photocatalysis," *IOP Conf. Ser.: Mater. Sci. Eng.*, vol. 478, p. 012019, Feb. 2019, doi: 10.1088/1757-899x/478/1/012019.

[15] L. Tesfaye Jule, K. Ramaswamy, B. Bekele, A. Saka, and N. Nagaprasad, "Experimental investigation on the impacts of annealing temperatures on titanium dioxide nanoparticles structure, size and optical properties synthesized through sol-gel methods," *Materials Today: Proceedings*, vol. 45, pp. 5752–5758, 2021, doi: 10.1016/j.matpr.2021.02.586.

[16] J. Li, Y. Ye, L. Shen, J. Chen, and H. Zhou, "Densification and grain growth during pressureless sintering of TiO2 nanoceramics," *Materials Science and Engineering: A*, vol. 390, no. 1–2, pp. 265–270, Jan. 2005, doi: 10.1016/j.msea.2004.08.025.

[17] S. Mahshid, M. Askari, M. Sasani Ghamsari, N. Afshar, and S. Lahuti, "Mixed-phase TiO2 nanoparticles preparation using sol–gel method," *Journal of Alloys and Compounds*, vol. 478, no. 1–2, pp. 586–589, Jun. 2009, doi: 10.1016/j.jallcom.2008.11.094.

[18] F. Pellegrino *et al.*, "Influence of agglomeration and aggregation on the photocatalytic activity of TiO 2 nanoparticles," *Applied Catalysis B: Environmental*, vol. 216, pp. 80–87, Nov. 2017, doi: 10.1016/j.apcatb.2017.05.046.

[19] C. Su, "Sol–gel preparation and photocatalysis of titanium dioxide," *Catalysis Today*, 2004.

[20] H. Hahn, J. Logas, and R. S. Averback, "Sintering characteristics of nanocrystalline TiO_2," *J. Mater. Res.*, vol. 5, no. 3, pp. 609–614, Mar. 1990, doi: 10.1557/jmr.1990.0609.

[21] N. C. Horti, M. D. Kamatagi, N. R. Patil, S. K. Nataraj, M. S. Sannaikar, and S. R. Inamdar, "Synthesis and photoluminescence properties of titanium oxide (TiO2) nanoparticles: Effect of calcination temperature," *Optik*, vol. 194, p. 163070, Oct. 2019, doi: 10.1016/j.ijleo.2019.163070.

[22] J. Zhang *et al.*, "Photocatalytic Degradation of Rhodamine B on Anatase, Rutile, and Brookite TiO2," *Chinese Journal of Catalysis*, vol. 32, no. 6–8, pp. 983–991, Jan. 2011, doi: 10.1016/S1872-2067(10)60222-7.

[23] E. A. Al-Maliky, H. A. Gzar, and M. G. Al-Azawy, "Determination of Point of Zero Charge (PZC) of Concrete Particles Adsorbents," *IOP Conf. Ser.: Mater. Sci. Eng.*, vol. 1184, no. 1, p. 012004, Sep. 2021, doi: 10.1088/1757-899x/1184/1/012004.

[24] M. Kosmulski, "The significance of the difference in the point of zero charge between rutile and anatase," *Advances in Colloid and Interface Science*, vol. 99, no. 3, pp. 255–264, Dec. 2002, doi: 10.1016/s0001-8686(02)00080-5.

[25] P. Górska *et al.*, "TiO2 photoactivity in vis and UV light: The influence of calcination temperature and surface properties," *Applied Catalysis B: Environmental*, vol. 84, no. 3–4, pp. 440–447, Dec. 2008, doi: 10.1016/j.apcatb.2008.04.028.

[26] L. M. Bertus and R. A. Carcel, "PREDICTION OF TiO2 AND WO3 NANOPOWDERS SURFACE CHARGE BY THE EVALUATION OF POINT OF ZERO CHARGE (PZC)," *Environ. Eng. Manag. J.*, vol. 10, no. 8, pp. 1021–1026, 2011, doi: 10.30638/eemj.2011.148.

[27] G. Žerjav, K. Žižek, J. Zavašnik, and A. Pintar, "Brookite vs. rutile vs. anatase: What`s behind their various photocatalytic activities?," *Journal of Environmental Chemical Engineering*, vol. 10, no. 3, p. 107722, Jun. 2022, doi: 10.1016/j.jece.2022.107722.

[28] N. Us, "Impact of Silver Ions Doping and Calcination on the Physicochemical Characteristics of TiO2 Nanoparticles with Photocatalytic and Regeneration Potential," *Iran. J. Chem. Chem. Eng.*, vol. 40, no. 4, 2021.

[29] U. G. Akpan and B. H. Hameed, "Parameters affecting the photocatalytic degradation of dyes using TiO2-based photocatalysts: A review," *Journal of Hazardous Materials*, vol. 170, no. 2–3, pp. 520–529, Oct. 2009, doi: 10.1016/j.jhazmat.2009.05.039.

[30] I. Groeneveld, M. Kanelli, F. Ariese, and M. R. Van Bommel, "Parameters that affect the photodegradation of dyes and pigments in solution and on substrate – An overview," *Dyes and Pigments*, vol. 210, p. 110999, Feb. 2023, doi: 10.1016/j.dyepig.2022.110999.

[31] S. N. Tan, M. L. Yuen, and R. A. Ramli, "Photocatalysis of dyes: Operational parameters, mechanisms, and degradation pathway," *Green Analytical Chemistry*, vol. 12, p. 100230, Mar. 2025, doi: 10.1016/j.greeac.2025.100230.

[32] A. O. Adeola, "Rhodamine B sequestration using acid-precipitated and microwave-treated softwood lignin: Comparative isotherm, kinetics and thermodynamic studies," *Environmental Technology*, 2023.

[33] K. Yu, S. Yang, H. He, C. Sun, C. Gu, and Y. Ju, "Visible Light-Driven Photocatalytic Degradation of Rhodamine B over $NaBiO_3$: Pathways and Mechanism," *J. Phys. Chem. A*, vol. 113, no. 37, pp. 10024–10032, Sep. 2009, doi: 10.1021/jp905173e.

[34] F. I. El-Dossoki, T. M. Atwee, A. M. Hamada, and A. A. El-Bindary, "Photocatalytic degradation of Remazol Red B and Rhodamine B dyes using TiO2 nanomaterial: estimation of the effective operating parameters," *Desalination and Water Treatment*, vol. 233, pp. 319–330, Sep. 2021, doi: 10.5004/dwt.2021.27519.

[35] K. M. Reza, A. Kurny, and F. Gulshan, "Parameters affecting the photocatalytic degradation of dyes using TiO2: a review," *Appl Water Sci*, vol. 7, no. 4, pp. 1569–1578, Jul. 2017, doi: 10.1007/s13201-015-0367-y.

[36] L. Shi and D. Weng, "Highly active mixed-phase TiO2 photocatalysts fabricated at low temperatureand the correlation between phase compositionand photocatalytic activity," *Journal of Environmental Sciences*, vol. 20, no. 10, pp. 1263–1267, Jan. 2008, doi: 10.1016/S1001-0742(08)62219-6.

[37] R. J. Tayade, P. K. Surolia, R. G. Kulkarni, and R. V. Jasra, "Photocatalytic degradation of dyes and organic contaminants in water using nanocrystalline anatase and rutile TiO_2," *Science and Technology of Advanced Materials*, vol. 8, no. 6, pp. 455–462, Jan. 2007, doi: 10.1016/j.stam.2007.05.006.

[38] T. S. Natarajan, M. Thomas, K. Natarajan, H. C. Bajaj, and R. J. Tayade, "Study on UV-LED/TiO2 process for degradation of Rhodamine B dye," *Chemical Engineering Journal*, vol. 169, no. 1–3, pp. 126–134, May 2011, doi: 10.1016/j.cej.2011.02.066.

[39] S. Goulart-Gonçalves *et al.*, "Direct synthesis of TiO2 nanoparticles without heat treatment: Effect of order of addition and precursor/reducing ratio," *Journal of Physics and Chemistry of Solids*, vol. 180, p. 111368, Sep. 2023, doi: 10.1016/j.jpcs.2023.111368.

[40] L. Laysandra *et al.*, "Adsorption and photocatalytic performance of bentonite-titanium dioxide composites for methylene blue and rhodamine B decoloration," *Heliyon*, vol. 3, no. 12, p. e00488, Dec. 2017, doi: 10.1016/j.heliyon.2017.e00488.

[41] A. Khataee, M. Sheydaei, A. Hassani, M. Taseidifar, and S. Karaca, "Sonocatalytic removal of an organic dye using TiO2/Montmorillonite nanocomposite," *Ultrasonics Sonochemistry*, vol. 22, pp. 404–411, Jan. 2015, doi: 10.1016/j.ultsonch.2014.07.002.

[42] S. Cukrowicz *et al.*, "Organobentonites Modified with Poly(Acrylic Acid) and Its Sodium Salt for Foundry Applications," *Materials*, vol. 14, no. 8, p. 1947, Apr. 2021, doi: 10.3390/ma14081947.

[43] D. P. Kgabi and A. A. Ambushe, "Characterization of South African Bentonite and Kaolin Clays," *Sustainability*, vol. 15, no. 17, p. 12679, Aug. 2023, doi: 10.3390/su151712679.

[44] M. Kassir *et al.*, "Adsorption and photocatalysis activity of TiO2/bentonite composites," *Desalination and Water Treatment*, vol. 98, pp. 196–215, Dec. 2017, doi: 10.5004/dwt.2017.21578.

[45] M. Kassir *et al.*, "Modification contrôlée des propriétés cristallochimiques et physico-chimiques de matériaux nanostructurés à base de TiO2 pour la maitrise des propriétés photocatalytiques".

[46] M. Supeno and R. Siburian, “Role of TiO_2 pillared bentonite-Co catalyst Ni to convert glucose hydrogenation to be sorbitol,” *J. Phys.: Conf. Ser.*, vol. 1116, p. 042038, Dec. 2018, doi: 10.1088/1742-6596/1116/4/042038.

[47] D. Kim *et al.*, “Synthesis and Characterization of Montmorillonite-Supported Tio_2 Composites for Enhanced UV Absorption,” *Clays and clay miner.*, vol. 68, no. 6, pp. 533–543, Dec. 2020, doi: 10.1007/s42860-020-00094-6.

[48] T. U. Rehman *et al.*, “Fabrication of stable superabsorbent hydrogels for successful removal of crystal violet from waste water,” *RSC Adv.*, vol. 9, no. 68, pp. 40051–40061, 2019, doi: 10.1039/C9RA08079A.

[49] Y. Qi *et al.*, “A Critical Review of Clay Mineral-Based Photocatalysts for Wastewater Treatment,” *Catalysts*, vol. 14, no. 9, p. 575, Aug. 2024, doi: 10.3390/catal14090575.

[50] S. H. Siregar, P. Prasetya, N. Norramizawati, M. Marlian, and A. R. Ramadhanti, “Titanium Dioxide (TiO2) Modified Bentonite for Photodegradation in Methylene Blue Dye,” *J. Kim. Sains Apl.*, vol. 26, no. 4, pp. 143–150, Jun. 2023, doi: 10.14710/jksa.26.4.143-150.

[51] R. Cherouaki, Y. Gherraby, R. Bassam, S. Belaaouad, and J. Naja, “Adsorption and photocatalytic degradation investigation of organic dyes on TiO2 bentonite surface in aqueous solution,” *Desalination and Water Treatment*, vol. 291, pp. 195–204, Apr. 2023, doi: 10.5004/dwt.2023.29470.

[52] S. D. Khairnar, M. R. Patil, and V. S. Shrivastava, “IRANIAN JOURNAL OF CATALYSIS,” 2018.

[53] Y. Li, S. Sun, M. Ma, Y. Ouyang, and W. Yan, “Kinetic study and model of the photocatalytic degradation of rhodamine B (RhB) by a TiO_2-coated activated carbon catalyst: Effects of initial RhB content, light intensity and TiO_2 content in the catalyst,” *Chemical Engineering Journal*, vol. 142, no. 2, pp. 147–155, Aug. 2008, doi: 10.1016/j.cej.2008.01.009.

[54] S.-Z. Kang, T. Wu, X. Li, and J. Mu, “Effect of montmorillonite on the photocatalytic activity of TiO2 nanoparticles,” *Desalination*, vol. 262, no. 1–3, pp. 147–151, Nov. 2010, doi: 10.1016/j.desal.2010.06.003.

[55] L.-K. Meng, C.-Y. Cao, and K. Tang, “Study on Disposal of Textile Dyes in Aqueous Solution by TiO_2 Pillared Bentonite,” *Separation Science and Technology*, vol. 48, no. 15, pp. 2302–2306, Oct. 2013, doi: 10.1080/01496395.2013.803486.

[56] N. P. Lata, Md. S. Hussain, Md. Abdulla-Al-Mamun, T. U. Rashid, and S. Md. Shamsuddin, “Fabrication and synergistically enhanced photocatalytic activity of ternary kaolinite, TiO2, and Al2O3 (K65T30A5) nanocomposite for visible-light-induced degradation of methylene blue and remazol red dye,” *Heliyon*, vol. 10, no. 8, p. e29255, Apr. 2024, doi: 10.1016/j.heliyon.2024.e29255.

[57] D. Ewis, M. M. Ba-Abbad, A. Benamor, and M. H. El-Naas, “Adsorption of organic water pollutants by clays and clay minerals composites: A comprehensive review,” *Applied Clay Science*, vol. 229, p. 106686, Nov. 2022, doi: 10.1016/j.clay.2022.106686.

[58] A. Alraae *et al.*, “One-step eco-friendly synthesis of Ag nanoparticles on bentonite-g-C_3N_4 for the reduction of hazardous organic pollutants in industrial wastewater.,” *Next Nanotechnology*, vol. 7, p. 100116, 2025, doi: 10.1016/j.nxnano.2024.100116.

[59] A. Fujishima and K. Honda, “Electrochemical Photolysis of Water at a Semiconductor Electrode,” *Nature*, vol. 238, no. 5358, pp. 37–38, Jul. 1972, doi: 10.1038/238037a0.

[60] F. Kooli, Y. Liu, R. Al-Faze, and A. Al Suhaimi, “Effect of acid activation of Saudi local clay mineral on removal properties of basic blue 41 from an aqueous solution,” *Applied Clay Science*, vol. 116–117, pp. 23–30, Nov. 2015, doi: 10.1016/j.clay.2015.07.044.

[61] S. Khan, S. Ajmal, T. Hussain, and M. U. Rahman, “Clay-based materials for enhanced water treatment: adsorption mechanisms, challenges, and future directions,” *J.Umm Al-*

Qura Univ. Appll. Sci., vol. 11, no. 2, pp. 219–234, Jun. 2025, doi: 10.1007/s43994-023-00083-0.
[62] K. Sahel *et al.*, "Photocatalytic degradation of anionic and cationic dyes over TiO2 P25, and Ti-pillared clays and Ag-doped Ti-pillared clays," *Applied Clay Science*, vol. 95, pp. 205–210, Jun. 2014, doi: 10.1016/j.clay.2014.04.014.

Chapter IV:

Kinetic analysis of synthesized photocatalysts

1. Introduction

The kinetics of Rhodamine B dye photodegradation using different synthesized catalyst samples were evaluated using pseudo-first-order (Equation IV.1) and pseudo-second-order (Equation IV.2) models, as illustrated in Figure 14. a-b:

Pseudo-first order $ln\left(\frac{C_0}{C_t}\right) = k_1t$ Equation IV.1

Pseudo second order $ln\left(\frac{1}{C_t}\right) = \left(\frac{1}{C_0}\right) + k_2t$ Equation IV.2

C_0 is the initial concentration (mg/L) of Rhodamine B, while C_t is the concentration of Rhodamine B at time t (mg/L), and t represents the contact time in minutes (min). k_1 and k_2 are the first and second-order rate constants, respectively. In the same context, the adsorption and photocatalytic activity of the photocatalysts are predicted using the Langmuir-Hinshelwood (L-H) equation, as it is also commonly employed to describe heterogeneous photocatalysis in several studies

[1,2]. Equation 3 represents a straight line with an intercept of $1/k_a$ and a slope of $1/k_aK$, as derived for the L-H model, where K is the adsorption coefficient of the reactant in ($L.mg^{-1}$) and k_a is the reaction rate constant in ($mg.\ L^{-1}.min^{-1}$)[3]:

$$\frac{\mathbf{1}}{\boldsymbol{r_0}} = \frac{\mathbf{1}}{\boldsymbol{k}} + \frac{\mathbf{1}}{\boldsymbol{kKC_0}} \qquad \text{Equation IV.3}$$

2. Photodegradation kinetics of Rhodamine B using TiO_2 photocatalyst:

As shown in Figure 2, the pseudo-first-order model provided a better fit than the pseudo-second-order model, indicating a significant correlation between $ln(C_0/C_t)$ and time. The rate constants (k_1) suggest that TiO_2-400 has the highest degradation rate, with $k_1 = 0.0377\ min^{-1}$ (Table IV.1), which can be attributed to its physicochemical properties, including a higher specific surface area (62.83 m^2/g), smaller crystallite size, and predominant anatase phase (67.89% anatase and 32.10% rutile), as confirmed by BET and XRD analysis. Additionally, TiO_2-400 exhibits an optical band gap energy of 3.14 eV, which contributes to its enhanced photocatalytic activity. In contrast, TiO_2-600 and TiO_2-800 exhibited lower rate constants, 0.0336 and 0.0202 min^{-1}, respectively, compared to TiO_2-400 and TiO_2-P25. This decrease in photocatalytic activity is attributed to a reduction in specific surface area, an increase in crystallite size, and the anatase-to-rutile phase transformation that occurs at higher calcination temperatures. Therefore, the phase transitions result in a reduced number of active sites and diminished charge separation efficiency [4,5]

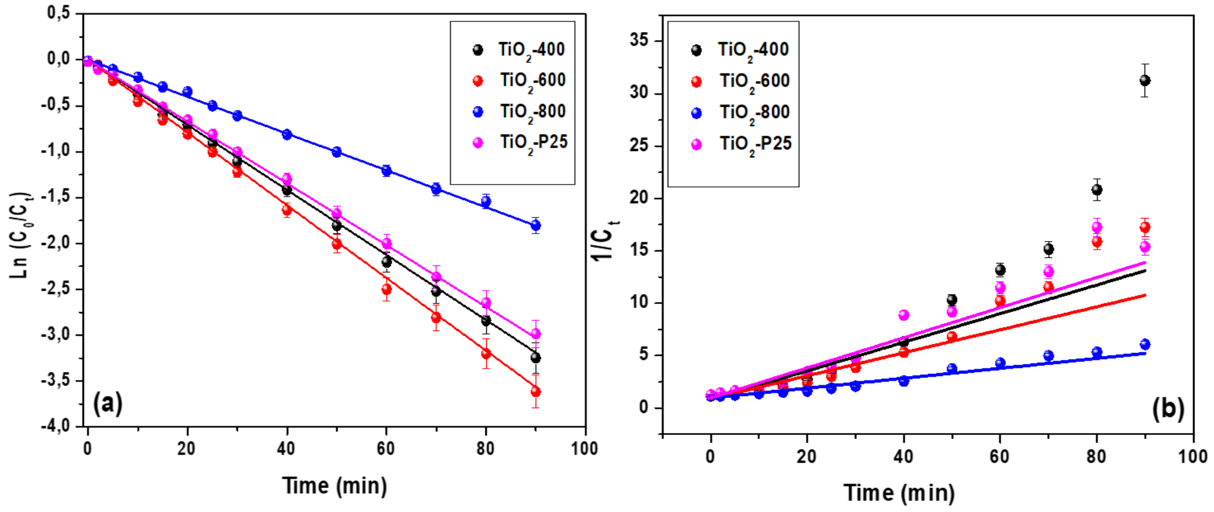

Figure IV.1. (a) Pseudo-first-order, (b) Pseudo-second-order kinetics fitting of Rhodamine dye photodegradation using different TiO_2 samples.
(Operational parameters: UV lamp: λ_{254nm}, intensity 4750 µW/cm², $[TiO_2]_0 = 0.1$ g/L, $[RhB]_0 = 10$ ppm, pH = 4.80).

Additionally, the increased particle agglomeration observed at higher calcination temperatures decreases the available surface area, contributing to the lower photocatalytic performance compared to TiO_2-400, as confirmed by SEM analysis [6]. The kinetic parameters derived from the L-H model are presented in Table IV.1, revealing a strong correlation between the degradation rate and the adsorption characteristics of the TiO_2 samples.

Table IV.1. Kinetics models and Langmuir-Hinshelwood representation parameters of Rhodamine B photodegradation using different TiO_2 samples.

TiO_2 samples		TiO_2-400	TiO_2-600	TiO_2-800	TiO_2-P25
First-order kinetics	k_1 (min^{-1})	0,0377	0,0336	0,0202	0,0349
	R^2	0,9940	0,9909	0,9958	0,9921
Second-order kinetics	k_2 (mg. L^{-1}min^{-1})	0,283	0,179	0,0570	0,188
	R^2	0,7650	0,8851	0,9840	0,7450
Langmuir-Hinshelwood	K (L.mg^{-1})	0.0436	0.0988	0.1616	0.0824
	k_a(mg.L^{-1}.min^{-1})	1,5696	0,7484	0,3198	0,8762
	R^2	0,9973	0,9925	0,9921	0,9931

Among the studied materials, TiO_2-400 exhibits the highest adsorption constant (K = 0.0436 $L\cdot mg^{-1}$) and the highest apparent rate constant (k_a = 1.5696 mg. $L^{-1}\cdot min^{-1}$), with an excellent correlation coefficient ($R^2 = 0.9973$) as shown in Figure IV.2. These results suggest an enhanced interaction between Rhodamine B molecules and the TiO_2-400 surface under photocatalytic conditions, leading to improved degradation kinetics. The progressive decrease in K and increase in k_a constants with rising calcination temperature is consistent with the anatase-to-rutile phase transition, resulting in a reduced specific surface area and increased crystallite size, which, in turn, influence photocatalytic performance [7]. For all samples, k_a values were higher than K, indicating that the photocatalytic process is driven by surface reactions, as reported in the literature [3].

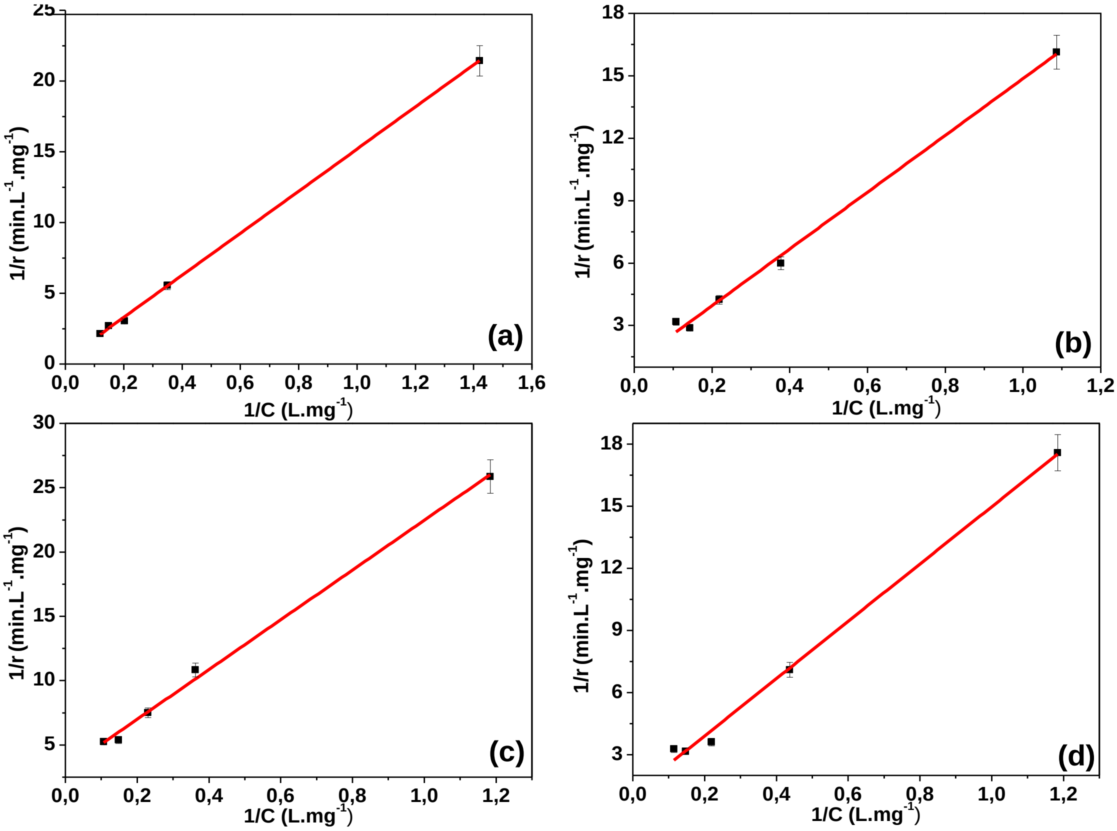

Figure IV.2. Representation of Langmuir-Hinshelwood equation of Rhodamine dye photodegradation using different TiO_2 samples **(a)** TiO_2-400, **(b)** TiO_2-600, **(c)** TiO_2-800, **(d)** TiO_2-P25
(Operational parameters: UV lamp: λ_{254nm}, intensity 4750 $\mu W/cm^2$, $[TiO_2]_0$ = 0.1 g/L, $[RhB]_0$ = 10 ppm, natural pH = 4.80).

3. Photodegradation kinetics of Rhodamine B using TiO_2-BN composites:

The experimental data of the TiO_2-BN samples were fitted for both pseudo-first-order and pseudo-second-order kinetic models to elucidate the photodegradation behaviour of Rhodamine B dye. As shown in Figure IV.3, the pseudo-first-order model provided a better fit than the pseudo-second-order model. Among the tested composites, the 50% TiO_2-BN sample exhibited the highest apparent rate constant in both models (k_1 = 0.05802 min^{-1}; k_2 = 2.35245 $mg \cdot L^{-1} \cdot min^{-1}$), indicating an efficient generation of reactive oxygen species (ROS), due to greater availability of photoactive TiO_2 sites. This finding aligns with recent studies, which have shown that increasing TiO_2 content enhances ROS formation and photocatalytic efficiency up to an optimal loading [8], [9]. The 30% TiO_2-BN sample displayed intermediate activity (k_1 = 0.04914 min^{-1}; k_2 = 0.80481 $mg \cdot L^{-1} \cdot min^{-1}$), suggesting a balanced interplay between TiO_2 dispersion and surface accessibility. In contrast, the 10% TiO_2-BN sample yielded the lowest kinetic constants (k_1 = 0.02562 min^{-1}; k_2 = 0.1101 $mg \cdot L^{-1} \cdot min^{-1}$), which can be attributed to insufficient photocatalytic sites and limited ROS production [10].

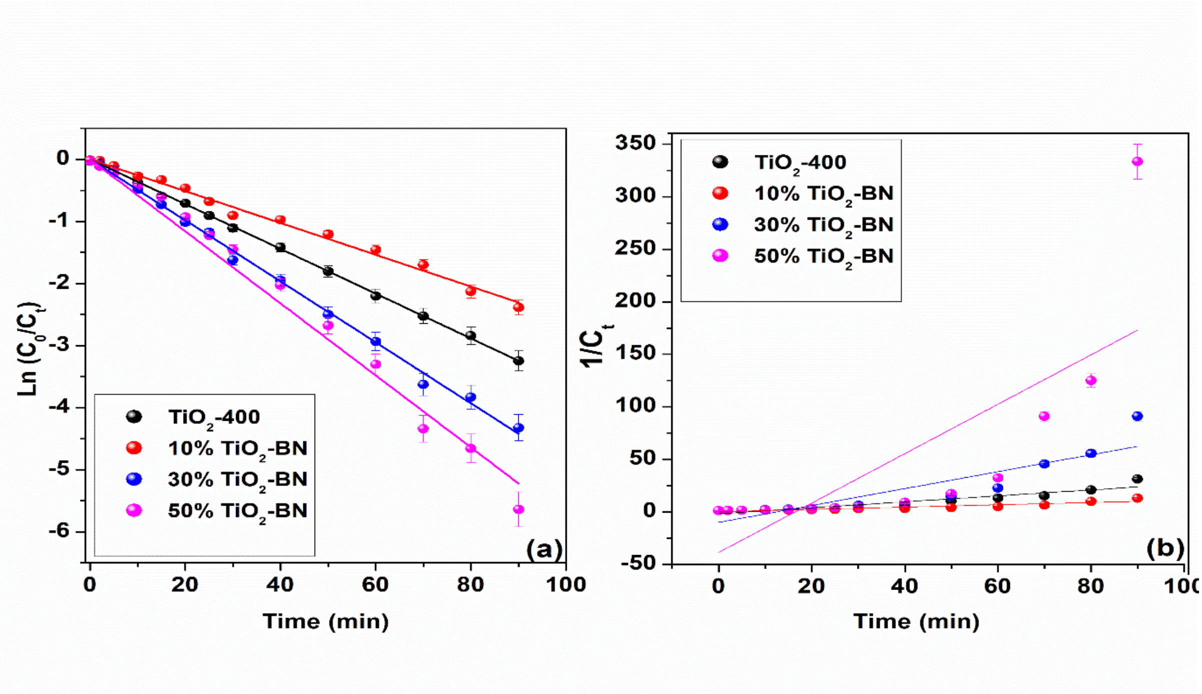

Figure IV.3. (a) Pseudo-first-order, (b) Pseudo-second-order kinetics fitting of Rhodamine dye photodegradation using TiO_2-400 and different TiO_2-BN samples. (Operational parameters: UV lamp: λ_{254nm}, intensity 4750 $\mu W/cm^2$, $[TiO_2]_0$ = 0.1 g/L, $[RhB]_0$ = 10 ppm, pH = 4.80).

However, for the 10%TiO_2-BN and 30%TiO_2-BN samples, the pseudo-second-order model also exhibited relatively considerable R^2 values (0.8584 and 0.78465, respectively), indicating a possible influence of surface adsorption processes or active site saturation, especially with low TiO_2 content [11]. In contrast, the second-order fit for 50% TiO_2-BN was lower (R^2 = 0.56613), further supporting that degradation here was driven by photogenerated species rather than surface-controlled kinetics. Although the pseudo-first-order model showed that the 50% TiO_2-BN composite had the highest apparent rate constant ($k_1 = 0.05802\ min^{-1}$), indicating rapid RhB degradation.

Furthermore, the Langmuir-Hinshelwood model (Figure IV.4) showed a significantly lower surface reaction rate ($k_a = 0.0705\ mg \cdot L^{-1} \cdot min^{-1}$) for the sample 50% TiO_2-BN. In contrast, the 10% TiO_2-BN composite exhibited a higher rate ($k_a = 1.325\ mg \cdot L^{-1} \cdot min^{-1}$), indicating more effective surface catalysis despite having less TiO_2. This difference arises because the pseudo-first-order model captures overall degradation mainly driven by ROS generation, while the L–H model provides mechanistic insights by separating adsorption from surface reactions [12].

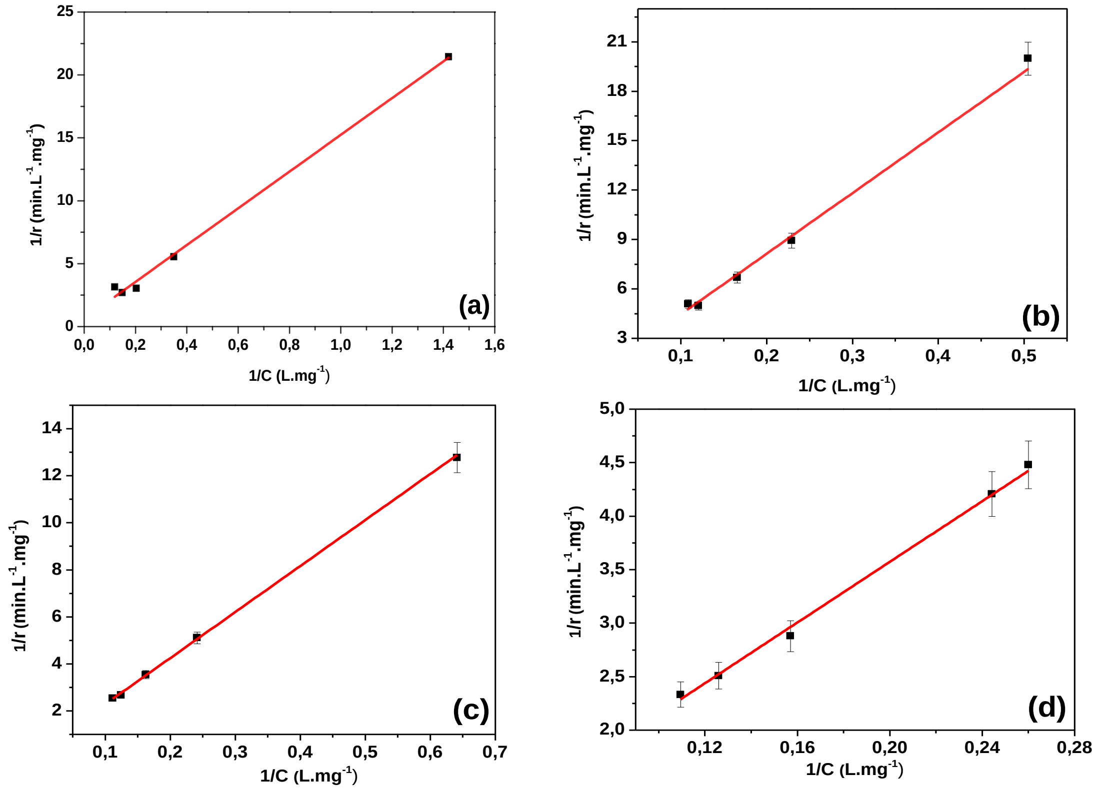

Figure IV.4. Representation of the Langmuir-Hinshelwood equation of Rhodamine dye photodegradation using TiO_2-400 different TiO_2 samples:
(a)TiO_2-400 (b) 10%TiO_2-BN, (c) 30%TiO_2-BN, (d) 50%TiO_2-BN
(Operational parameters: UV lamp: λ_{254nm}, intensity 4750 µW/cm², $[TiO_2]_0$ = 0.1 g/L, $[RhB]_0$ = 10 ppm, natural pH = 4.80)

In contrast, the 30% TiO_2-BN composite exhibited a considerable decrease in photocatalytic activity (k_a = 0.0509 mg.L^{-1}·min^{-1}, K = 0.0168 L.mg^{-1}), which can be attributed to the agglomeration of TiO_2 nanoparticles and the consequent reduction in accessible active sites. This agglomeration limited both the adsorption capacity and the efficiency of the photocatalytic reaction. Although the 50%TiO_2-BN sample showed a higher adsorption constant (K = 0.0519 L·mg^{-1}), its degradation rate remained relatively low (k_a = 0.0705 mg·L^{-1}·min^{-1}), suggesting that enhanced adsorption alone is not sufficient to ensure improved photocatalytic performance. Such behaviour is often associated with overloading effects, which may hinder charge transfer, increase electron-hole recombination rates, or reduce light penetration within the catalyst matrix [13]. The high correlation coefficients ($R^2 > 0.99$) for all samples support the applicability of the L-H model in describing the photodegradation kinetics of RhB over these composites. These findings highlight the importance of optimizing the TiO_2 content within bentonite matrices to strike a balance between adsorption capacity and photocatalytic reactivity, thereby achieving efficient pollutant removal [14].

Table IV.2. Kinetics models and Langmuir-Hinshelwood representation parameters of Rhodamine B photodegradation using TiO_2-400 and TiO_2-BN samples.

TiO_2 samples		TiO_2-400	10% TiO_2-BN	30% TiO_2-BN	50% TiO_2-BN
First-order kinetics	k_1 (min^{-1})	0,0377	0,02562	0,04914	0,05802
	R^2	0,9940	0,99651	0,99861	0,99229
Second-order kinetics	k_2 (mg. L^{-1}min^{-1})	0,283	0,1101	0,80481	2,35245
	R^2	0,7650	0,8584	0,78465	0,56613
Langmuir-Hinshelwood	K(L.mg^{-1})	0,0436	0,0206	0,0168	0,0519
	k_a (mg.L^{-1}.min^{-1})	1,5696	1,325	0,0509	0,0705
	R^2	0,9973	0,9937	0,9976	0,99281

4. Photocatalytic performance comparison: TiO_2-400 *vs.* 50%TiO_2-BN:

As a final step in the kinetic analysis, a comparative evaluation was conducted between the two most efficient photocatalysts, TiO_2 calcined at 400 °C (TiO_2-400) and the 50%TiO_2-bentonite composite (50%TiO_2-BN) to assess the effect of bentonite incorporation on photocatalytic performance (Table IV.3). Both materials exhibited high degradation efficiencies toward Rhodamine B under UV irradiation; however, the 50%TiO_2-BN composite demonstrated superior performance, achieving 99.64% degradation compared to 96.11% for TiO_2-400 after 90 minutes.

Table IV.3. Comparison of photodegradation efficiency and kinetic parameters of TiO_2-400 and 50%TiO_2-Bentonite composites under UV Irradiation.

Sample	Photodegradation efficiency (%)	Irradiation time (min)	k_1 (min^{-1})	k_a($mg.L^{-1}.min^{-1}$)	K($L.mg^{-1}$)
TiO_2-400	96,11	90	0,0377	1,5696	0,0436
50%TiO_2-BN	99,64	90	0,05802	0,0705	0,0519

The pseudo-first-order rate constant (k_1) of 50%TiO_2-BN was slightly higher for the composite (0.05802 min^{-1}) compared to TiO_2-400 (0.0377 min^{-1}) due to improved adsorption facilitated by the bentonite matrix. This is further supported by the higher Langmuir-Hinshelwood adsorption constant observed for the composite ($K = 0.0519\ L \cdot mg^{-1}$ vs. $0.0436\ L \cdot mg^{-1}$ for TiO_2-400). However, the apparent rate constant k_a was significantly lower for 50%TiO_2-BN (0.0705 $mg \cdot L^{-1} \cdot min^{-1}$) than for TiO_2-400 (1.5696 $mg \cdot L^{-1} \cdot min^{-1}$), suggesting that the presence of excess bentonite may hinder photocatalytic reaction kinetics by limiting light penetration, reducing active site accessibility, or promoting charge carrier recombination [15].

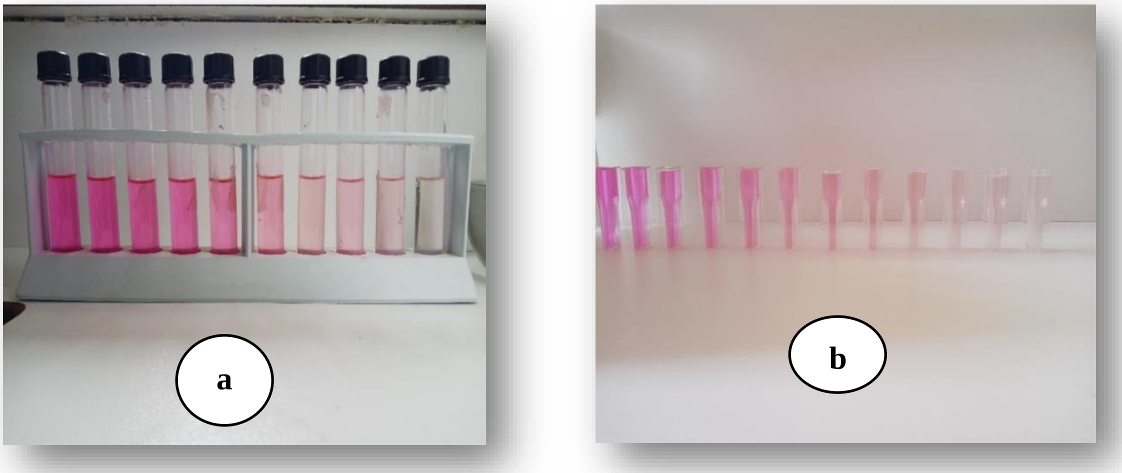

Figure IV.5. Photodegradation of Rhodamine B using (a) TiO_2-400 and (b) 50%TiO_2-Bentonite composite

Figure IV.5 illustrate the progressive discolouration of Rhodamine B solution during photocatalytic treatment. Figure (a) corresponds to TiO_2-400, while Figure (b) depicts the degradation behaviour obtained with the 50%TiO_2-BN composite, highlighting the enhanced catalytic efficiency. Similar effects have been reported in the literature for TiO_2-clay systems with high support content [16]. These findings demonstrate that although bentonite can enhance adsorption and improve material recovery, its proportion must be carefully optimized to ensure that the intrinsic photocatalytic activity of TiO_2 is not compromised.

5. Conclusion

This chapter provided a detailed assessment of the photocatalytic performance and kinetic behaviour of synthesised TiO_2-based catalysts, including pure TiO_2 calcined at various temperatures and TiO_2-BN composites with different TiO_2 loadings. The photodegradation of Rhodamine B under UV light was used as a model reaction to evaluate the activity of each material. kinetic modelling with pseudo-first-order, pseudo-second-order, and Langmuir–Hinshelwood models offered valuable insights into degradation mechanisms and adsorption-reaction processes. Among all samples, TiO_2-400 showed the highest apparent reaction rate constant, underscoring the importance of optimal crystallinity and surface properties. Nonetheless, the 50%TiO_2-BN composite demonstrated superior adsorption capacity and competitive degradation efficiency, highlighting bentonite’s role as a support material. However, excessive bentonite content was found to potentially impair photocatalytic performance by restricting active site access or increasing charge recombination. Overall, the results emphasise that both the physicochemical properties and composition of the catalysts significantly affect photocatalytic behaviour, and that a careful balance between the support structure and the active phase is crucial for achieving high photocatalytic efficiency. These findings lay a strong foundation for optimising TiO_2-based systems in environmental remediation.

References:

[1] W. Baran, E. Adamek, and A. Makowski, “The influence of selected parameters on the photocatalytic degradation of azo-dyes in the presence of TiO2 aqueous suspension,” *Chemical Engineering Journal*, vol. 145, no. 2, pp. 242–248, Dec. 2008, doi: 10.1016/j.cej.2008.04.021.

[2] J. P. S. Valente, P. M. Padilha, and A. O. Florentino, “Studies on the adsorption and kinetics of photodegradation of a model compound for heterogeneous photocatalysis onto TiO2,” *Chemosphere*, vol. 64, no. 7, pp. 1128–1133, Aug. 2006, doi: 10.1016/j.chemosphere.2005.11.050.

[3] M. Hasmath Farzana and S. Meenakshi, “Photocatalytic aptitude of titanium dioxide impregnated chitosan beads for the reduction of Cr(VI),” *International Journal of Biological Macromolecules*, vol. 72, pp. 1265–1271, Jan. 2015, doi: 10.1016/j.ijbiomac.2014.09.029.

[4] T. Ishigaki *et al.*, “Enhanced visible-light photocatalytic activity of anatase-rutile mixed-phase nano-size powder given by high-temperature heat treatment,” *R. Soc. open sci.*, vol. 7, no. 1, p. 191539, Jan. 2020, doi: 10.1098/rsos.191539.

[5] L. Jing, X. Qin, Y. Luan, Y. Qu, and M. Xie, “Synthesis of efficient TiO2-based photocatalysts by phosphate surface modification and the activity-enhanced mechanisms,” *Applied Surface Science*, vol. 258, no. 8, pp. 3340–3349, Feb. 2012, doi: 10.1016/j.apsusc.2011.07.101.

[6] F. Pellegrino *et al.*, “Influence of agglomeration and aggregation on the photocatalytic activity of TiO 2 nanoparticles,” *Applied Catalysis B: Environmental*, vol. 216, pp. 80–87, Nov. 2017, doi: 10.1016/j.apcatb.2017.05.046.

[7] S. Phromma, T. Wutikhun, P. Kasamechonchung, T. Eksangsri, and C. Sapcharoenkun, “Effect of Calcination Temperature on Photocatalytic Activity of Synthesized TiO2 Nanoparticles via Wet Ball Milling Sol-Gel Method,” *Applied Sciences*, vol. 10, no. 3, p. 993, Feb. 2020, doi: 10.3390/app10030993.

[8] Y. Kumar, S. Kumar, and J. Sangwai, “Effect of Clay on the kinetics of CO2 hydrate relevant for Carbon Capture and Sequestration”.

[9] H. Li, Y. Yao, X. Yang, X. Zhou, R. Lei, and S. He, “Degradation of Phenol by Photocatalysis Using TiO2/Montmorillonite Composites Under UV Light,” Sep. 27, 2021. doi: 10.21203/rs.3.rs-848926/v1.

[10] R. Djellabi *et al.*, “Titania–Montmorillonite for the Photocatalytic Removal of Contaminants from Water: Adsorb & Shuttle Process,” in *Green Materials for Wastewater Treatment*, vol. 38, Mu. Naushad and E. Lichtfouse, Eds., in Environmental Chemistry for a Sustainable World, vol. 38. , Cham: Springer International Publishing, 2020, pp. 291–319. doi: 10.1007/978-3-030-17724-9_13.

[11] Z. Tang and T. Cheng, “Stability and aggregation of nanoscale titanium dioxide particle (nTiO2): Effect of cation valence, humic acid, and clay colloids,” *Chemosphere*, vol. 192, pp. 51–58, Feb. 2018, doi: 10.1016/j.chemosphere.2017.10.105.

[12] Z. Zheng *et al.*, “Correlation of the Catalytic Activity for Oxidation Taking Place on Various TiO_2 Surfaces with Surface OH Groups and Surface Oxygen Vacancies,” *Chemistry A European J*, vol. 16, no. 4, pp. 1202–1211, Jan. 2010, doi: 10.1002/chem.200901601.

[13] R. Cherouaki, Y. Gherraby, R. Bassam, S. Belaaouad, and J. Naja, “Adsorption and photocatalytic degradation investigation of organic dyes on TiO2 bentonite surface in aqueous solution,” *Desalination and Water Treatment*, vol. 291, pp. 195–204, Apr. 2023, doi: 10.5004/dwt.2023.29470.

[14] Y. S. Ngoh and M. A. Nawi, “Role of bentonite adsorbent sub-layer in the photocatalytic-adsorptive removal of methylene blue by the immobilized TiO2/bentonite system,” *Int. J. Environ. Sci. Technol.*, vol. 13, no. 3, pp. 907–926, Mar. 2016, doi: 10.1007/s13762-015-0928-5.

[15] Z. Ghasemi, H. Younesi, and A. A. Zinatizadeh, “Kinetics and thermodynamics of photocatalytic degradation of organic pollutants in petroleum refinery wastewater over nano-TiO2 supported on Fe-ZSM-5,” *Journal of the Taiwan Institute of Chemical Engineers*, vol. 65, pp. 357–366, Aug. 2016, doi: 10.1016/j.jtice.2016.05.039.

[16] M. A. García-Muñoz *et al.*, “Influence of compatibility in the EVA/starch/organoclay biodegradable nanocomposite on thermal properties and flame self-extinguishing behavior,” *Polymer-Plastics Technology and Materials*, vol. 62, no. 17, pp. 2318–2333, Nov. 2023, doi: 10.1080/25740881.2023.2258396.

General conclusion

This thesis examined advanced oxidation processes (AOPs) based on heterogeneous and homogeneous photocatalysis for removing refractory organic pollutants from water, with particular focus on Rhodamine B (RhB) as a model contaminant. The main aim was to synthesise, characterize, and optimize nanostructured photocatalysts based on titanium dioxide (TiO_2), prepared via a non-conventional sol-gel method, and to investigate how structural modifications, composite formation, and operational conditions affect their photocatalytic efficiency. Initially, pure TiO_2 nanoparticles were successfully synthesised and subjected to controlled calcination at 400, 600, and 800 °C. Detailed physicochemical characterisation (TG/DSC, XRD, FTIR-ATR, BET, UV–Vis spectroscopy) demonstrated the significant influence of calcination temperature on crystallinity, surface area, and phase composition. Among the samples, TiO_2-400 exhibited the most favourable properties, combining a high anatase content with adequate surface area, which contributed to superior photocatalytic activity (96.11%), surpassing TiO_2-600 (93.37%), TiO_2-800 (81.25%), and the benchmark TiO_2-P25 (92.07%), following a pseudo-first-order kinetic model consistent with the Langmuir-Hinshelwood mechanism. In the second phase, TiO_2/bentonite (TiO_2-BN) composites were synthesised using the same non-conventional sol-gel approach to overcome the inherent limitations of TiO_2 photocatalyst agglomeration and limited adsorption capacity. Structural analysis (FTIR-ATR, XRD, BET, SEM/EDS, pH_{pzc}) confirmed successful incorporation of TiO_2 into the bentonite matrix, resulting in composites with improved textural properties and enhanced surface reactivity. The photocatalytic performance of TiO_2-BN improved with increasing TiO_2 content. Specifically, the 10% TiO_2-BN composite achieved a degradation efficiency of 86.76%, while the 30% TiO_2-BN reached 98.67%. The highest activity was observed with the 50% TiO_2-BN sample, which exhibited a degradation efficiency of 99.64%. This trend clearly indicates that higher TiO_2 loading enhances the availability of active sites for photocatalytic reactions, while the bentonite matrix contributes to adsorption and stabilisation of TiO_2 nanoparticles, resulting in a synergistic effect that maximises overall photocatalytic efficiency. The influence of key parameters, including initial dye concentration, photocatalyst dosage, pH, irradiation source, and TiO_2 content, was systematically studied, confirming the crucial role of adsorption-photocatalysis synergy in pollutant removal efficiency. The non-conventional sol-gel method proved to be a reliable and versatile synthesis route, producing nanostructured catalysts with performance comparable or superior to commercial TiO_2. These findings deepen understanding of how structural and operational factors govern photocatalytic degradation and highlight the potential of TiO_2-based nanocatalysts for environmental remediation. Future work will focus on scaling up the synthesis process, evaluating catalyst stability and reusability over long-term cycles, and extending degradation studies to real wastewater samples containing complex pollutant mixtures. Additionally, combining TiO_2/bentonite composites with other strategies, such as metal/non-metal doping or hybridisation with carbon-based materials, could further enhance visible-light activity and broaden application scope. In conclusion, this research offers valuable insights into designing and optimising TiO_2-based nanocatalysts for wastewater treatment. By demonstrating the effectiveness of a non-convolutional sol-gel synthesis route and the beneficial role of bentonite addition, the work establishes a basis for developing more efficient, stable, and sustainable photocatalysts to tackle the persistent issue of refractory organic pollutants in aquatic environments.

ANNEXES

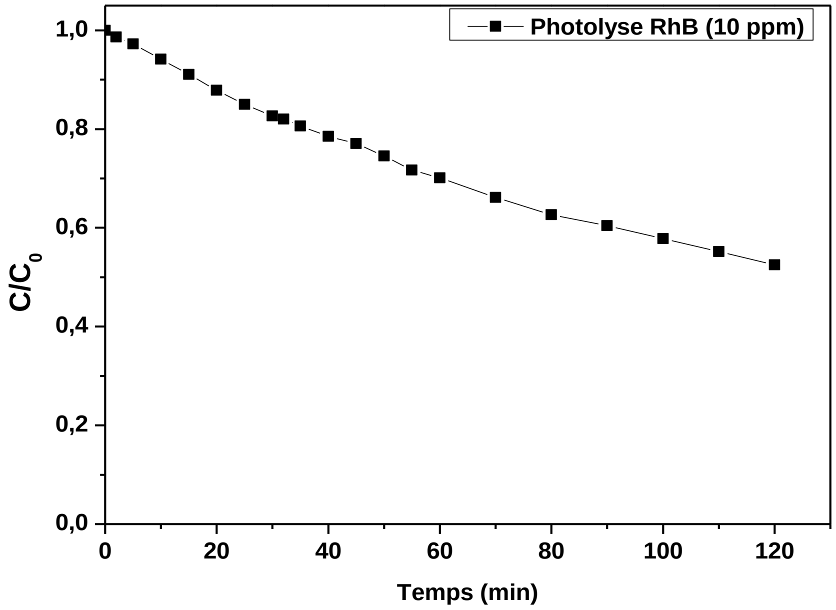

Figure A.1. Photolysis of Rhodamine B (10 ppm) under UV irradiation

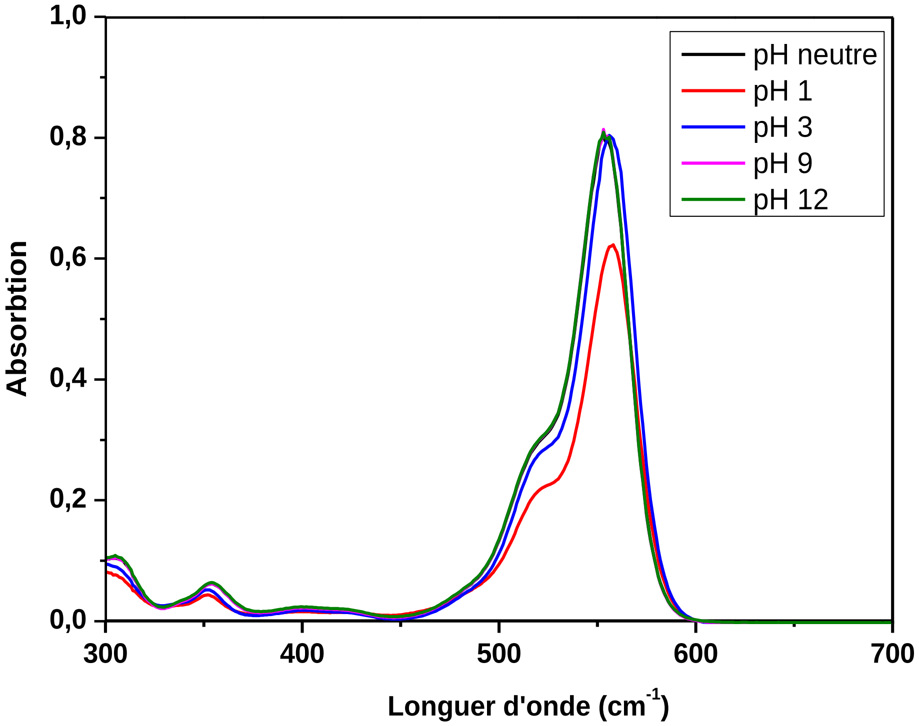

Figure A.2. UV-Vis absorption spectra of Rhodamine B at different pH values

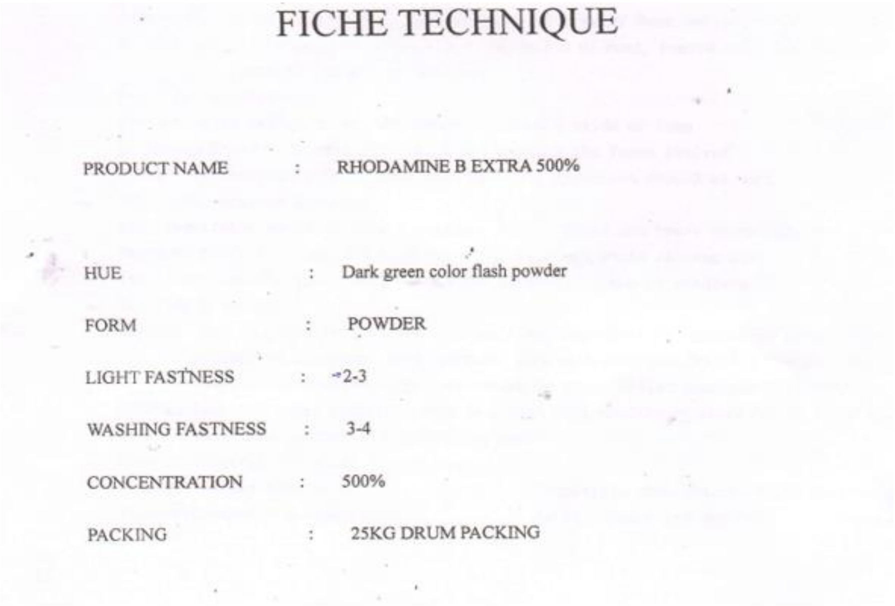

FICHE TECHNIQUE

PRODUCT NAME : RHODAMINE B EXTRA 500%

HUE : Dark green color flash powder
FORM : POWDER
LIGHT FASTNESS : 2-3
WASHING FASTNESS : 3-4
CONCENTRATION : 500%
PACKING : 25KG DRUM PACKING

Figure A.3. Technical data sheet of Rhodamine B

- **JCPDS reference cards extracted from the highScore database of TiO_2 and TiO_2-BN Samples:**

1. TiO_2 nanoparticles:

a) TiO_2-400 sample:

Name and formula (Anatase)

Reference code: 00-004-0477

Mineral name: Anatase, syn
Compound name: Titanium Oxide
PDF index name: Titanium Oxide

Empirical formula: O_2Ti
Chemical formula: TiO_2

Crystallographic parameters

Crystal system: Tetragonal
Space group: I41/amd
Space group number: 141

a (Å): 3,7830
b (Å): 3,7830
c (Å): 9,5100
Alpha (°): 90,0000

Beta (°): 90,0000
Gamma (°): 90,0000

Calculated density (g/cm^3): 3,90
Volume of cell (10^6 pm^3): 136,10
Z: 4,00

RIR: -

Status, subfiles and quality

Status: Marked as deleted by ICDD
Subfiles: Alloy, metal or intermetalic
Inorganic
Mineral
Pharmaceutical
Quality: Indexed (I)

Comments

Creation Date: 01/01/1970
Modification Date: 01/01/1970

References

Primary reference: Swanson, Tatge.,*Private Communication*, (1950)
Other: Parker.,*Z. Kristallogr.*, **59**, 1, (1923)

Peak list

No.	h	k	l	d [A]	2Theta[deg]	I [%]
1	1	0	1	3,51000	25,354	100,0
2	1	0	3	2,43500	36,884	9,0
3	0	0	4	2,37900	37,785	22,0
4	1	1	2	2,33600	38,507	9,0
5	2	0	0	1,89100	48,077	33,0
6	1	0	5	1,69900	53,922	21,0
7	2	1	1	1,66500	55,116	19,0
8	2	1	3	1,49400	62,075	4,0
9	2	0	4	1,48000	62,728	13,0
10	1	1	6	1,36700	68,596	5,0
11	2	2	0	1,33700	70,359	5,0
12	2	1	5	1,26400	75,094	10,0
13	3	0	1	1,25000	76,084	3,0
14	3	0	3	1,17100	82,267	2,0
15	3	1	2	1,16090	83,140	3,0
16				1,08690	90,261	3,0
17	3	2	1	1,04330	95,179	3,0
18	1	0	9	1,01730	98,436	2,0
19	3	1	6	0,95500	107,530	4,0
20	4	0	0	0,94610	109,014	3,0
21	3	2	5	0,91890	113,919	2,0
22	1	1	10	0,89600	118,568	3,0
23	2	2	8	0,88770	120,396	2,0

24	3	2	7	0,83110	135,896	1,0
25	4	1	5	0,82680	137,391	3,0
26	3	0	9	0,81000	143,974	1,0
27				0,79900	149,193	3,0

Stick Pattern

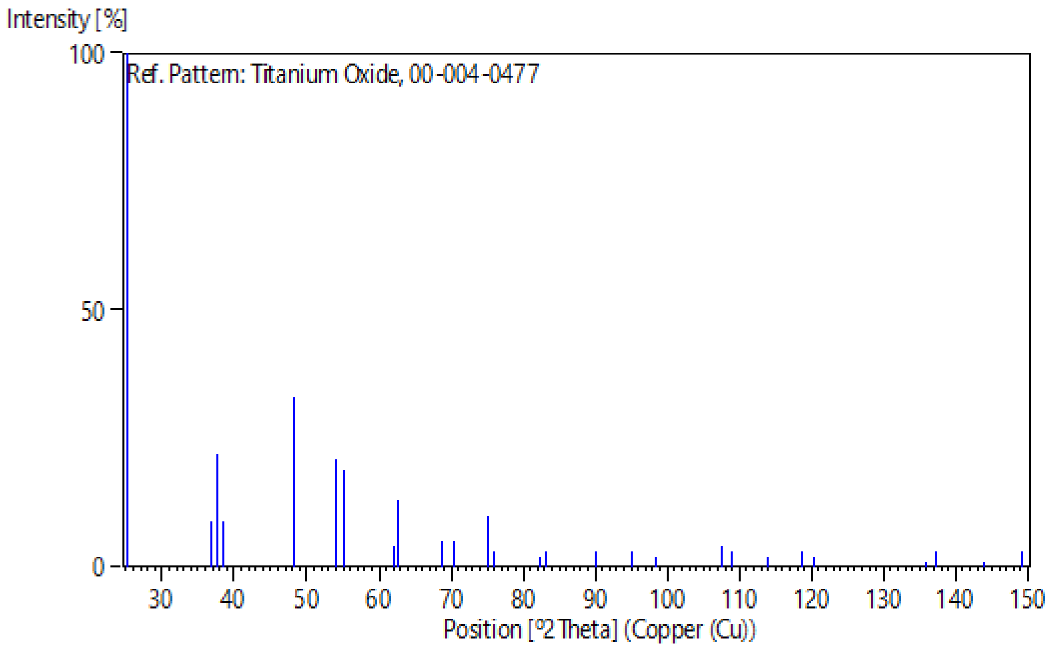

Name and formula (Rutile)

Reference code: 03-065-0190

Mineral name: Rutile, syn
Compound name: Titanium Oxide
PDF index name: Titanium Oxide

Empirical formula: O_2Ti
Chemical formula: TiO_2

Crystallographic parameters

Crystal system: Tetragonal
Space group: P42/mnm
Space group number: 136

a (Å): 4,5925
b (Å): 4,5925
c (Å): 2,9578
Alpha (°): 90,0000
Beta (°): 90,0000
Gamma (°): 90,0000

Calculated density (g/cm^3): 4,25
Volume of cell (10^6 pm^3): 62,38
Z: 2,00

RIR: 3,54

Status, subfiles and quality

Status: Marked as deleted by ICDD
Subfiles: Alloy, metal or intermetalic
Inorganic
Mineral
NIST Pattern
Pharmaceutical
Quality: Calculated (C)

Comments

Creation Date: 01/01/1970
Modification Date: 01/01/1970
N 22682 21030. Temperature Factor: No TF given for entry, B=1.0 assumed
Deleted Or Rejected By: Delete: same as 01-078-1508.

References

Structure: R.Restori, D.Schwarzenbach&J.R.Schneider, *ActaCrystallogr., Sec. B: Structural Science*, **43B**, 251-2, (1987)

Peak list

No.	h	k	l	d [A]	2Theta[deg]	I [%]
1	1	1	0	3,24739	27,443	100,0
2	1	0	1	2,48669	36,091	43,0
3	2	0	0	2,29625	39,201	6,4
4	1	1	1	2,18671	41,252	16,4
5	2	1	0	2,05383	44,055	5,7
6	2	1	1	1,68701	54,337	44,6
7	2	2	0	1,62369	56,642	13,0
8	0	0	2	1,47890	62,780	5,8
9	3	1	0	1,45228	64,066	5,9
10	2	2	1	1,42334	65,530	0,4
11	3	0	1	1,35954	69,025	13,6
12	1	1	2	1,34590	69,826	6,7
13	3	1	1	1,30361	72,441	0,7
14	3	2	0	1,27373	74,423	0,1
15	2	0	2	1,24334	76,565	1,4
16	2	1	2	1,20014	79,859	0,7
17	3	2	1	1,16987	82,363	2,6
18	4	0	0	1,14813	84,276	1,7

19	4	1	0	1,11384	87,509	0,6
20	2	2	2	1,09335	89,583	3,9
21	3	3	0	1,08246	90,734	2,1
22	4	1	1	1,04238	95,290	3,5
23	3	1	2	1,03620	96,042	2,7
24	4	2	0	1,02691	97,201	1,5
25	3	3	1	1,01653	98,537	0,1
26	4	2	1	0,97011	105,128	0,3
27	1	0	3	0,96397	106,087	1,0
28	1	1	3	0,94341	109,473	0,3
29	4	3	0	0,91850	113,996	0,1
30	4	0	2	0,90691	116,286	1,5
31	5	1	0	0,90066	117,577	1,6
32	4	1	2	0,88973	119,942	0,8
33	2	1	3	0,88882	120,143	3,0
34	4	3	1	0,87718	122,841	3,0
35	3	3	2	0,87348	123,738	2,1
36	5	1	1	0,86160	126,769	0,1
37	5	2	0	0,85281	129,178	0,1
38	4	2	2	0,84350	131,907	1,8
39	3	0	3	0,82890	136,655	2,0
40	5	2	1	0,81943	140,119	3,8
41	3	1	3	0,81572	141,582	0,2
42	4	4	0	0,81185	143,181	0,5

Stick Pattern

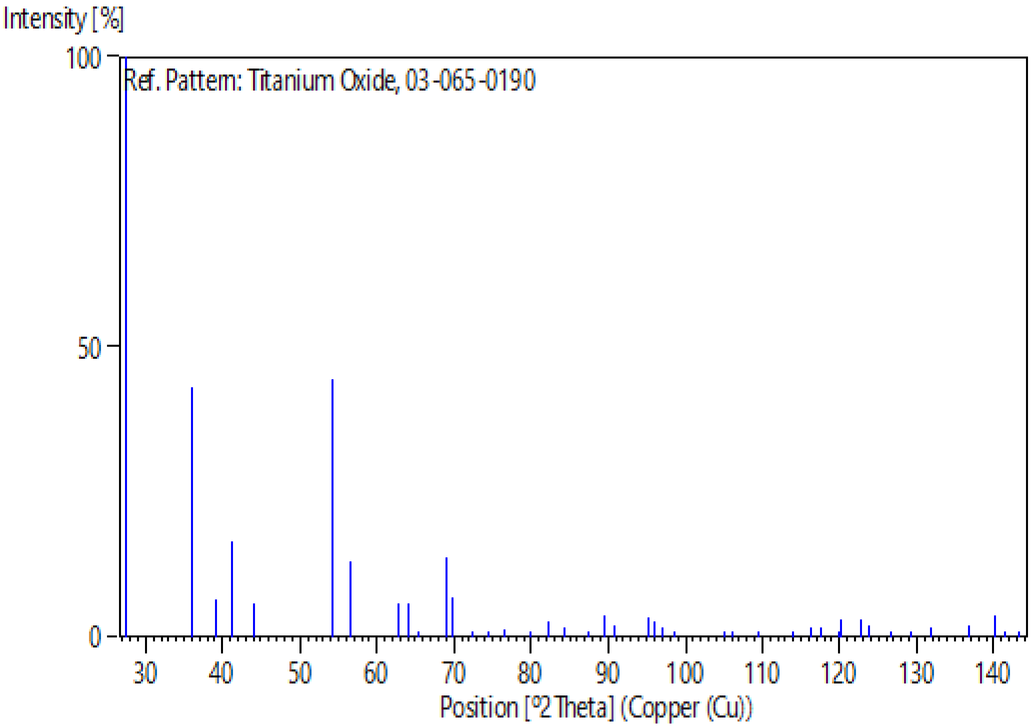

b) TiO_2-600 sample:

Name and formula (Anatase)

Reference code: 00-004-0477

Mineral name: Anatase, syn
Compound name: Titanium Oxide
PDF index name: Titanium Oxide

Empirical formula: O_2Ti
Chemical formula: TiO_2

Crystallographic parameters

Crystal system: Tetragonal
Space group: I41/amd
Space group number: 141

a (Å): 3,7830
b (Å): 3,7830
c (Å): 9,5100
Alpha (°): 90,0000
Beta (°): 90,0000
Gamma (°): 90,0000

Calculated density (g/cm^3): 3,90
Volume of cell (10^6 pm^3): 136,10
Z: 4,00

RIR: -

Status, subfiles and quality

Status: Marked as deleted by ICDD
Subfiles: Alloy, metal or intermetalic
Inorganic
Mineral
Pharmaceutical
Quality: Indexed (I)

Comments

Creation Date: 01/01/1970
Modification Date: 01/01/1970

References

Primary reference: Swanson, Tatge.,*Private Communication*, (1950)
Other: Parker.,*Z. Kristallogr.*, **59**, 1, (1923)

Peak list

No.	h	k	l	d [A]	2Theta[deg]	I [%]
1	1	0	1	3,51000	25,354	100,0
2	1	0	3	2,43500	36,884	9,0
3	0	0	4	2,37900	37,785	22,0
4	1	1	2	2,33600	38,507	9,0
5	2	0	0	1,89100	48,077	33,0
6	1	0	5	1,69900	53,922	21,0
7	2	1	1	1,66500	55,116	19,0
8	2	1	3	1,49400	62,075	4,0
9	2	0	4	1,48000	62,728	13,0
10	1	1	6	1,36700	68,596	5,0
11	2	2	0	1,33700	70,359	5,0
12	2	1	5	1,26400	75,094	10,0
13	3	0	1	1,25000	76,084	3,0
14	3	0	3	1,17100	82,267	2,0
15	3	1	2	1,16090	83,140	3,0
16				1,08690	90,261	3,0
17	3	2	1	1,04330	95,179	3,0
18	1	0	9	1,01730	98,436	2,0
19	3	1	6	0,95500	107,530	4,0
20	4	0	0	0,94610	109,014	3,0
21	3	2	5	0,91890	113,919	2,0
22	1	1	10	0,89600	118,568	3,0
23	2	2	8	0,88770	120,396	2,0
24	3	2	7	0,83110	135,896	1,0
25	4	1	5	0,82680	137,391	3,0
26	3	0	9	0,81000	143,974	1,0
27				0,79900	149,193	3,0

Stick Pattern

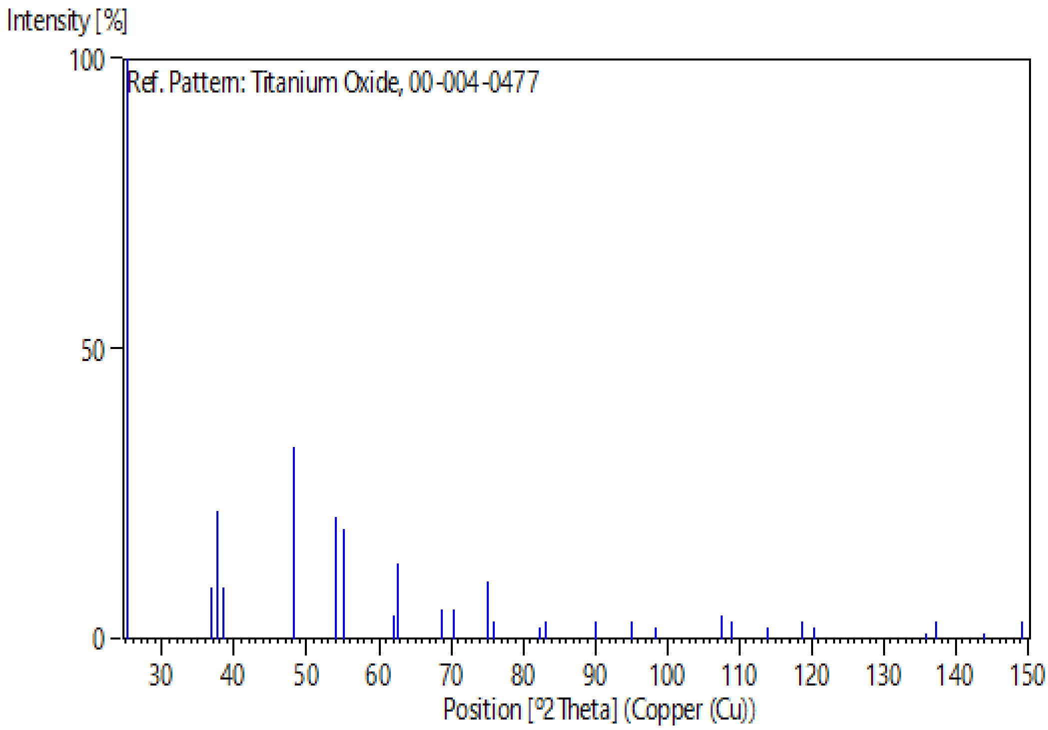

Name and formula (Rutile)

Reference code:	01-078-1509
Mineral name:	Rutile, syn
Compound name:	Titanium Oxide
Common name:	Titanium dioxide
ICSD name:	Titanium Oxide
Empirical formula:	O_2Ti
Chemical formula:	TiO_2

Crystallographic parameters

Crystal system:	Tetragonal
Space group:	P42/mnm
Space group number:	136
a (Å):	4,5933
b (Å):	4,5933
c (Å):	2,9580
Alpha (°):	90,0000
Beta (°):	90,0000
Gamma (°):	90,0000
Calculated density (g/cm^3):	4,25
Measured density (g/cm^3):	4,26
Volume of cell (10^6 pm^3):	62,41
Z:	2,00
RIR:	3,60

Subfiles and quality

Subfiles:	Alloy, metal or intermetalic
	Corrosion
	ICSD Pattern
	Inorganic
	Mineral
	Pharmaceutical
Quality:	Calculated (C)

Comments

ICSD collection code:	062678
Creation Date:	01/01/1970
Modification Date:	01/01/1970
ICSD Collection Code:	062678
Test from ICSD:	At least one TF missing
Sample Source or Locality:	Specimen from Verneuil grown (Djevahirdjian SA)
Additional Patterns:	See PDF 00-021-1276
Calculated Pattern Original Remarks:	Also anharmonic Gram-Charlier expansion calc. Charge densitiy in rutile, Ti O2.f a (P42/MNM). AX2.

References

Primary reference:	*Calculated from ICSD using POWD-12++*
Structure:	Restori, R., Schwarzenbach, D., Schneider, J.R., *ActaCrystallogr., Sec. B: Structural Science*, **43**, 251, (1987)

Peak list

No.	h	k	l	d [A]	2Theta[deg]	I [%]
1	1	1	0	3,24795	27,439	100,0
2	1	0	1	2,48693	36,087	43,6
3	2	0	0	2,29665	39,194	6,4
4	1	1	1	2,18696	41,247	16,9
5	2	1	0	2,05419	44,047	6,0
6	2	1	1	1,68724	54,329	47,8
7	2	2	0	1,62398	56,631	13,8
8	0	0	2	1,47900	62,775	6,4
9	3	1	0	1,45253	64,054	6,3
10	2	2	1	1,42355	65,519	0,5
11	3	0	1	1,35974	69,014	15,2
12	1	1	2	1,34602	69,819	7,7
13	3	1	1	1,30382	72,428	0,8
14	3	2	0	1,27395	74,408	0,2
15	2	0	2	1,24347	76,556	1,6
16	2	1	2	1,20026	79,849	0,9
17	3	2	1	1,17005	82,348	2,9
18	4	0	0	1,14832	84,259	2,0
19	4	1	0	1,11404	87,490	0,7
20	2	2	2	1,09348	89,570	4,7

Stick Pattern

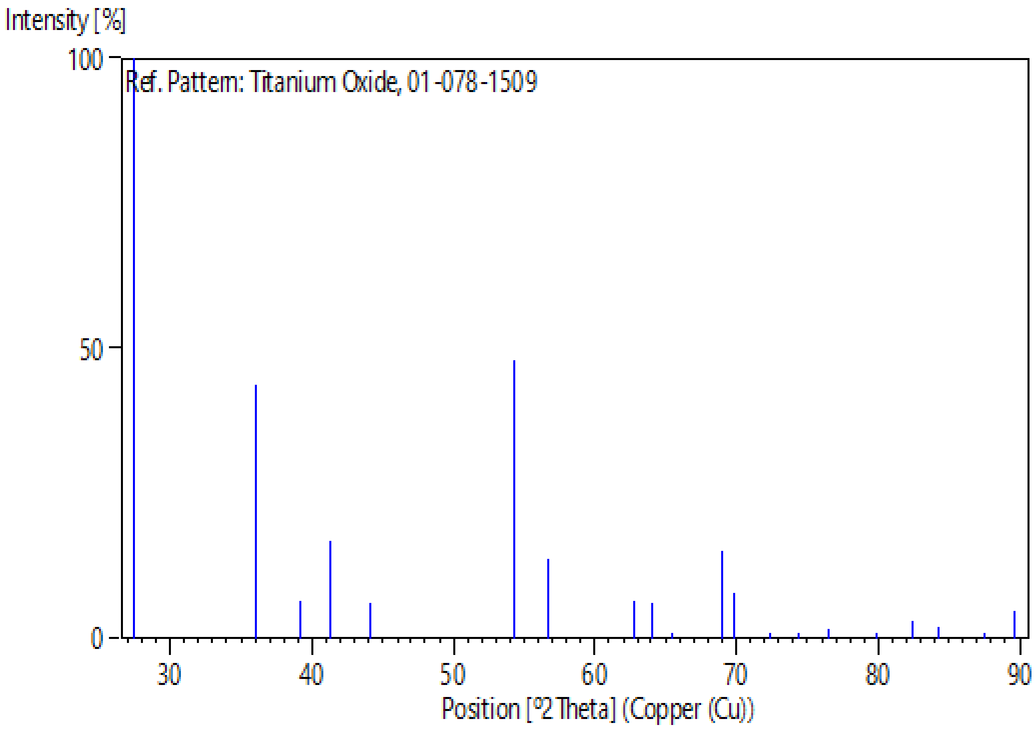

c) TiO_2-800 sample :

Name and formula (Rutile)

Reference code: 01-071-0650

Mineral name: Rutile, syn
Compound name: Titanium Oxide
ICSD name: Titanium Oxide

Empirical formula: O_2Ti
Chemical formula: TiO_2

Crystallographic parameters

Crystal system: Tetragonal
Space group: P42/mnm
Space group number: 136

a (Å): 4,5941
b (Å): 4,5941
c (Å): 2,9589
Alpha (°): 90,0000
Beta (°): 90,0000
Gamma (°): 90,0000

Calculated density (g/cm^3): 4,25
Measured density (g/cm^3): 4,26
Volume of cell (10^6 pm^3): 62,45
Z: 2,00

RIR: 3,63

Subfiles and quality

Subfiles: Alloy, metal or intermetalic
Corrosion
ICSD Pattern
Inorganic
Mineral
Pharmaceutical
Quality: Calculated (C)

Comments

ICSD collection code: 009161
Creation Date: 01/01/1970
Modification Date: 01/01/1970
ICSD Collection Code: 009161
Temperature Factor: ATF
Calculated Pattern Original Remarks: REM REF

Additional Patterns:	See PDF 00-016-0934. Rutile-Type Compounds. VI. Si O2, Ge O2 and a Comparison with other Rutile-Type Structures. f a (P42/MNM). AX2.

References

Primary reference:	*Calculated from ICSD using POWD-12++*, (1997)
Structure:	Baur, W.H., Khan, A.A., *Acta Crystallogr., Sec. B*, **27**, 2133, (1971)

Peak list

No.	h	k	l	d [A]	2Theta[deg]	I [%]
1	1	1	0	3,24852	27,434	100,0
2	1	0	1	2,48760	36,077	42,8
3	2	0	0	2,29705	39,187	6,7
4	1	1	1	2,18750	41,236	16,4
5	2	1	0	2,05454	44,039	6,0
6	2	1	1	1,68761	54,316	46,7
7	2	2	0	1,62426	56,621	13,6
8	0	0	2	1,47945	62,754	6,1
9	3	1	0	1,45278	64,041	6,3
10	2	2	1	1,42384	65,504	0,5
11	3	0	1	1,36002	68,998	15,0
12	1	1	2	1,34640	69,796	7,4
13	3	1	1	1,30408	72,411	0,8
14	3	2	0	1,27417	74,393	0,2
15	2	0	2	1,24380	76,532	1,6
16	2	1	2	1,20057	79,824	0,8
17	3	2	1	1,17028	82,328	3,0
18	4	0	0	1,14852	84,241	1,9
19	4	1	0	1,11423	87,471	0,7
20	2	2	2	1,09375	89,542	4,5

Stick Pattern

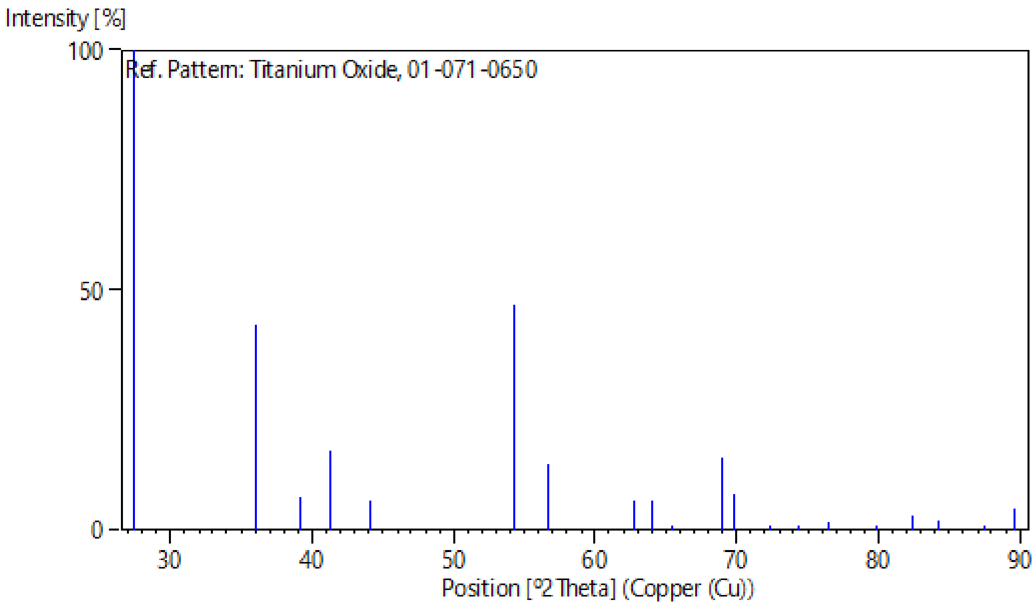

2. TiO_2-BN composites:

a) 10%TiO_2-BN sample:

Name and formula (TiO_2 Anatase)

Reference code: 01-071-1167

Mineral name: Anatase
Compound name: Titanium Oxide
ICSD name: Titanium Oxide

Empirical formula: O_2Ti
Chemical formula: TiO_2

Crystallographic parameters

Crystal system: Tetragonal
Space group: I41/amd
Space group number: 141

a (Å): 3,7892
b (Å): 3,7892
c (Å): 9,5370
Alpha (°): 90,0000
Beta (°): 90,0000
Gamma (°): 90,0000

Calculated density (g/cm^3): 3,88
Volume of cell (10^6 pm^3): 136,93
Z: 4,00

RIR: 4,95

Status, subfiles and quality

Status: Diffraction data collected at non ambient temperature
Subfiles: Alloy, metal or intermetalic
Corrosion
ICSD Pattern
Inorganic
Mineral
Pharmaceutical
Quality: Calculated (C)

Comments

ICSD collection code: 009853
Creation Date: 01/01/1970
Modification Date: 01/01/1970
ICSD Collection Code: 009853
Temperature of Data Collection: REM TEM 300 C
Calculated Pattern Original Remarks: REM M PDF 00-021-1272
Temperature Factor: ITF

Sample Source or Locality:	Specimen from Binntal, Wallis, Switzerland
Additional Patterns:	See PDF 01-071-1169. Refinement of the structure of anatase at several temperatures. e a (I41/AMDS). AX2.

References

Primary reference:	*Calculated from ICSD using POWD-12++*, (1997)
Structure:	Horn, M., Schwerdtfeger, C.F., Meagher, E.P., *Z. Kristallogr., Kristallgeom., Kristallphys., Kristallchem.*, **136**, 273, (1972)

Peak list

No.	h	k	l	d [A]	2Theta[deg]	I [%]
1	1	0	1	3,52143	25,271	100,0
2	1	0	3	2,43542	36,877	6,1
3	0	0	4	2,38425	37,698	18,4
4	1	1	2	2,33588	38,509	7,1
5	2	0	0	1,89460	47,980	23,7
6	1	0	5	1,70372	53,761	14,7
7	2	1	1	1,66845	54,992	14,4
8	2	1	3	1,49539	62,010	2,5
9	2	0	4	1,48331	62,572	10,5
10	1	1	6	1,36705	68,593	4,5
11	2	2	0	1,33968	70,198	4,8
12	1	0	7	1,28207	73,858	0,4
13	2	1	5	1,26684	74,897	7,2
14	3	0	1	1,25213	75,932	2,0
15	0	0	8	1,19212	80,505	0,3
16	3	0	3	1,17381	82,027	0,5
17	2	2	4	1,16794	82,529	3,5
18	3	1	2	1,16212	83,034	1,5

Stick Pattern

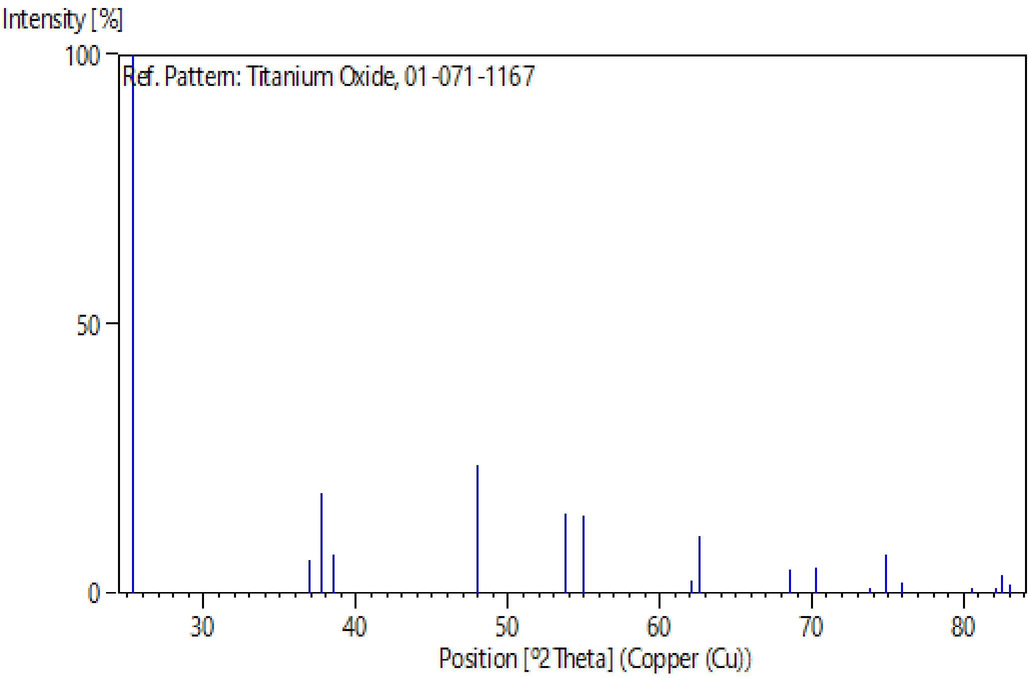

Name and formula (Quarts)

Reference code: 01-083-0539

Mineral name: Quartz
Compound name: Silicon Oxide
ICSD name: Silicon Oxide

Empirical formula: O_2Si
Chemical formula: SiO_2

Crystallographic parameters

Crystal system: Hexagonal
Space group: P3121
Space group number: 152

a (Å): 4,9210
b (Å): 4,9210
c (Å): 5,4163
Alpha (°): 90,0000
Beta (°): 90,0000
Gamma (°): 120,0000

Calculated density (g/cm^3): 2,63
Volume of cell (10^6 pm^3): 113,59
Z: 3,00

RIR: 3,07

Subfiles and quality

Subfiles: Alloy, metal or intermetalic
Corrosion
ICSD Pattern
Inorganic
Mineral
Pharmaceutical
Quality: Calculated (C)

Comments

ICSD collection code: 079634
Creation Date: 01/01/1970
Modification Date: 01/01/1970
ICSD Collection Code: 079634
Temperature Factor: ATF
Calculated Pattern Original Remarks: REM TEM Mentioned
Calculated Pattern Original Remarks: REM PRE Mentioned. Crystal structures of the low-temperature quartz-type phases of Si O2 and Ge O2 at elevated pressure
Additional Patterns: See ICSD 41447. c a (P3121). AX2.

References

Primary reference:	*Calculated from ICSD using POWD-12++*, (1997)
Structure:	Glinnemann, J., King, Jr., H.E., Schulz, H., Hahn, Th., La Placa, S.J., Dacol, F., *Z. Kristallogr.*, **198**, 177, (1992)

Peak list

No.	h	k	l	d [A]	2Theta[deg]	I [%]
1	1	0	0	4,26171	20,827	21,7
2	1	0	1	3,34924	26,593	100,0
3	1	1	0	2,46050	36,488	6,5
4	0	1	2	2,28570	39,389	6,6
5	1	1	1	2,24018	40,224	3,1
6	2	0	0	2,13086	42,384	4,9
7	0	2	1	1,98292	45,718	2,8
8	1	1	2	1,82111	50,046	11,3
9	0	0	3	1,80543	50,511	0,4
10	2	0	2	1,67462	54,772	3,4
11	1	0	3	1,66241	55,209	1,5
12	2	1	0	1,61078	57,138	0,2
13	2	1	1	1,54395	59,857	7,9
14	1	1	3	1,45561	63,902	1,5
15	3	0	0	1,42057	65,673	0,4
16	2	1	2	1,38440	67,616	4,9
17	0	2	3	1,37748	68,002	6,1
18	3	0	1	1,37409	68,193	6,6
19	0	1	4	1,29050	73,296	1,8
20	0	3	2	1,25800	75,515	2,4
21	2	2	0	1,23025	77,531	1,3
22	1	2	3	1,20194	79,715	2,4
23	2	2	1	1,19969	79,895	1,5
24	1	1	4	1,18630	80,982	2,1
25	3	1	0	1,18199	81,339	2,4
26	3	1	1	1,15481	83,677	1,5
27	0	2	4	1,14285	84,756	0,2
28	2	2	2	1,12009	86,899	0,1
29	0	3	3	1,11641	87,257	0,2

Stick Pattern

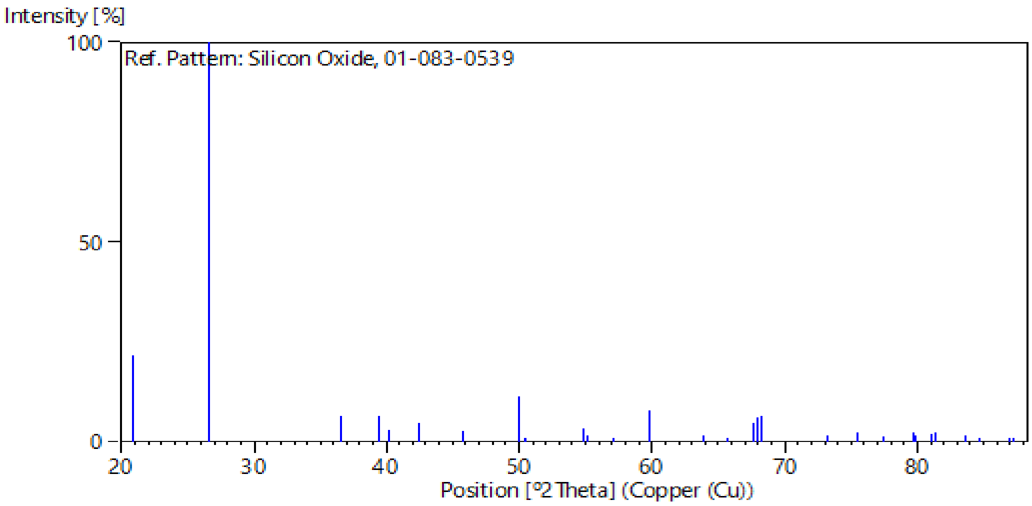

b) 30%TiO_2-BN sample

Name and formula (TiO_2 anatase)

Reference code:	01-071-1168
Mineral name:	Anatase
Compound name:	Titanium Oxide
ICSD name:	Titanium Oxide
Empirical formula:	O_2Ti
Chemical formula:	TiO_2

Crystallographic parameters

Crystal system:	Tetragonal
Space group:	I41/amd
Space group number:	141
a (Å):	3,7971
b (Å):	3,7971
c (Å):	9,5790
Alpha (°):	90,0000
Beta (°):	90,0000
Gamma (°):	90,0000
Calculated density (g/cm^3):	3,84
Volume of cell (10^6 pm^3):	138,11
Z:	4,00
RIR:	4,86

Status, subfiles and quality

Status:	Diffraction data collected at non ambient temperature
Subfiles:	Alloy, metal or intermetalic
	Corrosion
	ICSD Pattern
	Inorganic
	Mineral
	Pharmaceutical
Quality:	Calculated (C)

Comments

ICSD collection code:	009854
Creation Date:	01/01/1970
Modification Date:	01/01/1970
ICSD Collection Code:	009854
Temperature of Data Collection:	REM TEM 600 C
Calculated Pattern Original Remarks:	REM M PDF 21-1272
Temperature Factor:	ITF

Sample Source or Locality:	Specimen from Binntal, Wallis, Switzerland. Refinement of the structure of anatase at several temperatures. e a (I41/AMDS). AX2.

References

Primary reference:	*Calculated from ICSD using POWD-12++*, (1997)
Structure:	Horn, M., Schwerdtfeger, C.F., Meagher, E.P., *Z. Kristallogr., Kristallgeom., Kristallphys., Kristallchem.*, **136**, 273, (1972)

Peak list

No.	h	k	l	d [A]	2Theta[deg]	I [%]
1	1	0	1	3,52989	25,209	100,0
2	1	0	3	2,44381	36,746	6,0
3	0	0	4	2,39475	37,527	18,0
4	1	1	2	2,34205	38,404	7,0
5	2	0	0	1,89855	47,874	22,4
6	1	0	5	1,71042	53,533	13,9
7	2	1	1	1,67204	54,864	13,5
8	2	1	3	1,49927	61,832	2,3
9	2	0	4	1,48773	62,365	9,7
10	1	1	6	1,37224	68,298	4,2
11	2	2	0	1,34248	70,030	4,3
12	1	0	7	1,28738	73,503	0,4
13	2	1	5	1,27077	74,626	6,4
14	3	0	1	1,25479	75,742	1,7
15	0	0	8	1,19737	80,081	0,3
16	3	0	3	1,17663	81,789	0,5
17	2	2	4	1,17102	82,265	3,0
18	3	1	2	1,16470	82,809	1,4

Stick Pattern

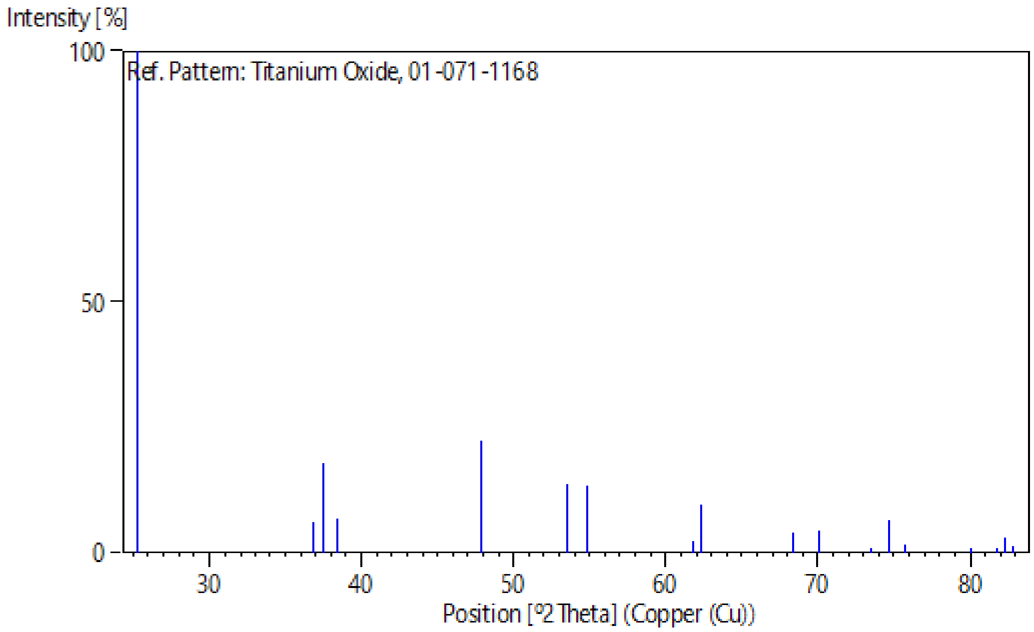

Name and formula (Quartz)

Reference code:	01-089-1961
Mineral name:	Quartz
Compound name:	Silicon Oxide
Common name:	Silicon oxide - HT
ICSD name:	Silicon Oxide
Empirical formula:	O_2Si
Chemical formula:	SiO_2

Crystallographic parameters

Crystal system:	Hexagonal
Space group:	P6222
Space group number:	180
a (Å):	4,9210
b (Å):	4,9210
c (Å):	5,4160
Alpha (°):	90,0000
Beta (°):	90,0000
Gamma (°):	120,0000
Calculated density (g/cm^3):	2,63
Volume of cell (10^6 pm^3):	113,58
Z:	3,00
RIR:	4,11

Subfiles and quality

Subfiles:	Alloy, metal or intermetalic ICSD Pattern Inorganic Mineral Pharmaceutical
Quality:	Calculated (C)

Comments

ICSD collection code:	042498
Creation Date:	01/01/1970
Modification Date:	01/01/1970
ICSD Collection Code:	042498
Test from ICSD:	No R value given
Test from ICSD:	At least one TF missing
Calculated Pattern Original Remarks:	REM TEM Mentioned. Structural relations between the low- and high-temperature forms of beta-eucryptite (Li Al Si O4) and low and high quartz. I. k g (P6222). AX2.

References

Primary reference: *Calculated from ICSD using POWD-12++*
Structure: Schulz, H., Tscherry, V., *Acta Crystallogr., Sec. B*, **28**, 2168, (1972)

Peak list

No.	h	k	l	d [A]	2Theta[deg]	I [%]
1	1	0	0	4,26171	20,827	24,8
2	1	0	1	3,34917	26,594	100,0
3	1	1	0	2,46050	36,488	5,5
4	1	0	2	2,28561	39,391	1,0
5	1	1	1	2,24016	40,224	0,3
6	2	0	0	2,13086	42,384	5,0
7	2	0	1	1,98291	45,719	3,2
8	1	1	2	1,82106	50,048	10,4
9	0	0	3	1,80533	50,514	0,4
10	2	0	2	1,67459	54,773	0,4
11	1	0	3	1,66233	55,212	0,5
12	2	1	0	1,61078	57,138	0,2
13	2	1	1	1,54394	59,857	7,1
14	1	1	3	1,45556	63,904	0,3
15	3	0	0	1,42057	65,673	0,4
16	2	1	2	1,38438	67,617	4,2
17	2	0	3	1,37743	68,005	4,8
18	3	0	1	1,37409	68,193	4,1
19	1	0	4	1,29044	73,300	1,6
20	3	0	2	1,25799	75,516	1,9
21	2	2	0	1,23025	77,531	0,9
22	2	1	3	1,20191	79,717	1,7
23	2	2	1	1,19969	79,895	0,9
24	1	1	4	1,18625	80,986	1,6
25	3	1	0	1,18199	81,339	0,7
26	3	1	1	1,15480	83,678	1,2
27	2	0	4	1,14280	84,760	0,1
28	2	2	2	1,12008	86,900	0,1
29	3	0	3	1,11639	87,259	0,1

Stick Pattern

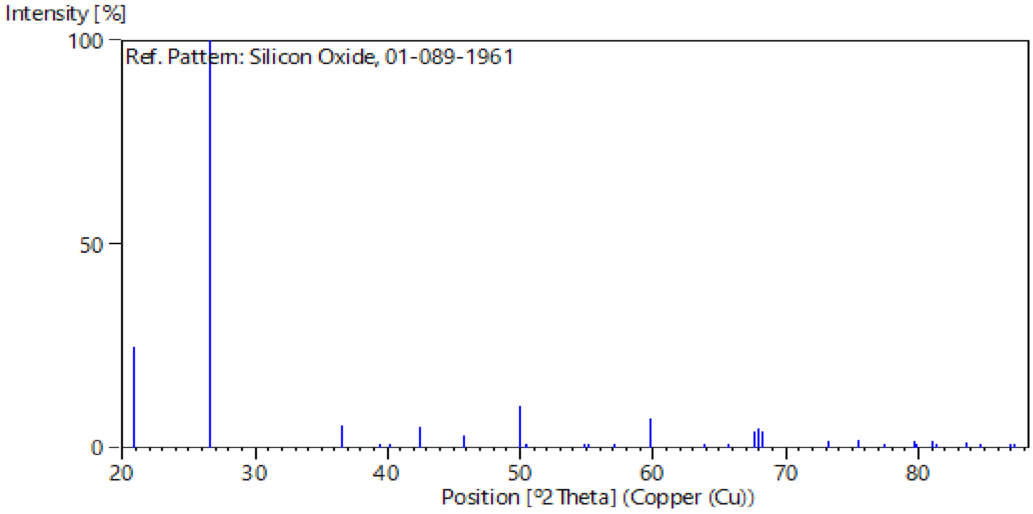

c) 50%TiO_2-BN sample:

Name and formula (TiO_2Anatase)

Reference code: 01-086-1157

Mineral name: Anatase, syn
Compound name: Titanium Oxide
ICSD name: Titanium Oxide

Empirical formula: $O_2Ti_{0.72}$
Chemical formula: $Ti_{0.72}O_2$

Crystallographic parameters

Crystal system: Tetragonal
Space group: I41/amd
Space group number: 141

a (Å): 3,7830
b (Å): 3,7830
c (Å): 9,4970
Alpha (°): 90,0000
Beta (°): 90,0000
Gamma (°): 90,0000

Calculated density (g/cm^3): 3,25
Volume of cell (10^6 pm^3): 135,91
Z: 4,00

RIR: 3,60

Subfiles and quality

Subfiles: Alloy, metal or intermetalic
Corrosion
ICSD Pattern
Inorganic
Mineral
Quality: Calculated (C)

Comments

ICSD collection code: 082084
Creation Date: 01/01/1970
Modification Date: 01/01/1970
ICSD Collection Code: 082084. Rietveld profile refinement applied
Calculated Pattern Original Remarks: REM K Minority phase (8%) in mixture with rutile from gel dr
Calculated Pattern Original Remarks: REM 343 K for 24h and annealed at 873 K for 12h in air
Test from ICSD: No R value given
Test from ICSD: At least one TF missing
Additional Patterns: See PDF 01-078-2486. Synthesis and characterization of sol-gel

Pt/(Ti O2) catalyst. e a (I41/AMDZ). N3O8.

References

Primary reference:	*Calculated from ICSD using POWD-12++*, (1997)
Structure:	Sanchez, E., Lopez, T., Gomez, R., Bokhimi, Morales, A., Novaro, O., *J. Solid State Chem.*, **122**, 309, (1996)

Peak list

No.	h	k	l	d [A]	2Theta[deg]	I [%]
1	1	0	1	3,51444	25,322	100,0
2	1	0	3	2,42777	36,998	1,4
3	0	0	4	2,37425	37,863	15,9
4	1	1	2	2,33062	38,600	1,8
5	2	0	0	1,89150	48,064	26,0
6	1	0	5	1,69745	53,975	16,0
7	2	1	1	1,66559	55,094	13,4
8	2	1	3	1,49210	62,162	0,8
9	2	0	4	1,47941	62,756	8,7
10	1	1	6	1,36222	68,870	4,6
11	2	2	0	1,33749	70,330	5,0
12	1	0	7	1,27707	74,196	0,2
13	2	1	5	1,26333	75,141	7,5
14	3	0	1	1,25003	76,082	1,7
15	0	0	8	1,18712	80,915	0,1
16	3	0	3	1,17148	82,226	0,2
17	2	2	4	1,16531	82,756	2,8
18	3	1	2	1,16004	83,216	0,6

Stick Pattern

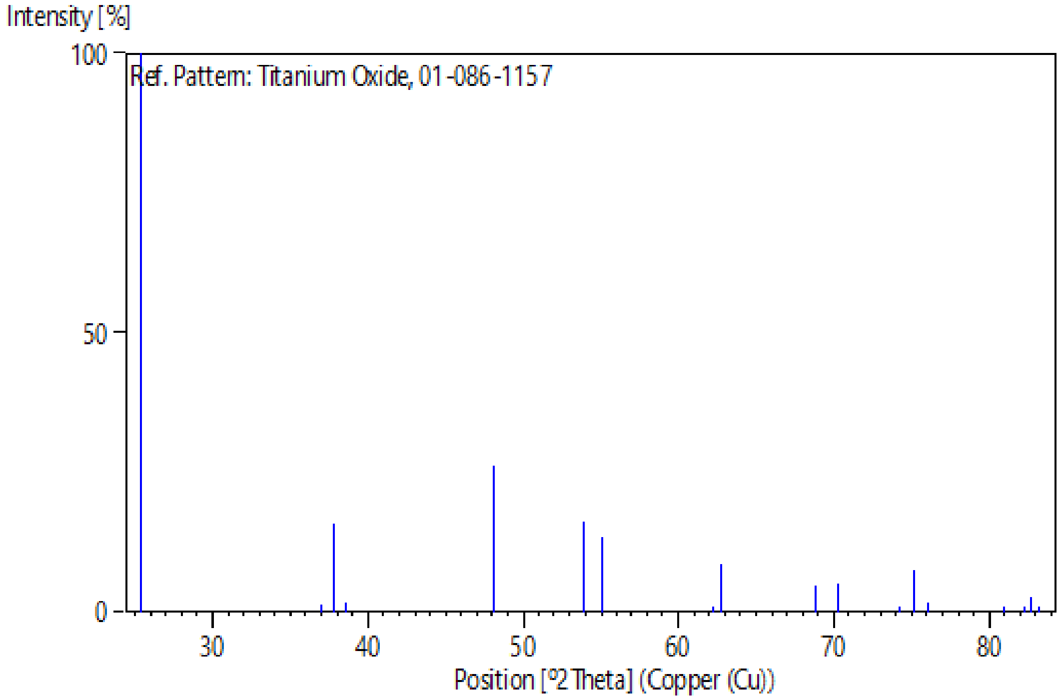

Name and formula (Quartz)

Reference code:	01-070-3755
Mineral name:	Quartz
Compound name:	Silicon Oxide
ICSD name:	Silicon Oxide
Empirical formula:	O_2Si
Chemical formula:	SiO_2

Crystallographic parameters

Crystal system:	Hexagonal
Space group:	P3121
Space group number:	152
a (Å):	4,9160
b (Å):	4,9160
c (Å):	5,4090
Alpha (°):	90,0000
Beta (°):	90,0000
Gamma (°):	120,0000
Calculated density (g/cm^3):	2,64
Volume of cell (10^6 pm^3):	113,21
Z:	3,00
RIR:	2,93

Subfiles and quality

Subfiles:	Alloy, metal or intermetalic ICSD Pattern Inorganic Mineral
Quality:	Calculated (C)

Comments

ICSD collection code:	090145
Creation Date:	01/01/1970
Modification Date:	01/01/1970
ICSD Collection Code:	090145
Test from ICSD:	REF Journal of Applied Crystallography
Test from ICSD:	CLAS 32 (Hermann-Mauguin) - D3 (Schoenflies)
Test from ICSD:	PRS hP9
Test from ICSD:	ANX AX2
Test from ICSD:	WYCK c a
Temperature Factor:	ITF. Rietveld profile refinement applied
Sample Source or Locality:	Specimen from Baveno, Novara, Italy
Additional Patterns:	See PDF 01-079-1910. Accuracy of XRPD QPA using the combined Rietveld-RIR method.

References

Primary reference:	*Calculated from ICSD using POWD-12++*
Structure:	Gualtieri, A.F., *J. Appl. Crystallogr.*, **33**, 267, (2000)

Peak list

No.	h	k	l	d [A]	2Theta[deg]	I [%]
1	1	0	0	4,25738	20,848	21,9
2	0	1	1	3,34542	26,624	100,0
3	1	1	0	2,45800	36,527	6,5
4	1	0	2	2,28283	39,441	6,3
5	1	1	1	2,23778	40,269	2,9
6	2	0	0	2,12869	42,430	4,4
7	2	0	1	1,98082	45,770	2,7
8	1	1	2	1,81899	50,109	9,9
9	0	0	3	1,80300	50,584	0,3
10	0	2	2	1,67271	54,840	3,0
11	0	1	3	1,66025	55,287	1,3
12	2	1	0	1,60914	57,201	0,2
13	1	2	1	1,54234	59,925	6,4
14	1	1	3	1,45382	63,990	1,2
15	3	0	0	1,41913	65,749	0,3
16	1	2	2	1,38287	67,701	3,7
17	2	0	3	1,37581	68,096	4,5
18	0	3	1	1,37267	68,273	4,9
19	1	0	4	1,28880	73,409	1,3
20	3	0	2	1,25663	75,612	1,6
21	2	2	0	1,22900	77,624	0,8
22	2	1	3	1,20054	79,827	1,8
23	2	2	1	1,19845	79,994	1,1
24	1	1	4	1,18479	81,107	1,4
25	3	1	0	1,18079	81,440	1,7
26	1	3	1	1,15362	83,783	0,9
27	2	0	4	1,14142	84,887	0,2
28	2	2	2	1,11889	87,015	0,1
29	3	0	3	1,11514	87,381	0,2

Stick Pattern

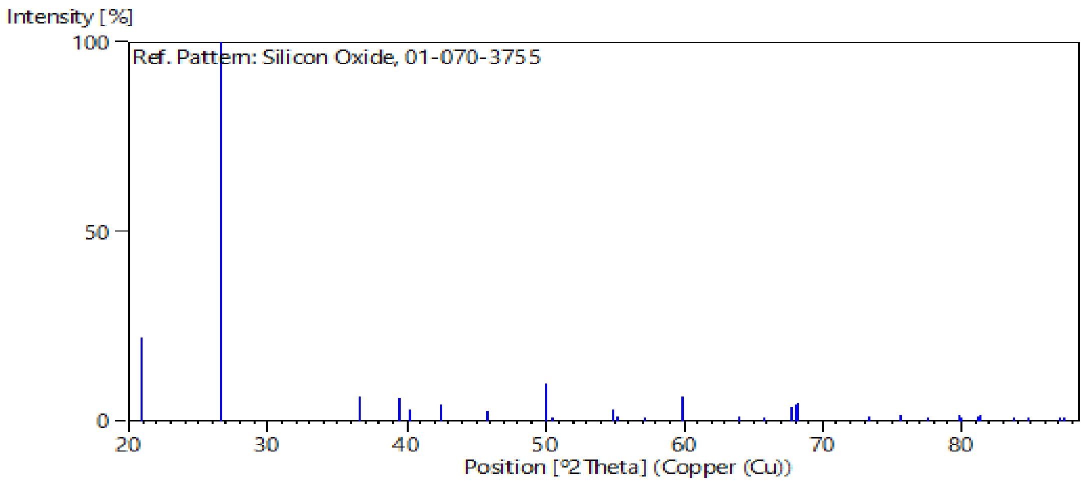

Publications:

Kahoul, K., Ahmedchekkat, F., & Chiha, M. (2025). ***Intensification of Rhodamine B Photodegradation Using TiO_2 Nanocatalyst Synthesized via Non-conventional Sol-Gel Method***. *Desalination and Water Treatment*, 101433. http://doi.org/10.1016/j.dwt.2025.101433.

Conference participations :

International communication :

Effect of thermal treatment on photocatalytic activity of synthesized titanium dioxide nanoparticles via the sol-gel method.1ère Conférence Internationale sur les Procédés Industriels et la Conservation Environnementale (CISPICE'2021), Skikda du 07 au 09 décembre 2021. (**Poster**).

Effect of crystalline phase of synthesized TiO_2 photocatalyst on the organic dye removal. The *First International Conference on Petrochemistry and Energy Transition (ICPET23), November 21st to 23rd, 2023, Skikda, Algeria.* (**Poster**).

Synthesis of titanium dioxide nanoparticles by modified sol-gel method. First international conference on materials science and applications, ICMSA'23 (Hybrid) held from February 08th to 09th 2023, at Khenchla University (Algeria). (**Poster**).

National communications:

Photocatalytic degradation of Rhodamine B using synthesized nano-TiO_2. First national conference on advanced materials and their applications (NCAMA'23), October 18 and 19th 2023, Tipaza. Algeria. (**Poster**)

A comparative study on synthesized and commercial TiO_2 photocatalysts for organic dye removal. The 1st National Conference on Physics and Its Applications (NCPA'2023), 2nd December 2023, Bousaada, Algeria (**Oral**).